MONASH University

A Census of Low Redshift AGNs

Madhooshi Ruwanpura Senarath

Doctor of Philosophy

Supervised by:
A.Prof. Michael J.I. Brown
A.Prof. Michelle E. Cluver

A Thesis Submitted for the Degree of Doctor of Philosophy at
Monash University in 2021
School of Physics and Astronomy

Copyright notice

A Census of Low Redshift AGNs

Abstract

In this thesis we conducted a census of low redshift Active Galactic Nuclei (AGNs) using a combination of infrared (IR) colour, optical colour and emission line ratios to select obscured, unobscured and variable AGNs. Previous AGN surveys use optical/ultraviolet (UV), X-ray and radio wavelengths to measure the space density of AGNs. However, these wavelengths are subject to well-known selection effects where the optical/UV are obscured by dust, the soft X-ray is sensitive to electron attenuation and only some AGNs are powerful in the radio. We determine whether there are populations of AGNs that have been missed by previous AGN surveys that use less comprehensive criteria to select AGNs. This thesis also aims to make improvements on the cosmic accretion history by using our AGN samples to search for changing look AGNs (CLAGNs), determine bolometric corrections, measure luminosity functions and constrain the accretion rate density.

We systematically search for CLAGNs at $z < 0.04$ that may have changed spectral type in the past decade using photometry from PanSTARRS, SkyMapper and *WISE* to search the entire sky. A variety of selection methods was used to select CLAGN candidates, including measuring changes in flux over time, which may indicate a change in spectral type. Optical colour as a proxy for changes in Hα equivalent width was also used. We identify two new CLAGNs using our optical colour selection method, NGC 1346 and 2MASX J20075129-1108346. These AGNs were confirmed as CLAGNs using observations with WiFeS on the 2.3m telescope at Siding Spring in 2018 and 2019.

To determine AGN bolometric luminosities using photometry (and thus constrain the accretion rate), we have measured AGN bolometric corrections for optical/UV, X-ray and IR wavelengths. To do this we use the best available AGN SEDs at this time which include a variety of obscured and unobscured AGNs. Bolometric luminosities were calculated by integrating over a wider wavelength range than much of recent literature, including the IR to X-ray wavelength range; 24 µm - 8 keV. Our bolometric luminosities cover a wider luminosity range than much of the literature with $\log(L_{bol}) \approx 42.5$ - 47.5 erg s^{-1}. We find that our bolometric luminosities are almost directly proportional to IR luminosity irrespective of IR wavelength, which is at odds with some of the literature. This result is in part due to our sample selection, and in part due to the methods used to fit the relationship between the IR and bolometric luminosities.

We then determined the IR $z < 0.35$ AGN luminosity function using the GAMA survey. AGNs were selected using IR colour, emission line widths, emission line flux ratios and the Véron-Cetty & Véron (2010) catalogue. We see that the AGNs selected using colour were the most luminous; including broad line AGNs, and the AGNs selected using emission line ratios were narrow line with lower luminosities. The break in our IR luminosity function was found to occur at lower luminosities than optical luminosity functions from the literature. We used our IR luminosity function and IR bolometric corrections to measure the accretion rate densities at low redshifts ($z < 0.35$). Extrapolating using our magnitude range, for a magnitude range of -35 $<$ M_{W1} (mag) $<$ -20, we calculate an accretion rate density of 2.85 $\pm$ 0.36 $\times$ 10^{-6} $M_{\odot}$ yr^{-1} Mpc^{-3} which agrees within 20 % of accretion rate densities measured in the literature with the bolometric luminosity function by Barger et al. (2001).

Publications during enrolment

- **A Systematic Survey for z $<$ 0.04 Changing-Look AGNs**. Assoc. Prof. Michael J.I. Brown and Assoc. Prof. Michelle E. Cluver, Prof. Thomas H. Jarrett, Prof. Christian Wolf, Dr. Nicholas P. Ross, Prof. John R. Lucey, Dr. Vaishali Parkash and Dr Wei J. Hon. Published March 2021, *Monthly Notices of the Royal Astronomical Society.* DOI:10.1093/mnras/stab393.

Thesis including published works declaration

I hereby declare that this thesis contains no material which has been accepted for the award of any other degree or diploma at any university or equivalent institution and that, to the best of my knowledge and belief, this thesis contains no material previously published or written by another person, except where due reference is made in the text of the thesis.

This thesis includes one original paper published in a peer reviewed journal entitled: 'A Systematic Survey for z $<$ 0.04 Changing-Look AGNs' (Senarath et al., 2021). The core theme of the thesis is determining whether there are populations of AGNs that have been missed by previous AGN surveys. The ideas, development and writing up of all the papers in the thesis were the principal responsibility of myself, the student, working within the School of Physics and Astronomy under the supervision of Assoc. Prof. Michael Brown and Assoc. Prof. Michelle Cluver.

The inclusion of co-authors reflects the fact that the work came from active collaboration between researchers and acknowledges input into team-based research.

In the case of Chapter 2 my contribution to the work involved the following:

Thesis Chapter	Publication Title	Status	Nature and % of student contribution	Co-author name(s) Nature and % of Co-author's contribution	Co-author(s), Monash Student Y/N
Chapter 2	'A Systematic Survey for z $<$ 0.04 Changing-Look AGNs'	Published	85 %. Writing of publication, sample selection, analysis.	Michael J.I. Brown, 6% Michelle E. Cluver, 3 % Thomas H. Jarrett, 2% Christian Wolf, 2% Nicholas P. Ross, 0.5 % John R. Lucey, 0.5 % Vaishali Parkash, 0.5 % Wei J. Hon, 0.5 %	No No No No No No No No

I have renumbered sections of submitted or published papers in order to generate a consistent presentation within the thesis.

Student name: Madhooshi Ruwanpura Senarath

Student signature:

Date: 26/11/2021

I hereby certify that the above declaration correctly reflects the nature and extent of the student's and co-authors' contributions to this work. In instances where I am not the responsible author I have consulted with the responsible author to agree on the respective contributions of the authors.

Main Supervisor name: Assoc. Prof. Michael J.I. Brown

Main Supervisor signature:
Date:. 26/11/2021

Acknowledgements

First and foremost, I would like to thank my supervisors Michael Brown and Michelle Cluver for their guidance, support and patience throughout my PhD. In particular, for always providing feedback, for sharing their knowledge and always making time to meet with me to discuss my work. I am extremely grateful for their enthusiasm and excitement about my work and for always pushing me to make my work better.

I wish to thank Jean Pettigrew, for always having her door open when I needed help and for always being a source of positivity. I would also like to thank my postgraduate coordinators Kristian Helmerson and Duncan Galloway for their support through this PhD. I want to thank the collaborators and co-authors I have worked with throughout my candidature for sharing their knowledge and providing feedback on Chapter 2 of this thesis: Christian Wolf, Thomas H. Jarrett, Rachel Webster, Wei J. Hon, John R. Lucey and Nicholas P. Ross.

I am indebted to my unofficial academic big sister, Vaishali Parkash, for her guidance and support throughout my entire PhD, and for always listening to me when I needed someone to talk to. I would not be where I am today without her. I would also like to thank my fellow PhD students for their friendship and guidance.

I am also grateful to my wonderful friends Supipi Amarasekera, Madhini Kuruppu and Amani Kekunawala for always being excited to hear about my research and for providing me with comfort and encouragement.

Finally, and most importantly, I wish to thank my mother, father and brother for encouraging me to do my best, for listening to my troubles and for always believing in me, even when I didn't. In particular my father for his love of amateur astronomy which lead me down the path to pursuing a PhD in astronomy.

Contents

Copyright notice i

Abstract ii

Publications during enrolment iv

Thesis including published works declaration v

Acknowledgements vii

List of Figures x

List of Tables xii

1 Introduction 1
- 1.1 Galaxy formation and evolution . . . 3
- 1.2 Galaxy Bimodality . . . 7
  - 1.2.1 Galaxy morphology . . . 7
  - 1.2.2 Galaxy kinematics . . . 8
  - 1.2.3 Galaxy colour . . . 10
- 1.3 Active Galactic Nuclei . . . 13
- 1.4 AGN SEDs and classes of AGNs . . . 15
  - 1.4.1 Type 1 and 2 AGNs . . . 15
  - 1.4.2 AGN type selection as a function of wavelength . . . 15
  - 1.4.3 Changing look AGNs (CLAGNs) . . . 20
  - 1.4.4 Probing Galaxy Properties using Spectroscopy. . . . 21
- 1.5 The Luminosity Function of AGNs . . . 23
- 1.6 Supermassive Black Hole Accretion History . . . 25
- 1.7 Thesis aims . . . 28

2 A Systematic Survey for z < 0.04 Changing-Look AGNs 30
- 2.1 Abstract . . . 31
- 2.2 Introduction . . . 31
  - 2.2.1 Why CLAGN change spectral type . . . 34
  - 2.2.2 Known CLAGNs . . . 35
- 2.3 Candidate selection . . . 38
  - 2.3.1 Imaging surveys and catalogues . . . 39
  - 2.3.2 Optical colour selection . . . 40

2.3.3 Optical flux variability selection . . . 42
2.3.4 Infrared flux variability selection . . . 43
2.3.5 AGNs with 2 or more archival spectra . . . 45
2.4 Spectroscopic follow-up . . . 48
2.5 Spectral variability and new CLAGNs . . . 49
2.5.1 2MASX J20075129-1108346 . . . 50
2.5.2 Mrk 609 . . . 50
2.5.3 Mrk 915 . . . 51
2.5.4 NGC 1346 . . . 51
2.6 Conclusions . . . 52

3 AGN Bolometric Corrections 57
3.1 Introduction . . . 57
3.2 The SED Sample . . . 60
3.3 Calculating Bolometric Luminosity. . . . 62
3.4 Bolometric corrections . . . 66
3.4.1 Calculating Bolometric correction . . . 66
3.4.2 Effects of different fitting techniques . . . 67
3.4.3 Effects of Host galaxy light . . . 68
3.4.4 PAHs . . . 74
3.4.5 UV/optical Bolometric corrections . . . 77
3.4.6 X-ray bolometric corrections . . . 77
3.5 IR Bolometric corrections . . . 80
3.6 Bolometric corrections for all Brown et al 2019 SEDs . . . 84
3.7 Summary and Conclusions . . . 88

4 Infrared AGN Luminosity Function 92
4.1 Introduction . . . 92
4.2 AGN sample selection . . . 95
4.2.1 The GAMA catalogue . . . 95
4.2.2 BPT selected AGNs . . . 96
4.2.3 Colour selection . . . 97
4.2.4 Known AGNs . . . 101
4.2.5 Comparison with optical colour selection and emission line widths . . . 104
4.2.6 BPT and Colour of Brown et al. (2019) SEDs . . . 105
4.2.7 Type 2 quasars . . . 107
4.3 Absolute magnitudes . . . 109
4.4 GAMA IR AGN luminosity functions . . . 112
4.5 Accretion rate density . . . 120
4.6 Conclusions . . . 124

5 Summary and Conclusions 127

Bibliography 137

List of Figures

1.1 Large scale structures of the Universe (Springel et al., 2006). . . 5
1.2 Galaxy merger tree for an elliptical galaxy from De Lucia & Blaizot (2007). . . . 6
1.3 The Hubble tuning fork diagram used to classify galaxies (Hubble, 1936). . . . 8
1.4 Stellar velocity fields of galaxies from the SAURON sample of E (elliptical) and S0 galaxies. . . . 9
1.5 Optical colour-magnitude diagram from Schawinski et al. (2014) which shows the binomial distribution of galaxy colours. . . . 11
1.6 *WISE* IR colour-colour diagram used to classify galaxies from Wright et al. (2010) . . . 12
1.7 Schematic of the unified model of AGNs from Beckmann & Shrader (2012). . . . 14
1.8 Spectra of a type 1 and a type 2 Seyfert. . . . 16
1.9 Intermediate type 1 Seyferts. . . . 17
1.10 Schematic representation of an AGN SED from Padovani et al. (2017), loosely based on observed SEDs. . . . 18
1.11 Schematic of an image-slicing IFU setup. . . . 22
1.12 SDSS data release 3 optical quasar luminosity function from Richards et al. (2006a). . . . 26
1.13 Observed halo mass function from Bell et al. (2003) compared to the halo mass function of the Millenium Simulation (Springel et al., 2005). . . . 28
1.14 Accretion rate density of black holes as a function of redshift from Barger et al. (2001). . . . 29

2.1 Spectra of NGC 2617, a previously identified CLAGN. . . . 35
2.2 Skymapper *riz* colours for our CLAGN candidates. . . . 41
2.3 Pan-STARRS catalogue *riz* colours for our CLAGN candidates . 42
2.4 The *r*-band magnitude as a function of apparent magnitude for Véron-Cetty & Véron (2010) type 1.8s, type 1.9s and type 2s. . . 44
2.5 Change in NEOWISE W1 photometry as a function of W1 photometry. . . . 45
2.6 Spectra of 2MASX J20075129-1108346, a new CLAGN. . . . 53
2.7 Spectra of Mrk 609, an AGN with varying spectra which does not meet our criteria for CLAGN. . . . 54
2.8 Spectra of Mrk915, an AGN with varying spectra which does not meet our criteria for CLAGN. . . . 55

2.9 Spectra od NGC 1346, a new CLAGN. 56

3.1 SED of Mrk 279 from Brown et al. (2019). 61
3.2 Schematic of the Hyper-fit linear model (Robotham & Obreschkow, 2015). 68
3.3 4C 19.44 SED (Shang et al., 2011). 71
3.4 WISE colour-colour diagram of the 27 Brown et al. (2019) AGN SEDs in our sample. 75
3.5 UV/Optical bolometric corrections for the Brown et al. (2019) SEDs. 78
3.6 X-ray bolometric correction with κ_{bol} vs L_{bol} 79
3.7 Hard X-ray bolometric corrections. 80
3.8 1.5 µm, 2 µm and 3 µm bolometric corrections. 82
3.9 7 µm, 12 µm, 15 µm and 24 µm bolometric corrections. 85
3.10 SED of AGN PG1307+085, a Brown et al. (2019) SED without X-ray data. 89

4.1 Magnitude-redshift figure of our GAMA galaxies with AGNs selected using BPT and *WISE* colour-colour indicated. 95
4.2 Distribution of our AGN sample in the three GAMA equatorial fields: G09, G12 and G15. 97
4.3 BPT diagram of GAMA galaxy catalogue. 98
4.4 AGNs selected by BPT criterion. 99
4.5 BPT selected AGNs that appears in the 'AGN' box region of the *WISE* colour-colour diagram. 100
4.6 *WISE* apparent magnitude colour-colour diagram of GAMA galaxy catalogue prior to k-corrections. 101
4.7 AGNs selected by colour criterion. 102
4.8 Galaxies that appear in the star forming region of the *WISE* colour-colour diagram. 103
4.9 Optical colour-colour plot of GAMA sample. 106
4.10 Colour-colour and BPT plots of the Brown et al. (2019) SEDs. . 107
4.11 Two most IR bright Type 2 AGNs in our sample. 108
4.12 k-correction at z = 0.35. 110
4.13 Histogram of GAMA galaxies. 113
4.14 W1 magnitude as a function of W1 uncertainty. 114
4.15 W1 absolute magnitude vs W1 - W2 colour. 115
4.16 Luminosity function of all galaxies in GAMA and AGNs in GAMA using a magnitude limit of W1 = 18 mag. 116
4.17 Absolute W1 magnitude vs redshift displaying our binning. . . . 118
4.18 Our Bolometric AGN luminosity function. 122

List of Tables

1.1 Some luminosity functions from the literature 24

2.1 Known $z < 0.04$ CLAGNs and their respective types and references. 37
2.2 Sample taken from our SkyMapper catalogue used to select CLAGN candidates. 46
2.3 Sample taken from our Pan-STARRS (PS1) catalogue used to select CLAGN candidates. 47
2.4 CLAGN candidates that were observed with WiFeS between 2018 July and 2019 March. 48

3.1 Wavelength range archival bolometric corrections integrate over to measure bolometric luminosities. 59
3.2 Our bolometric luminosities ($\log(L_{bol})$) and IR monochromatic luminosities ($\log(\lambda L_\lambda)$). Note all are in units of erg s^{-1}. 65
3.3 H-band host galaxy fractions of AGNs in our sample. 69
3.4 Our bolometric luminosities ($\log(L_{bol})$) and IR monochromatic luminosities ($\log(\lambda L_\lambda)$) after subtracting NGC 584 host galaxy template. Note all are in units of erg s^{-1}. 72
3.5 Our optical and UV bolometric corrections with non zero intercept in the form $\log(L_{bol}) = A + B\log(\lambda L_\lambda)$ measured using Hyper-fit. 76
3.6 Our X-ray bolometric corrections with non zero intercept in the form $\log(L_{bol}) = A + B\log(\lambda L_\lambda)$ measured using Hyper-fit. 80
3.7 Our IR bolometric corrections with non zero intercept in the form $\log(L_{bol}) = A + B\log(\lambda L_\lambda)$ measured using Hyper-fit. 86
3.8 Our optical/UV and IR bolometric corrections, when Compton thick AGNs are removed form the sample, with non zero intercept in the form $\log(L_{bol}) = A + B\log(\lambda L_\lambda)$ measured using Hyper-fit. 87

4.1 Numbers of $z < 0.35$ AGNs selected with each method. 102
4.2 Our $z < 0.35$ quasar luminosity function with Poisson uncertainties, where the three GAMA regions cover 180 square degrees with a magnitude limit of W1 = 18 mag. 120

Chapter 1

Introduction

One of the most important questions in astronomy today is understanding how galaxies evolve and grow over cosmic time (see The National Committee for Astronomy, 2016; Committee for a Decadal Survey of Astronomy and Astrophysics, 2020). Central to this is the transformation of gas into stars and the subsequent end of star formation in many galaxies, where active galactic nuclei (AGN) may play a role by heating or ejecting gas from galaxies (Tabor & Binney, 1993; Silk & Rees, 1998; Fabian, 1999b, 2012). Understanding the characteristics of the effects of AGNs is complicated by holes in AGN demographics arising from systematic biases in each of the wavelengths with which AGNs are observed.

The distributions of nearby galaxy properties are often bimodal, including (but not limited to) colour, morphology, star formation rate and kinematics (Tully et al., 1982; Strateva et al., 2001; Baldry et al., 2004; Hogg et al., 2004; Schneider et al., 2007; Brammer et al., 2009). Broadly speaking, most optically red galaxies contain little cool gas and dust and are comprised of old evolved red stars. Optically blue galaxies contain cold gas and are undergoing active star formation. Galaxy mass grows from star formation and mergers, where star formation dominates for disk galaxies, while mergers dominate for massive elliptical galaxies (e.g. De Lucia & Blaizot, 2007; Hopkins et al., 2007, and references therein). Star formation in galaxies does not remain constant and mergers of galaxies can either trigger short bursts of star formation or quench the star formation in galaxies (Kereš et al., 2005; Croton et al., 2006; Menci, 2006; Birnboim et al.,

2007; Dressler et al., 2009; Cen, 2011). The specific cause of why star formation in galaxies is quenched is unknown, however a possible major contributor may be AGNs.

Most massive galaxies have a supermassive black hole (SMBH) at their centre (Magorrian et al., 1998; Ho, 1999). Accretion of material towards the central black hole converts the potential energy of matter in the accretion disk to radiation and particle flow (e.g. Barger et al., 2001; Zheng et al., 2007; Beckmann & Shrader, 2012; Yang et al., 2012; Wang et al., 2013). The process of AGN feedback takes place when the energy and radiation generated by accretion interacts with the gas in the host galaxy. Silk & Rees (1998), Fabian (1999a) and Fabian (2012), amongst others, find that it is possible that the intense flux of photons and particles produced by the AGN quenches the galaxy bulge of interstellar gas, leading to termination of star formation, and consequently terminating the AGN as there is no fuel for accretion. Studies of quasar and AGN demographics provide a principle constraint on the number of accreting SMBHs, elucidating the importance of the role that they play in the evolution of galaxy populations (e.g. Barger et al., 2001; Zheng et al., 2007; Yang et al., 2012; Wang et al., 2013).

A major goal of AGN surveys is to measure the cosmic accretion rate history (i.e. black hole accretion histories) as this allows inferences to be made about the evolution of galaxies. To do this, we require both an AGN bolometric correction and an AGN luminosity function which give the relationship between the bolometric luminosity function and the accretion rate;

$$\epsilon \dot{M}_{BH} = L_{bol}/c^2 \tag{1.1}$$

where $\dot{M}_{BH}$ is the mass inflow rate, ϵ is radiative efficiency of the accretion energy and L_{bol} is the bolometric luminosity (e.g. Barger et al., 2001; Fabian, 2012).

The space density of AGNs has previously been measured using optical/UV, X-ray and radio wavelengths. However these wavelengths suffer from significant and well known selection effects where especially optical and ultra-violet (UV)

light can be obscured by dust, leading to an underestimate of the true space density. The X-ray emission is believed to largely be the result of inverse Compton scattering of the photons in the accretion disk by the hot corona (Padovani et al., 2017). A limitation of X-ray is that soft X-ray wavelengths are also sensitive to electron attenuation. Although in theory the hard X-ray band is able to select all types of AGNs, it has a tendency to miss AGNs with low luminosity.

Radio wavelengths are sensitive to synchrotron emission, however, strong radio emission only happens in a small subset of AGNs (Miley, 1980; Condon, 1992; Padovani et al., 2017). The mid-infrared (MIR), which probes the hot dusty torus (Barvainis, 1987; Antonucci, 1993; Padovani et al., 2017), is not impacted by dust obscuration and is less prone to variability at shorter wavelengths and may therefore provide the best means (i.e. is well correlated with the bolometric luminosity and accretion rate) of measuring the space density of AGNs.

Motivated by the selection effects experienced by previous AGN surveys, this thesis focuses on determining whether there are populations of (potentially significant) AGNs that have been overlooked, by using a combination of IR/optical photometry and emission line ratios to select both obscured, unobscured and variable AGNs. We first systematically search for 'changing look' AGNs (CLAGNS) in the local ($z < 0.04$) Universe. Next we measure IR AGN bolometric corrections and subsequently, we use photometry from the Galaxy And Mass Assembly survey (GAMA, Wright et al., 2016) to measure the space density of AGNs in the IR to determine whether there are populations of AGNs that have been missed by previous surveys. For the remainder of this chapter, we provide a brief review of the current understanding of galaxy formation and evolution with a particular focus on AGNs.

1.1 Galaxy formation and evolution

The accepted theory on the formation and evolution of galaxies is built upon the ΛCDM paradigm, which describes a Universe comprised of non-relativistic cold dark matter, radiation, baryonic matter and dark energy (e.g. Blumenthal et al., 1984; Amanullah et al., 2010; Komatsu et al., 2011). In this framework, small

density perturbations, produced during the inflationary period of the Universe, are responsible for the large scale structures we see in the Universe today, formed through the gravitational attraction of dark matter haloes.

The distribution of dark matter structures from N-body simulations by Springel et al. (2006) look like the large scale structures that we see in current the Universe, and this can be seen in Figure 1.1. These structures began as small initial density perturbations and have grown over cosmic time and are observed in the cosmic microwave background radiation (CMB; Bennett et al., 2003). The density perturbations collapsed to form the first gravitationally bound proto-galactic structures which interact with each other and merge to form early type galaxies. The fine filaments that link these nodes contain galaxies as well, and these filaments are surrounded by voids, which are under-dense regions (Pimbblet et al., 2004). The growth and subsequent quenching of a galaxy is thought to be affected by the cosmic environment it was formed in. That is, galaxies that are formed in a void have a higher star formation rate than galaxies of equal mass in the higher density nodes and filaments (Grogin & Geller, 2000; Von Benda-Beckmann & Müller, 2008). The interactions of these galaxies and subsequent star formation (and the formation of more metal rich stars) resulted in the formation of later type galaxies.

The first galaxies that formed were irregular in shape (e.g. Bromm & Yoshida, 2011, and references therein). As the mass of the first galaxies increased, it caused them to spin up and the angular momentum acting on them shaped them into disk-dominated spiral galaxies, which comprised of a disk of stars contained within a disk of HI gas and dust (Springel et al., 2005). This model of galaxy formation and large-scale structure follows the theory of a 'bottom-up' model of hierarchical galaxy formation (White & Rees, 1978).

Following this process, galaxies continued to grow through mergers. It should be noted that this aspect of the 'bottom-up' model occurs irrespective of the star formation rates of the galaxies. The merging of galaxies forms elliptical galaxies (e.g. Toomre & Toomre, 1972; De Lucia & Blaizot, 2007, and references therein). These mergers destroy disks and are responsible for the diversity of the orbital planes of stars in elliptical galaxies. The most massive elliptical galaxies

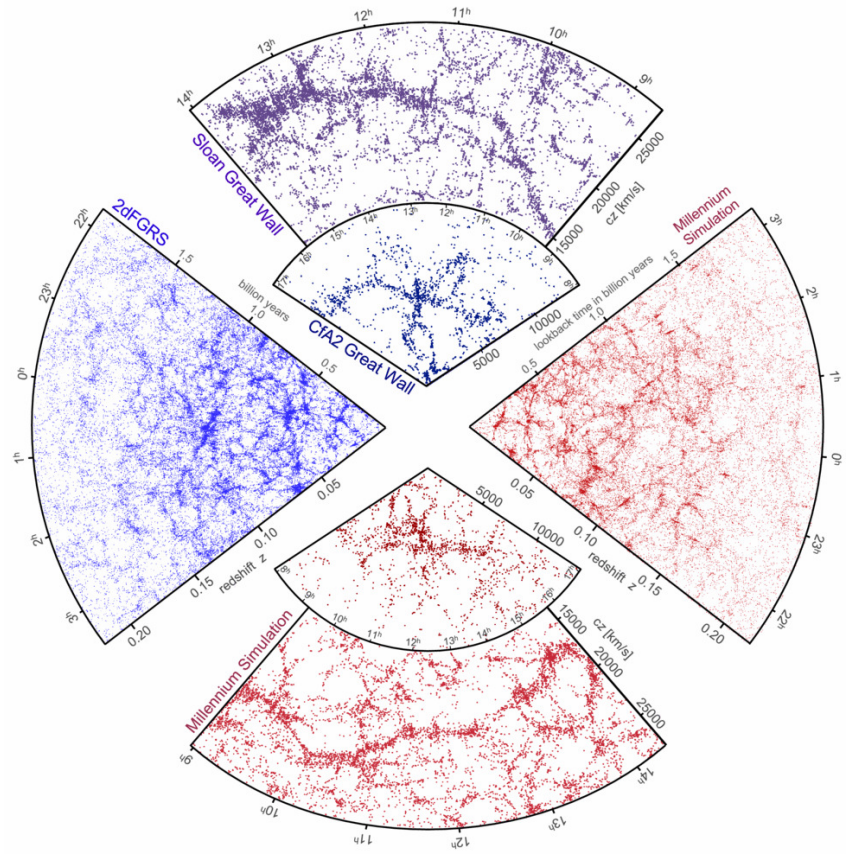

FIGURE 1.1: Depiction of large scale structures of the Universe, constructed using semi-analytic techniques which are used to simulate the formation and evolution of the galaxies (Springel et al., 2006). The simulated results are comparable to the observed structure from 2dFGRS (left wedge with purple points, Colless et al., 2001) and Sloan Digital Sky Survey (top wedge with blue points York et al., 2000).

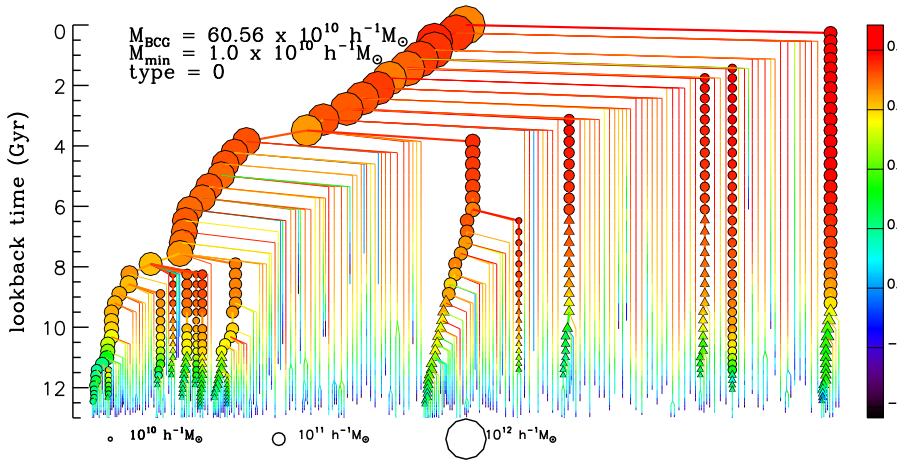

FIGURE 1.2: Galaxy merger tree for an elliptical galaxy from De Lucia & Blaizot (2007), determined using models. The colours and size of the circles indicate the optical colour and mass of the galaxies, respectively. This figure shows the hierarchical merging of smaller galaxies to form massive elliptical galaxies, and that the galaxies become more optically red with decreasing look-back time, indicating a decrease in star formation.

we observe in the Universe are thought to have formed through recent mergers (approximately in the last 3 Gyrs according to Figure 1.2 from De Lucia & Blaizot (2007)) even though their stellar populations are $\sim$ 10 Gyr old (White & Frenk, 1991; Cole et al., 2000). Figure 1.2 demonstrates the hierarchical merging of smaller galaxies to form larger galaxies; in the case of this figure it shows the merger tree of an elliptical galaxy (De Lucia & Blaizot, 2007). Galaxy growth may also be caused by AGNs that trigger star formation due to AGN feedback (Ishibashi et al., 2013). This feedback is driven by radiation pressure on dusty gas.

It should be noted that the above description of the formation of spiral and elliptical galaxies is an idealised view, the reality of this formation and evolutionary process is far more complicated. The star formation in galaxies does not remain constant and mergers of galaxies can either trigger short bursts of star formation or quench the star formation in the galaxy. Star formation in elliptical galaxies has also decreased over time and this is illustrated clearly by Figure 1.2 from De Lucia & Blaizot (2007), where the optical colour of elliptical galaxies becomes more red in recent times when compared to elliptical galaxies at lookback times of $>$ 10 Gyrs. This reddening is due to the decline in star formation, as well as

the ageing of existing stellar populations. The quenching of star formation leads to passive galaxies (Hopkins, 2008). The reason why these galaxies cease their star formation is unknown, however a possible cause may be connected to AGN activity.

1.2 Galaxy Bimodality

1.2.1 Galaxy morphology

Galaxy morphologies are correlated to their gas content, star formation and kinematics and can be highly varied across different galaxy types. Galaxy morphology and classifications have been a century old discussion beginning with the discovery by Hubble (1926) that spiral nebula have distances beyond our galaxy. Since then, attempts have been made to group galaxies based on their morphology or shape.

The most widely recognised galaxy classification scheme is that of Hubble (1926), which classified the shapes of galaxies first into two major groups of shapes; spirals (which have a flattened disk, a centrally concentrated bulge and spiral arms) and ellipticals (which are spheroidal in appearance and largely lacking in substructure), and then subdivided into galaxies within these two groups. Spiral galaxies are typically blue in colour and have an abundance of gas and dust and have active star formation. Elliptical galaxies are typically optically red in colour and have little or no star formation. Elliptical galaxies are separated by the severity of their projected axis ratios and spiral galaxies are separated based on whether they contain bars and the tightness of the spiral arms. This is illustrated in Figure 1.3, which depicts the 'Hubble tuning fork diagram' (Hubble, 1936) with the elliptical galaxies forming the handle of the tuning fork and the S0 galaxy type at the point where the two handles branch out to barred and unbarred spiral galaxies. As elliptical galaxies are formed from mergers, it makes sense that elliptical galaxies are typically more common in galaxy clusters and dense environments (Hubble & Humason, 1931).

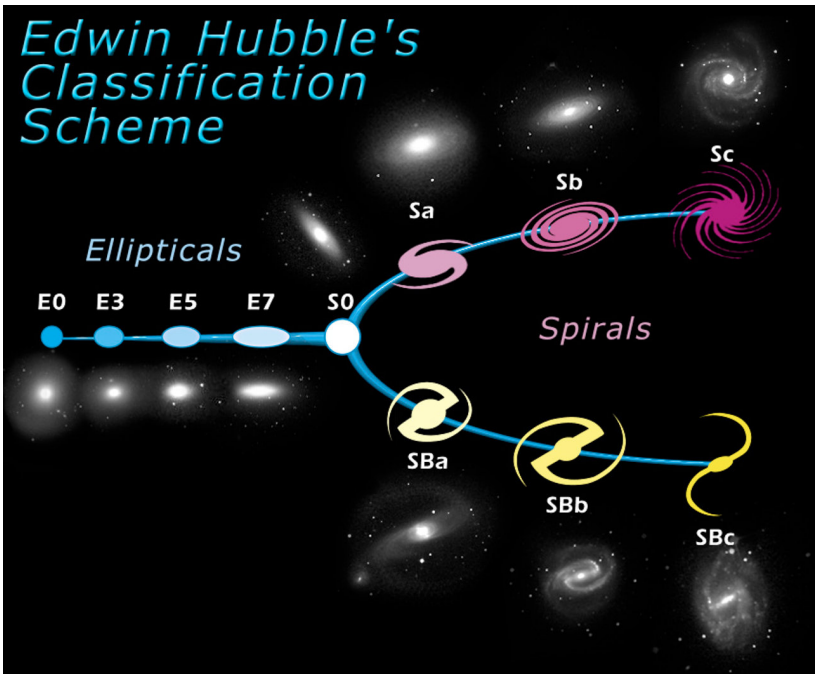

FIGURE 1.3: The Hubble tuning fork diagram used to classify galaxies (Hubble, 1936). The elliptical galaxies are classified by their degree of ellipticity and spiral galaxies are separated on whether they contain bars and the tightness of the spiral arms.

Hubble (1926) also included a third group of galaxies called lenticular galaxies which fall between the spiral and elliptical galaxies, classified as S0 on the tuning fork diagram. Lenticular galaxies contain a bright central bulge which is surrounded by a disk, however they do not have any spiral structures. Objects that do not fall into any of these three categories are referred to as irregular galaxies. Hubble's classification is a starting point, and while the classification is too simple and has been revised to include features such as bars and rings (de Vaucouleurs, 1959), the classification scheme has remained mostly unchanged.

1.2.2 Galaxy kinematics

The current methods by which galaxies are classified goes beyond the Hubble tuning fork model. With the advent of integral field spectroscopy, it has become possible to map stellar population absorption lines spatially across a galaxy. This provides the velocity and angular momentum of the galaxy, i.e. its kinematics (Cappellari et al., 2007; Emsellem et al., 2007; Fogarty et al., 2014; Brough et al., 2017; Raouf et al., 2021). Early-type galaxies are classified as fast or

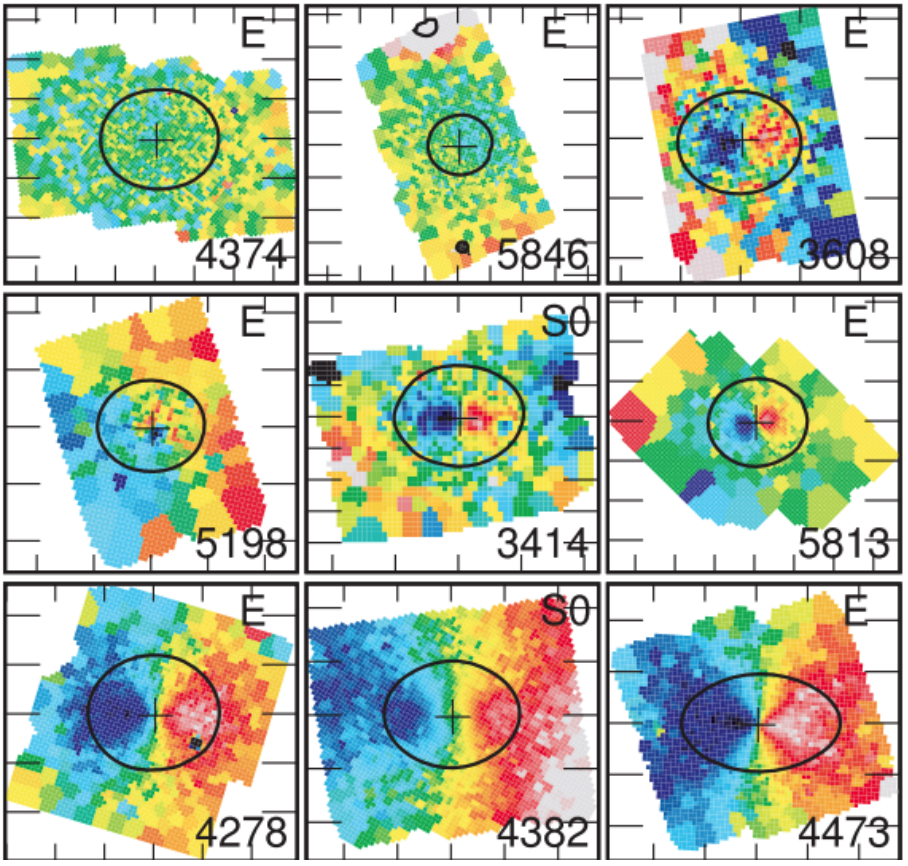

FIGURE 1.4: Stellar velocity fields of galaxies from the SAURON sample of E and S0 galaxies, the stellar rotation increases from the top left to the bottom right (Emsellem et al., 2007). Fast rotating galaxies are disk dominated and slow rotating galaxies are dispersion-dominated.

slow rotators according to their specific stellar angular momentum. Fast rotating galaxies rotate rapidly and contain stellar disks, while slow rotating galaxies are dispersion-dominated (Cappellari & Copin, 2003; Emsellem et al., 2007; Krajnović et al., 2011). Emsellem et al. (2007) shows this clearly using the SAURON survey sample shown in Figure 1.4.

Most disk-dominated galaxies are classified as fast rotators using this scheme (Weijmans et al., 2014). However, approximately half of all elliptical galaxies and 90% of S0 galaxies are also found to be fast rotators (Fogarty et al., 2014; Jeong et al., 2019; van de Sande et al., 2021). This was a surprising result as we expect elliptical galaxies to be dispersion dominated (de Zeeuw & Franx, 1991).

1.2.3 Galaxy colour

Galaxies can be classified by their optical colour as either red or blue and this colour is dependent on the stellar population of the galaxy (Tinsley, 1968; Hogg et al., 2002). Hot, short-lived OB type stars emit light that peaks at the blue end of the optical spectrum. Long-lived cooler stars such as K and M type stars peak at redder wavelengths. Consequently younger galaxies with active star formation appear bluer in colour and these are typically spiral galaxies, while older galaxies will appear redder. Thus colour is often used as a proxy for galaxy shape.

Galaxies generally exist in either the 'blue cloud' or in the 'red sequence' as is illustrated in Figure 1.5 from Schawinski et al. (2014), an optical colour magnitude diagram. The 'green valley' population exists between these two populations and represents a transition population. Galaxies in this region are hypothesised to be transitioning from blue to red (Bell et al., 2004; Wyder et al., 2007; Schawinski et al., 2014). It should be noted that recent work has shown that using colour alone to classify galaxy morphologies does not always work (e.g. Taylor et al., 2014). This is due to dust obscuration, where dust is heated in star forming regions by UV and visible light which is then re-emitted in the infrared. This makes galaxies appear redder than the colour we observe from their stellar population (Calzetti, 2001).

Large-scale surveys such as the Sloan Digital Sky Survey (SDSS, Abazajian et al., 2004), the Wide-field Infrared Survey Explorer (*WISE*, Wright et al., 2010), SkyMapper (Wolf et al., 2018) and the Panoramic Survey Telescope and Rapid Response System (Pan-STARRS, Chambers et al., 2019; Flewelling et al., 2020) have been used to show that galaxy colour distribution is in general bimodal (e.g. Strateva et al., 2001; Hogg et al., 2002; Baldry et al., 2004; Cluver et al., 2020). A widely used method for determining galaxy types is the *WISE* colour-colour diagram shown in Figure 1.6 from Wright et al. (2010); this is similar to the *WISE* colour-colour diagram from Jarrett et al. (2011).

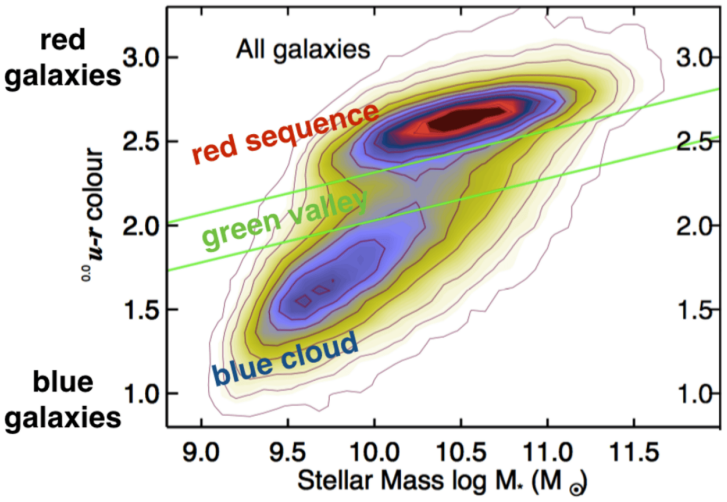

FIGURE 1.5: Optical colour-magnitude diagram from Schawinski et al. (2014). This shows the bimodal distribution of galaxy colours, highlighting the blue colour section and the red colour section. The 'green valley' is also shown and this represents a transition population between the two larger groups.

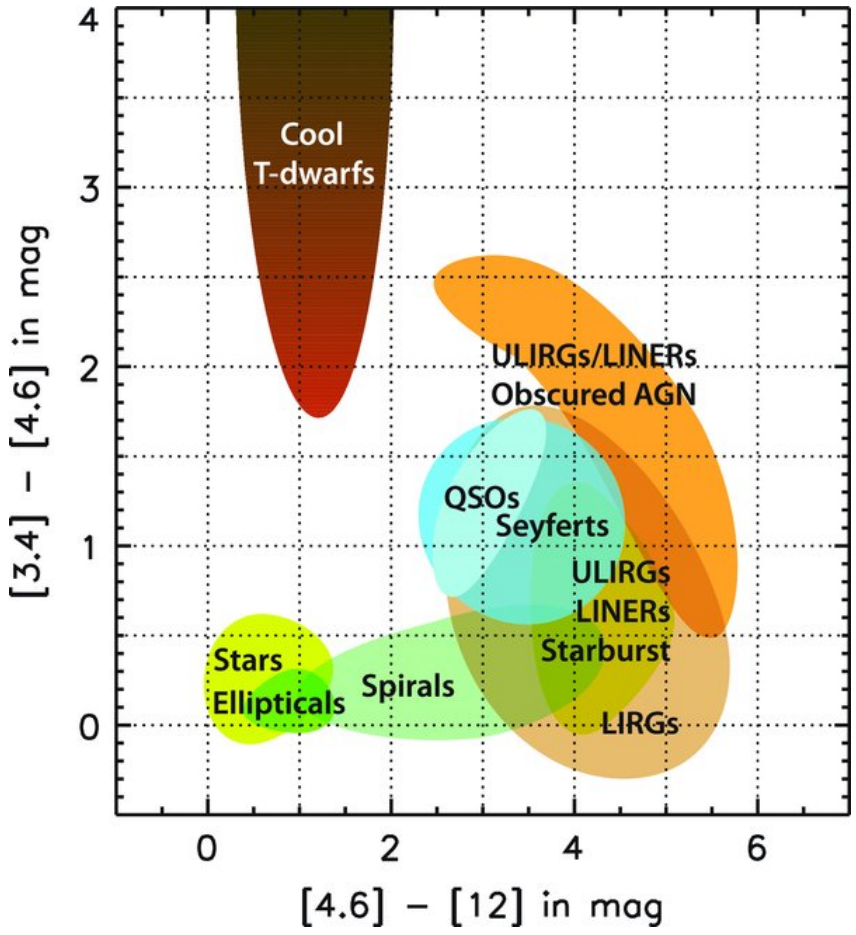

FIGURE 1.6: *WISE* IR colour-colour diagram (in Vega magnitudes) which can be used to classify galaxies as AGNs, star forming galaxies and passive galaxies (Wright et al., 2010).

1.3 Active Galactic Nuclei

AGNs are compact, energetic inner regions of galaxies that are powered by the accretion towards a SMBH with mass 10^4 - 10^{10} $M_\odot$ (Osterbrock, 1989). AGNs are very luminous and may thus play a complex role in galaxy evolution, heating gas that would otherwise cool and collapse to form new stars (Silk & Rees, 1998; Fabian, 1999a).

AGNs with emission line spectra are split into two classes, $M_B >$ -21.5 + 5log h_{100} Seyfert galaxies and $M_B <$ -21.5 + 5log h_{100} quasars (Schmidt & Green, 1983). In Seyfert galaxies, the total energy emitted from their compact nuclear source is comparable to the total energy emitted by all stars in the galaxy (Peterson, 1997). On the other hand, the total energy emitted from their compact nuclear sources in a quasar is greater than the total energy emitted by all the stars in the galaxy by a factor of up to > 100 (Peterson, 1997).

The unified model of AGN proposes that all observed AGN types/classes are a single type of object, observed under different conditions (Antonucci, 1993). The main parameters are the orientation of the AGN along the line of sight and the radio loudness. The orientation determines the optical detectability of the AGN, and the broad-line region and the radio loudness dictates whether the AGN produces a jet (Beckmann & Shrader, 2012). This is presented in the schematic in Figure 1.7. In the context of the unified model (Antonucci, 1993), the difference between the two classes results from the orientation of the dusty torus that can obscure the broad-line emitting region. The obscuring dusty torus is heated by the AGN, and the dust within it emits blackbody radiation that can be detected in the mid-infrared.

The general size of the disk is 10^{11} - 10^{12} m, which is approximately 100 times smaller than the broad line region (BLR) (which is $\approx$ 0.1 pc). The torus is approximately 0.1 to a few pc in size (Jaffe et al., 2004; Burtscher et al., 2013; Mason, 2015). The narrow line region (NLR) can extend out to $\gtrapprox$ 1 kpc (e.g. Storchi Bergmann, 2015, and references therein).

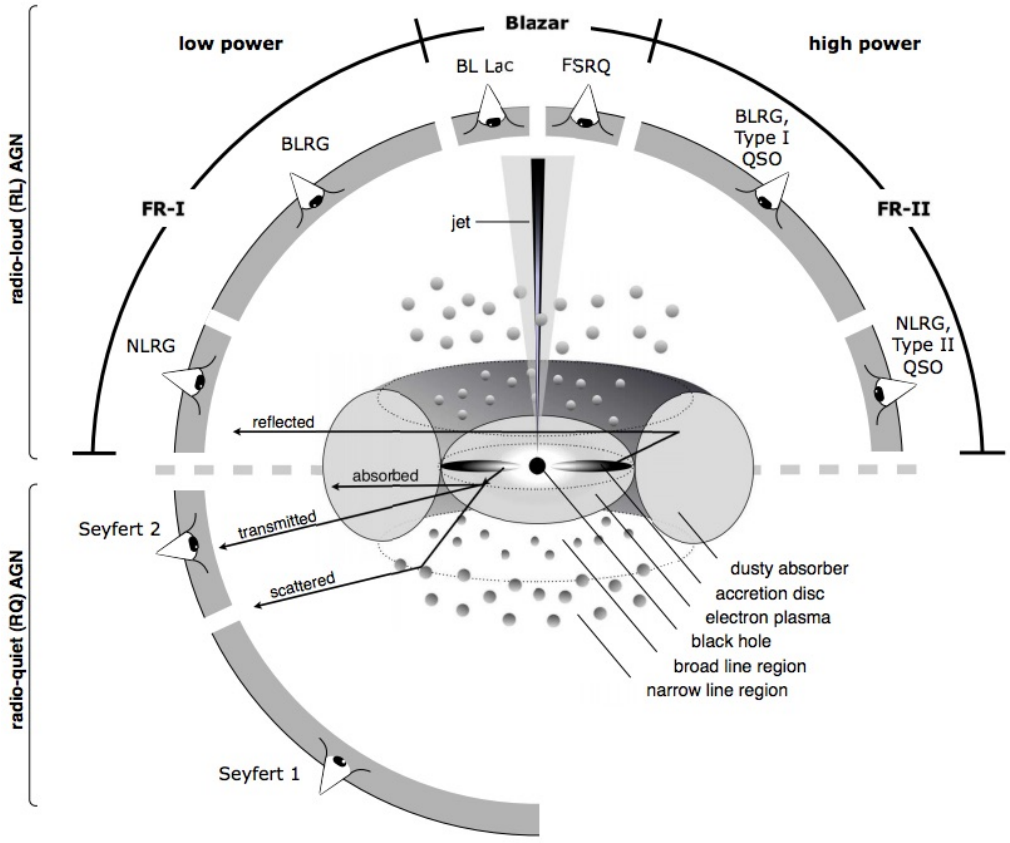

FIGURE 1.7: Schematic of the unified model of AGNs from Beckmann & Shrader (2012). According to this schematic the type of object observed depends on the angle at which we are viewing the AGN.

1.4 AGN SEDs and classes of AGNs

1.4.1 Type 1 and 2 AGNs

The classic spectroscopic sub-classes for AGNs are broad and narrow emission line AGNs, type 1 (unobscured) and type 2 (obscured), although there are intermediate classes containing combinations of broad and narrow-line components (Osterbrock, 1989). Type 1 AGNs contain permitted broad emission lines (1000 - 10,000 km sec^{-1}) as well as narrow-line emission lines ($<$ 1000 km sec^{-1}) superposed (e.g. Osterbrock, 1989; Netzer, 2015). Narrow lines are characteristic of low-density ionized gas (electron density $n_e \approx 10^3$ - 10^6 cm^{-3}), where the width of the line corresponds to velocities of approximately 100 km/s. Broad lines are permitted lines only, and are a result of emission from broad-line high density gas ($n_e \approx 10^9$ cm^{-3} or higher). Type 2 AGNs differ from type 1 AGNs as they contain only narrow-line emission ($<$ 1000 km sec^{-1}), thus the threshold for type 1 and type 2 is 1000 km sec^{-1} (Peterson, 1997). Figure 1.8 presents two galaxies, one type 1 and the other type 2, where the difference between broad-line and narrow-line is clearly visible.

There are also intermediate type 1 Seyferts (1.2, 1.5, 1.8 and 1.9) which are classified according to the appearance of their optical spectra. Some examples of intermediate type AGNs are shown in Figure 1.9 (Osterbrock, 1981). Seyfert 1.2 galaxies have a strong broad Hβ component (an example of this is Mrk 079, panel a of Figure 1.9). Seyfert 1.5 galaxies have narrow lines with obvious Hα and Hβ components (an example of this is NGC 1667, panel b of Figure 1.9). Seyfert 1.8 galaxies, identified by Osterbrock (1978), have narrow lines with a broad Hα component and a recognisable Hβ component (an example of this is Mrk 609, panel c of Figure 1.9). Seyfert 1.9 galaxies have a broad Hα line, but other lines are narrow (an example of this is UGC 7064, panel d of Figure 1.9).

1.4.2 AGN type selection as a function of wavelength

Different wavelengths trace different regions and properties of an AGN, this consequently impacts the classes and luminosities of AGNs selected by different

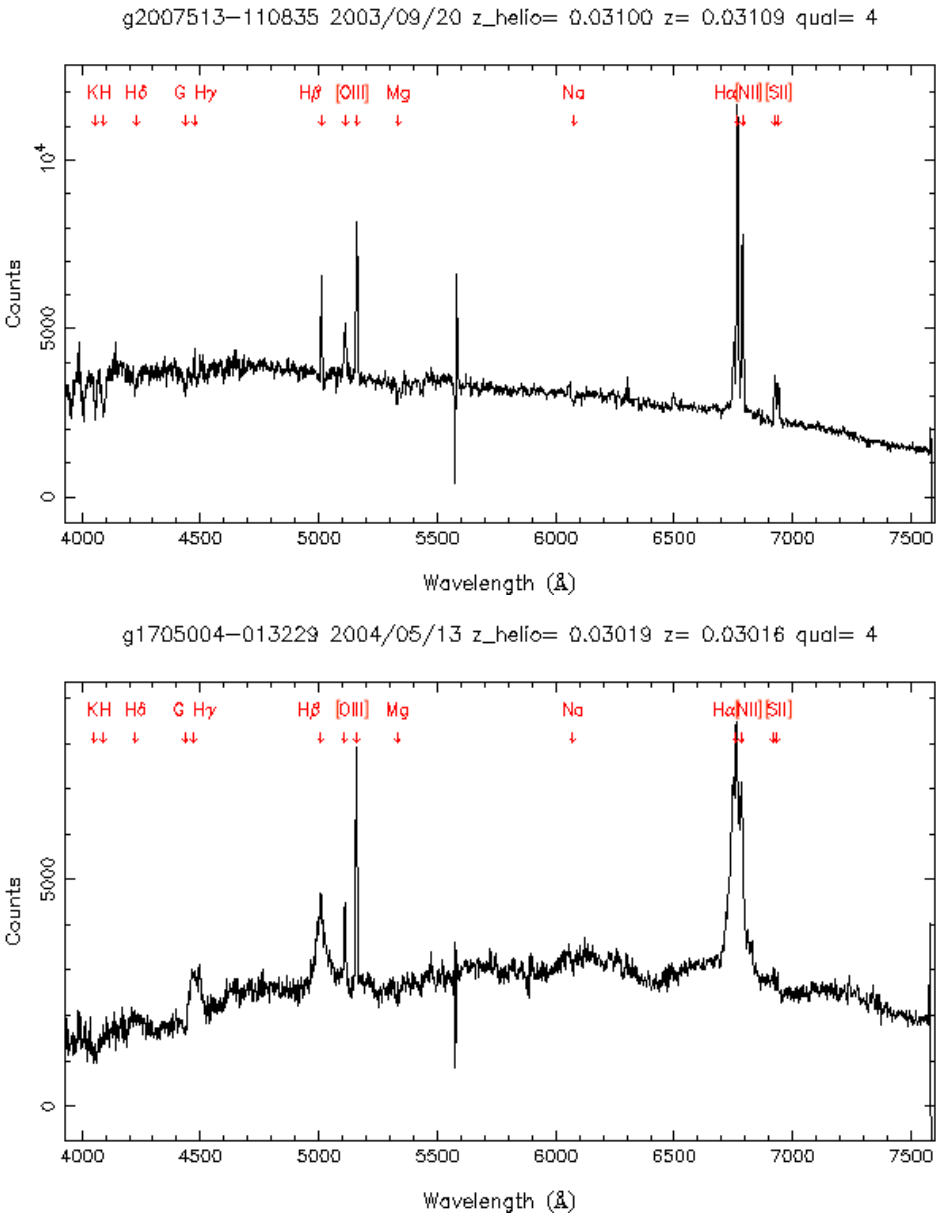

FIGURE 1.8: Panel (a): Spectra of 2MASX J20075129-1108346, a type 2 Seyfert galaxy obtained by Jones et al. (2009). This spectrum clearly contains only narrow lines with booming Hα emission (it is also one of our "changing look" AGN candidates). Panel (b): Spectra of 2MASX J1705004-013229, a type 1 Seyfert galaxy obtained by Jones et al. (2009). This spectrum clearly contains both broad-line (Hα) and narrow-line ([OIII]) peaks (this is another of our "changing look" AGN candidates).

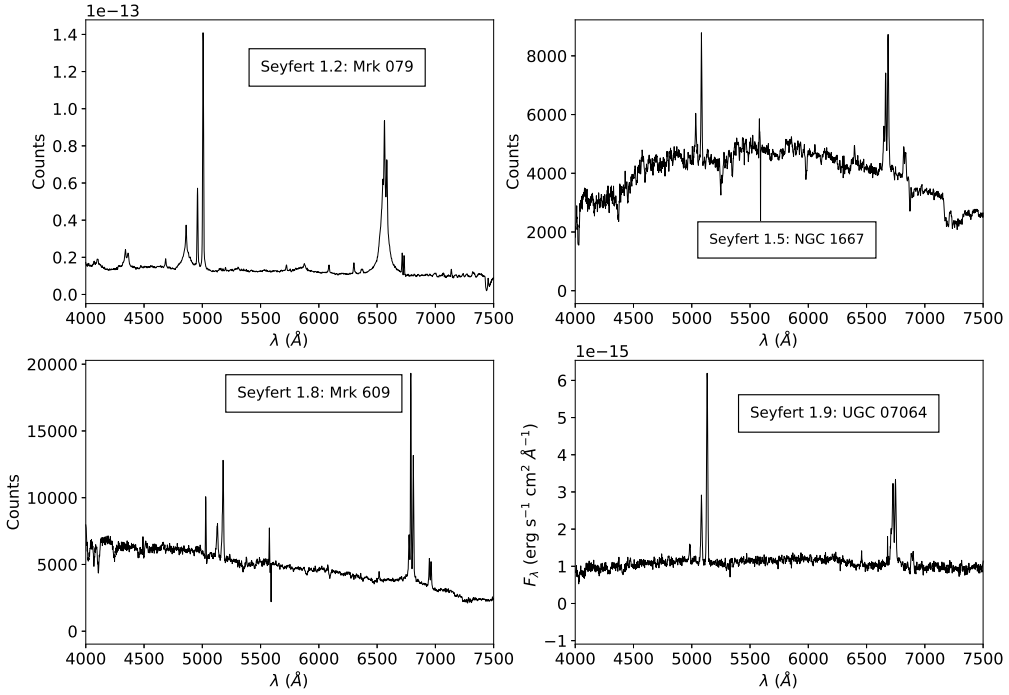

FIGURE 1.9: Intermediate type 1 Seyferts classified according to (Osterbrock, 1981). Mrk 79 is an example of a Seyfert 1.2 galaxy (Gavazzi et al., 2013), NGC 1667 is an example of a Seyfert 1.5 galaxy (Jones et al., 2009), Mrk 609 is an example of a Seyfert 1.8 galaxy (Jones et al., 2009) and UGC 7064 is an example of a Seyfert 1.9 galaxy (Jones et al., 2009). These galaxies all contain broad and narrow lines, but are categorised as intermediate type 1s as the appearance of their optical spectra differ.

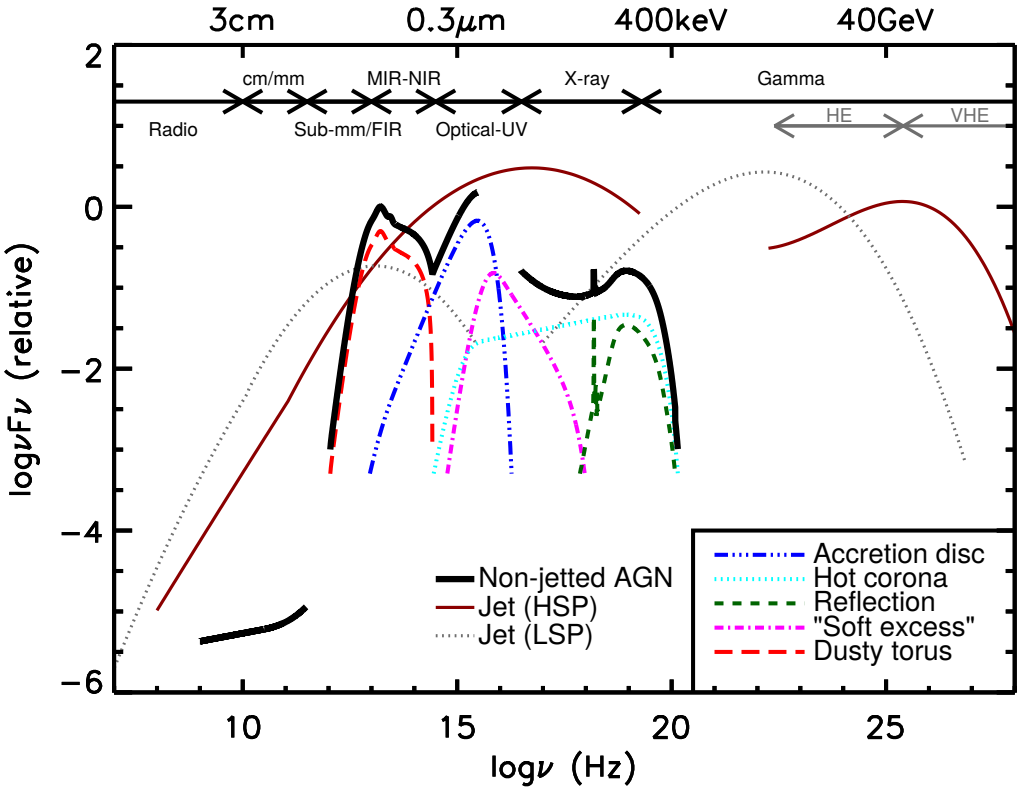

FIGURE 1.10: Schematic representation of an AGN SED from Padovani et al. (2017), loosely based on observed SEDs. This figure shows that different wavelengths trace different regions of an AGN. The radio band corresponds to the jet, the IR is sensitive to the dusty torus, the optical/UV is sensitive to the accretion disk and the X-ray is sensitive to the ionised reflection. Note that the dust component is coming from the AGN, not the host galaxy.

surveys, as is illustrated in Figure 1.10. The X-ray band traces the emission of the hot corona and the ionized reflection of the X-ray continuum from distant neutral material like the molecular torus, the BLR and NLR or the accretion disk (Antonucci, 1993; George & Fabian, 1991; Jaffe et al., 2004; Meisenheimer et al., 2007; Bianchi et al., 2008). The soft X-ray is also sensitive to attenuation by electrons (Padovani et al., 2017). The hard X-ray in theory should be able to select all AGN types, however, has a tendency to miss low-luminosity AGNs. X-ray variability can be used to distinguish AGN and star forming galaxies (Padovani, 2016).

The optical and UV bands probe emission from the accretion disk and fast moving gas (1000 - 10,000 km $\sec^{-1}$) in the BLR (Padovani et al., 2017), but the UV and optical emission from these regions can be obscured by dust. Colour and emission line ratios are two ways in which AGNs can be selected in the optical and UV. Emission line ratios measured using optical spectra can be used to select AGNs from star forming galaxies, where emission line ratios are dependent on the temperature and density of the gas, and the UV spectrum incident upon it. This can be done using a Baldwin, Phillips and Terlevich diagram (BPT diagram; Baldwin et al., 1981).

The IR wavelength range is sensitive to thermal emission from warm and hot dust, which is often attributed to the torus that can obscure the ultraviolet and optical emission (e.g. Padovani et al., 2017). AGNs that can be selected using the IR include both obscured and unobscured AGNs (type 1 and type 2 AGNs) including extremely obscured AGNs that aren't picked up by optical and X-ray surveys. IR selection of AGNs is typically done using IR colours, such as a *WISE* colour selection (e.g. Jarrett et al., 2011; Stern et al., 2012; Assef et al., 2013). IR colour can distinguish AGNs from star forming galaxies and passive galaxies, it also provides relatively high completeness for shallow surveys (Padovani et al., 2017; Yao et al., 2020).

1.4.3 Changing look AGNs (CLAGNs)

Changing look AGNs (CLAGNs) are Seyferts and quasars where the spectra varies from broad line to narrow line on time scales of tens of years (e.g. Denney et al., 2014; Shappee et al., 2014; Guo et al., 2016; Oknyansky et al., 2017; Ross et al., 2018; Noda & Done, 2018). This timescale for change is three orders of magnitude smaller than what one might expect. That is, given the size of the torus is on the order of 1 pc and the relevant velocities are $< 10^4$ km s^{-1}, one might expect CLAGNs to take $\sim 10^3$ years to evolve.

There are two main reasons why we observe changes in spectra. The first reason AGNs change type is due to changes in the central engine. That is, changes in accretion rate of the central black hole, changes in the accretion disk structure, or tidal disruptions (Dexter & Agol, 2011; Kelly et al., 2011; Kokubo, 2015; MacLeod et al., 2016). This scenario is complicated since it challenges the unified model of AGNs as the orientation of the AGN remains the same even though the spectrum does not. The second reason is that an obscuring cloud crosses the line of sight, causing changes in observed light curves (e.g., Goodrich, 1989; LaMassa et al., 2015; Guo et al., 2016). In the latter scenario, light from the inner disk is obscured by the cloud such that it blocks light from the broad-line region causing broad lines to disappear. The IR emission remains unchanged in this scenario as it is unaffected by dust obscuration.

The most common method by which studies have identified CLAGNs is by serendipity. An example of this is NGC 2617, which was identified after an outburst triggered a transient source alert (Shappee et al., 2014). However, more recently, targeted searches for CLAGNs have been conducted with the release of more readily available archival data and multi-epoch photometry such as SDSS (Eisenstein et al., 2011), NEOWISE (Mainzer et al., 2014), GAIA (Gaia Collaboration et al., 2016), SkyMapper (Wolf et al., 2018) and Pan-STARRS (Chambers et al., 2019). Targeted searches for CLAGN include LaMassa et al. (2015), MacLeod et al. (2016), Ruan et al. (2016), Runnoe et al. (2016), Gezari et al. (2017), Yang et al. (2018), Stern et al. (2018) and MacLeod et al. (2019). These searches mainly focus on detecting CLAGNs that are beyond $z \sim 0$. Yang

et al. (2018) and Stern et al. (2018) look for variability in *WISE* IR photometry to select CLAGN candidates, while MacLeod et al. (2019) looked for variation in optical photometry, where the change in photometry is linked to changes in spectral type. A more thorough discussion of CLAGNs and CLAGN studies can be found in Chapter 2.

1.4.4 Probing Galaxy Properties using Spectroscopy.

AGN candidates can be identified from imaging (eg. colour selection), however, spectroscopic follow-up is required to unambiguously identify AGNs. That is, to determine their spectral classes and to determine their redshifts. In this thesis we use a combination of archival and new, slit, fibre and IFU spectroscopy. We go into some more detail on this in the paragraphs below.

Fibre-fed spectrographs are used by large scale spectroscopic surveys such as the SDSS (York et al., 2000), the Two-degree-Field Galaxy Redshift Survey (2dF-GRS, Colless et al., 2001) and GAMA (Driver et al., 2011; Wright et al., 2016), and are able to classify a large number of galaxies based on their spectral type at once. Despite this, single optical fibre surveys suffer from significant limitations at low redshift. Large, nearby galaxies often span several arcminutes, therefore a small fibre (of several arcseconds) will only be able to capture nuclear spectra, missing important information on the disk and outer regions of the galaxy (e.g. Pracy et al., 2014; Davies et al., 2015). This limitation is referred to as aperture bias and it limits the ability to study nearby galaxies spectroscopically.

Long slit spectroscopy allows astronomers to gain both spatial and spectral information along one axis of an extended source. However, it cannot provide information about the entire galaxy at once. Surveys such as the SAGES Legacy Unifying Globulars and Galaxies Survey (SLUGGS, Brodie et al., 2014) have obtained 2D spatial spectroscopy by placing a slit at different orientations over the same galaxy, but this is observationally expensive. The solution is to use integral field spectroscopy (IFS) as this technique provides full spatial spectroscopy for extended objects with one pointing.

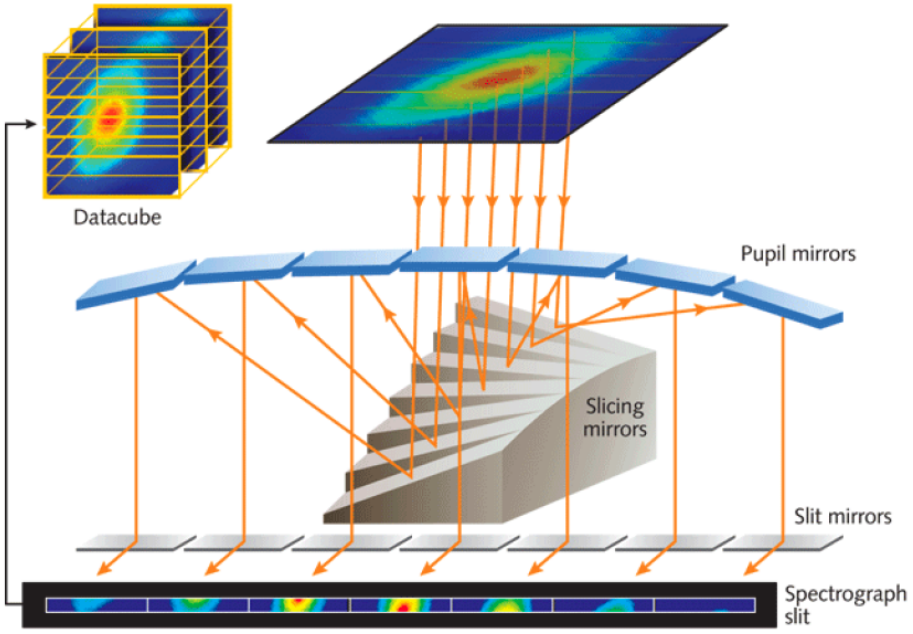

FIGURE 1.11: Schematic of an image-slicing IFU setup. The mirrors slice the images, then the gratings further slit the spectra into two dimensions. Image credit: Durham University.

IFS is a technique that involves capturing multiple spectra of a single galaxy at once across a two-dimensional field of view. Integral field units (IFUs) divide the galaxy up into individual spatial pixels or spaxels, which allows astronomers to study and resolve specific regions of galaxies. There are several different types of IFUs, including image slicing IFUs and fibre-fed IFUs, as displayed in Figure 1.11. Image slicing IFUs use mirrors to segment an image into thin horizontal strips, then rearranges them end to end to form the slit of the spectrograph. The advantage of using an image slicing IFU is that it provides spatial coverage with adjoining borders and therefore only one pointing is necessary to observe the entire object in the field of view. Fibre-fed IFUs consist of bundles of fibre which take regions of a focal plane and rearranges them along a fibre slit. The disadvantage of fibre-fed IFUs is that unlike image slicing IFUs, it does not cover the entire focal plane and thus a dithering pattern is necessary for continuous coverage of the entire focal plane.

Chapter 2 of this thesis uses IFS taken from the Wide Field Spectrograph

(WiFeS: e.g., Dopita & Sutherland, 2003) IFU on the Australian National University's 2.3 m telescope at Siding Spring. WiFeS is an image slicing IFU and has a field of view of $25'' \times 38''$, divided into 950 spaxels. The wavelength coverage is $3500 - 9200$ Å which covers optical wavelengths (Dopita et al., 2010). In particular this wavelength coverage spans emission lines such as Hα (6563 Å) and Hβ (4861 Å), which are ideal for identifying intermediate Seyfert types.

1.5 The Luminosity Function of AGNs

The space density of AGNs provides a constraint on the number of accreting SMBHs and the rate at which they accrete (e.g. Yu & Tremaine, 2002; Falcón-Barroso et al., 2006; Fabian, 2012; Yang et al., 2012; Wang et al., 2013). The luminosity function of AGNs is the number of AGNs per unit volume at a given luminosity (e.g. Peterson, 1997, and references therein). Therefore, the AGN luminosity function and its evolution over cosmic time can be used to measure black hole accretion histories (e.g. Schmidt, 1968; Mathez, 1978; Schmidt & Green, 1983; Koo & Kron, 1988; Brown et al., 2006; Kulkarni et al., 2019).

Some of the earliest quasar luminosity functions were measured by Schmidt & Green (1983), Boyle et al. (1988), Koo & Kron (1988), Hewett et al. (1993), Warren et al. (1994) etc. These luminosity function measurements established the rapid evolution of quasars and a peak at $z \approx 2.5$ for the most luminous quasars. This is also seen in more recent AGN luminosity functions measured using the optical, radio and X-ray (e.g. Dunlop & Peacock, 1990; Ueda et al., 2003; Croom et al., 2004; Richards et al., 2006a; Ross et al., 2013; Retana-Montenegro & Röttgering, 2020). These luminosity functions are parameterized by a broken power law which peaks at $z \sim 2$ - 3. The luminosity at this redshift range is approximately characterised by pure luminosity evolution. The population of quasars at this redshift range are becoming less luminous with time. X-ray surveys such as Hasinger et al. (2001) and Giacconi et al. (2002), which look at fainter AGNs, demonstrated that pure luminosity evolution fails to explain redshift-dependent evolution of AGNs when the AGN luminosity is less than L^* (the luminosity at which the AGN luminosity function flattens). These studies

TABLE 1.1: Some luminosity functions from the literature

Study	Band	Sample size	redshift range	bright power-law index (α)
Boyle et al. (2000)	Optical	5057	$0.35 < z < 2.3$	-3.41
Ueda et al. (2003)	Hard X-ray	246	$0.0 < z < 3$	-3.37
Croom et al. (2004)	Optical	15830	$0.4 < z < 2.1$	-3.31
Richards et al. (2005)	g-band	5645	$0.4 < z < 2.1$	-3.28
Brown et al. (2006)	IR	183	$1 < z < 5$	-2.75
Croom et al. (2009)	Optical	10637	$0.4 < z < 2.1$	-3.38
Ross et al. (2013)	Optical		$0.3 < z < 2.2$	-3.37
Tuccillo et al. (2015)	Optical	87	$3.6 < z < 4.4$	-2.3
Singal et al. (2016)	IR	$\approx$ 20,000	$z < 4.5$	-3.9
Niida et al. (2020)	Optical	224	$z \sim 5.0$	-3.94
Retana-Montenegro & Röttgering (2020)	Optical	5646	$1.4 < z < 5.0$	-3.55
Shen et al. (2020)	Bolometric		$z < 0.2$	-2.75
Onken et al. (2021)	UV	119	$4 < z < 5.5$	-3.84 at $z \sim 5$
Zhang et al. (2021)	Lyα	18320	$2.0 < z < 3.5$	-3.06
This work	IR	1199	$z < 0.35$	-2.75

showed that the peak of the AGN luminosity function occurred at lower redshifts compared to where the peak occurs for more luminous AGN luminosity functions and this finding has been described as AGN downsizing (e.g. Barger et al., 2005).

Boyle et al. (2000), Croom et al. (2004), Richards et al. (2005) Richards et al. (2006a) and Singal et al. (2016) use some of the largest samples of AGNs to measure luminosity functions in the optical/UV, X-ray and IR. Richards et al. (2006a) measure the optical luminosity function of a large, homogeneous sample of luminous type 1 quasars which cover the entire range of observable quasar redshifts. Richards et al. (2006a) use a subset of the SDSS DR3 data, carefully selected to maximise homogeneity. This sample consists of $\sim$ 15,000 quasars selected over $\sim$ 1600 deg^2 with 15.0 mag $< i <$ 19.1 mag and $0.0 \lesssim z \lesssim 3.0$, extending to $i < 20.2$ mag for higher redshift quasars up to $z \sim 5$. We present the Richards et al. (2006a) luminosity function results in Figure 1.12. Richards et al. (2006a) compare their DR3 measurements to previous works from Wolf et al. (2003), Richards et al. (2005), Croom et al. (2004), Ueda et al. (2003), Hunt et al. (2004), Barger et al. (2005), Hasinger et al. (2005) and Meiksin (2005).

We provide luminosity functions from the literature in Table 1.1. The low redshift optical luminosity functions mentioned in Table 1.1 (Boyle et al., 2000; Croom et al., 2004; Richards et al., 2005; Ross et al., 2013) agree to within a bright end power law index of 0.13 and emphasizes the complexity of parameterizing a sample that covers such a large range of redshifts and luminosities.

Richards et al. (2006a) find that the slope of the quasar luminosity function is flattening with increasing redshift. This has been seen before by quasar luminosity function measurements that use smaller samples of high redshift quasars (e.g. Schmidt et al., 1995; Fan et al., 2001). However Richards et al. (2006a) find this for a much larger redshift range than any other previous study. This finding is in direct contrast to that of Wyithe & Loeb (2003) and Hopkins et al. (2006) who use models to construct the space density, as they find that the slope of the luminosity function is steeper at higher redshifts than at low redshifts. Hopkins et al. (2006) determined the evolution to high redshift by adjusting the break in their luminosity for their $0 < z < 3$ model to fit the existing high redshift data. Richards et al. (2006a) state that in order for the Hopkins et al. (2006) to match their observed flattening at high redshift, Hopkins et al. (2006) will either need to change their model or the method by which their models extrapolate to higher redshifts.

1.6 Supermassive Black Hole Accretion History

Most massive galaxies have a supermassive black hole (SMBH) in the centre (e.g. Rees, 1984; Begelman, 1989; Magorrian et al., 1998; Ho, 1999) and these SMBHs grow through mass accretion where the host galaxies' gas loses angular momentum and accretes onto the black hole. This releases energy in the form of radiation across the entire electromagnetic spectrum, as well as winds and radio plasma jets (e.g. Elvis et al., 1994). Some of this released energy is fed back into the galaxy, leading to the heating of inflowing gas and resulting in the truncation of star formation (Silk & Rees, 1998; Fabian, 1999a). This process is called AGN feedback.

There are at least two major modes of energy that contribute to AGN feedback and energy outflow near the black hole. The first of these is the radiative mode (also known as the quasar wind mode); which operates in a bulge where the accreting black hole is close to the Eddington limit (Fabian, 2012). Rapid accretion onto the central black hole drives energy outflows, which can lead to the expulsion of gas from the galaxy and truncate star formation (e.g. Tabor &

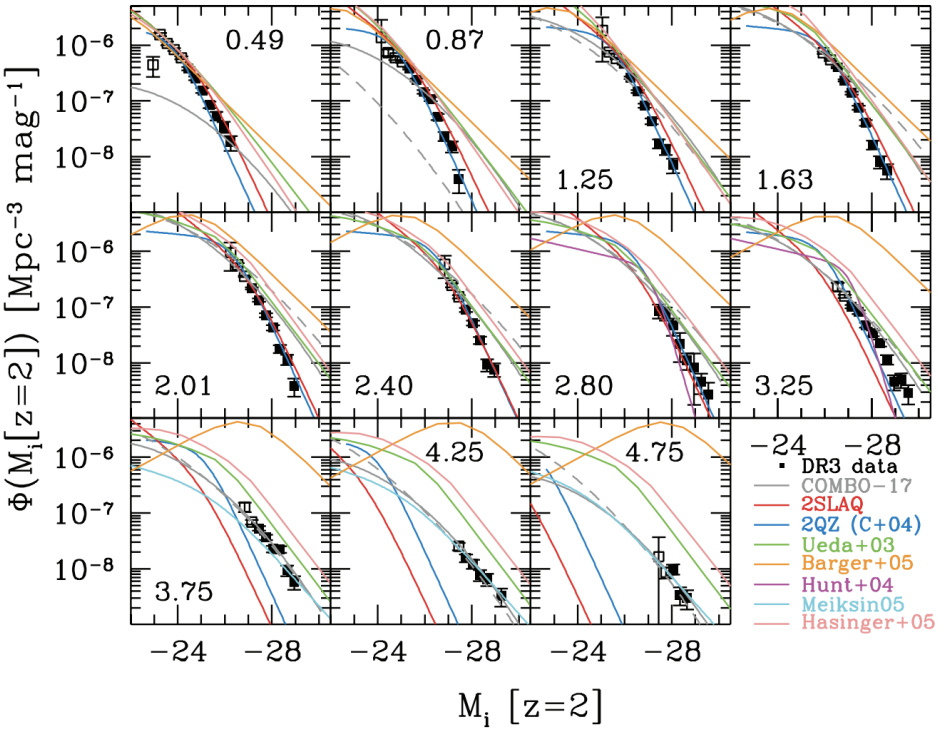

FIGURE 1.12: SDSS data release 3 optical quasar luminosity function from Richards et al. (2006a). They compare their DR3 measurements to previous works from Wolf et al. (2003), Richards et al. (2005), Croom et al. (2004), Ueda et al. (2003), Hunt et al. (2004), Barger et al. (2005), Hasinger et al. (2005) and Meiksin (2005) and find that their DR3 data matches most with that of Ueda et al. (2003). This figure shows that even at low redshifts, measured luminosity function can have a range of-power law indices, and this may suggest some bright AGNs are missing from some samples.

Binney, 1993; Silk & Rees, 1998; Fabian, 1999b; Chartas et al., 2003; Fabian, 2012). This form of feedback is potentially driven by galaxy mergers which drive gas towards the centre of the merged galaxy, feeding the black hole and hence triggers accretion and outflows (e.g. Springel et al., 2005, and references therein). At higher redshifts ($z \sim 2$), the radiative mode may be sufficient to explain the shape of the galaxy luminosity function (van Dokkum et al., 2010).

The second mode is the kinematic mode (radio mode), it operates in galaxies which have a hot halo and the accreting black hole has powerful jets. This occurs in galaxies with lower Eddington fraction with high masses (Fabian, 2012). Although radiative feedback mode is sufficient to explain the luminosity functions of high redshift quasars, it alone cannot account for the discrepancies in the observed and simulated luminosity function for high mass galaxies. In the

kinematic mode, cooling gas that may accrete onto the black hole is heated in large galaxies ($\log(M\ [M_\odot]) > 11$) (Fabian, 1999a, 2012). This mode of AGN feedback scales with galaxy mass (e.g. Sadler et al., 1989; Pimbblet et al., 2013) and may explain the cause of quenching of star formation in massive galaxies.

The relationship between dark matter halo mass and galaxy stellar mass provides indirect evidence for AGN feedback (e.g. Zheng et al., 2007; Yang et al., 2012; Wang et al., 2013). This is illustrated in Figure 1.13 from Mutch et al. (2013). It shows the difference between the observed galactic stellar mass function (Bell et al., 2003) and the halo mass function of the Millennium Simulation (Springel et al., 2005). The closer the stellar mass function is to the Millennium Simulation, the more efficient star formation is in the halo. The discrepancy in the observed galactic stellar mass function and the Millennium Simulation at high and low masses indicates that star formation is less efficient at these masses. At the higher mass end ($\log(M\ [M_\odot]) \gtrapprox 11.0$) this is thought to be as a result of AGN feedback where energy fed back into the SMBH heats gas that would otherwise cool and form stars.

Given AGNs are powered by accretion, the bolometric luminosities of AGNs can be used to directly measure the mass inflow rate into a black hole dM/dt, $\epsilon\ \dot{M}_{BH} = L_{bol}/c^2$, that is the accretion rate of a black hole (ϵ is the radiative efficiency of the accretion energy). This can be expressed as:

$$\dot{M}_{BH} = 1.76 \times 10^5 (0.1/\epsilon)(L_{bol}/10^{42}) \tag{1.2}$$

with $\dot{M}_{BH}$ in units of $M_\odot$ Gyr^{-1} and L_{bol} (bolometric luminosity) in units of erg s^{-1} (Barger et al., 2001). This is illustrated in Figure 1.14 which shows the black hole accretion rate density, measured in the hard X-ray, as a function of redshift by Barger et al. (2001). The upper bound is measured using the bolometric luminosity which is measured using the IR, radio and hard X-ray, and the lower band is measured using X-ray luminosities. The accretion rate densities are on average a factor of 20 higher when measured using bolometric luminosities compared to X-ray luminosities alone. The shape of the accretion rate density roughly follows a $(1 + z)^3$ line. This redshift dependence is similar

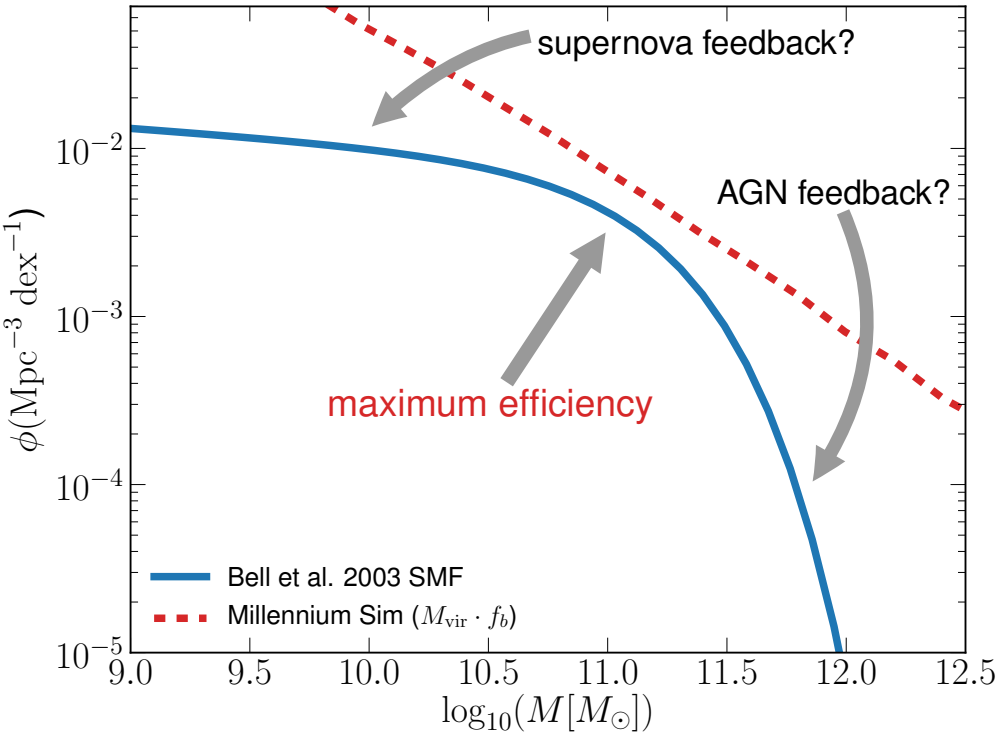

FIGURE 1.13: The observed galactic stellar mass function (Bell et al., 2003) compared to the halo mass function of the Millenium Simulation (Springel et al., 2005) from Mutch et al. (2013). Star formation in the halo is more efficient with the stellar mass function is closer to the simulation, where the discrepancy at the higher mass end ($\log(M\ [M_\odot]) > 11.0$) may be the result of AGN feedback.

to the inferred dependence in star formation histories (Lilly et al., 1996; Cowie et al., 1999; Wilson et al., 2002). Therefore, an accurate accretion history is dependent on carefully derived bolometric corrections.

1.7 Thesis aims

The goals of this thesis are to a) detect AGNs that were potentially missed by previous surveys, b) precisely measure the AGN luminosity function and c) to improve measurements of the cosmic accretion history. Specifically, we investigate the following:

- We search for AGNs missed by previous surveys by conducting a systematic search to find CLAGNs. To do this we use optical colour, optical variability

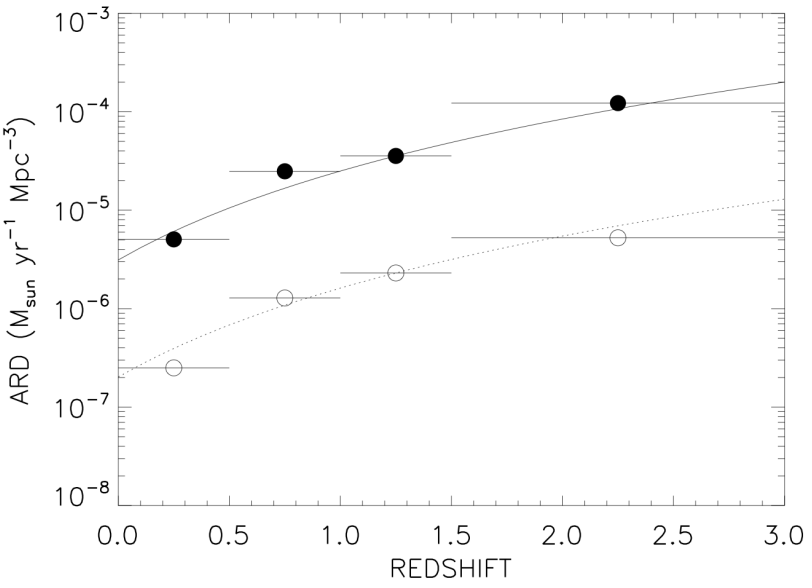

FIGURE 1.14: Accretion rate density of black holes as a function of redshift from Barger et al. (2001). The upper line is the accretion rate density measured using bolometric luminosity which is measured using the IR, radio and hard X-ray, and the lower line is accretion rate density measured using X-ray luminosities.

and mid-IR variability to preselect $z < 0.04$ CLAGNs for spectroscopic follow-up.

- We determine the relationship between monochromatic luminosity and bolometric luminosity, improving on prior literature in wavelength coverage and methods.

- We measure the IR AGN luminosity function, which measures emission from warm dust (attributed to the torus) and is relatively insensitive to obscuration, using *WISE* imaging and the GAMA spectroscopic survey (Hopkins et al., 2013; Cluver et al., 2014). We then measure the accretion rate density of the local Universe ($z < 0.35$) using our IR bolometric corrections and luminosity function.

Chapter 2

A Systematic Survey for z < 0.04 Changing-Look AGNs

This Chapter almost identically replicates the original publication (Senarath et al., 2021) which can be found here. Some tables have been edited for improved readability. Some text has also been modified or added based on feedback from thesis examiners.

Authors:

Madhooshi R. Senarath,[1] Michael J. I. Brown,[1] Michelle E. Cluver,[2,3] Thomas H. Jarrett,[5] Christian Wolf,[4] Nicholas P. Ross,[6] John R. Lucey,[7] Vaishali Parkash,[1] Wei J. Hon.[8]

Affiliations:

[1]School of Physics and Astronomy, Monash University, Clayton, Victoria 3800, Australia

[2]Centre for Astrophysics and Supercomputing, Swinburne University of Technology, Hawthorn, Victoria, 3122, Australia

[3]Department of Physics and Astronomy, University of the Western Cape, Robert Sobukwe Road, Bellville, 7535, South Africa

[4]Research School of Astronomy and Astrophysics, Australian National University, Canberra, ACT 2611, Australia

[5]Department of Astronomy, University of Cape Town, Private Bag X3, Rondebosch, 7701, South Africa

[6]Institute for Astronomy, University of Edinburgh, Royal Observatory, Blackford Hill, Edinburgh EH9 3HJ, United Kingdom

[7] Centre for Extragalactic Astronomy, University of Durham, Durham DH1 3LE, United Kingdom

[8] School of Physics, University of Melbourne, Parkville, Victoria 3010, Australia

2.1 Abstract

We have conducted a systematic survey for $z < 0.04$ active Galactic nuclei (AGNs) that may have changed spectral class over the past decade. We use SkyMapper, Pan-STARRS and the Véron-Cetty & Véron (2010) catalogue to search the entire sky for these "changing-look" AGNs using a variety of selection methods, where Pan-STARRS has a coverage of 3π steradians (sky north of Declination $-30°$) and SkyMapper has coverage of $\sim$ 21,000 deg^2 (sky south of Declination 0°). We use small aperture photometry to measure how colour and flux have changed over time, where a change may indicate a change in spectral type. Optical colour and flux are used as a proxy for changing Hα equivalent width, while *WISE* 3.4 μm flux is used to look for changes in the hot dust component. We have identified four AGNs with varying spectra selected using our optical colour selection method. Three AGNs were confirmed from recent observations with WiFeS on the 2.3 m telescope at Siding Spring and the other was identified from archival spectra alone. From this, we identify two new changing look AGNs; NGC 1346 and 2MASX J20075129-1108346. We also recover Mrk 915 and Mrk 609, which are known to have varying spectra in the literature, but they do not meet our specific criteria for changing look AGNs.

2.2 Introduction

The classic dichotomy of Active Galactic Nuclei (AGNs) classifies their optical spectra as having either broad or narrow emission lines, type 1 and type 2,

respectively, with some intermediate classes containing both emission line components (Seyfert, 1943; Weedman, 1976; Osterbrock, 1977, 1981). The widely used unified model of AGNs proposes that observed AGN type/classes are a single type of object, observed at different orientations along the line of sight (Osterbrock, 1989; Antonucci, 1993). We can directly observe both the broad line region (BLR) and narrow line region (NLR) in type 1 Seyferts. Whereas, in type 2 Seyferts, the light from the broad line region is absorbed by the dusty torus and is not visible in the optical (although it is observable in the IR), while the light from the narrow line region is scattered. Intermediate type 1 Seyferts can have both narrow and broad emission lines, type 1.5 Seyferts have narrow lines with obvious broad Hα and Hβ components, type 1.8s have narrow lines with a broad Hα component and a recognisable broad Hβ component and type 1.9s contain narrow lines with only Hα line being broad (Osterbrock, 1977, 1981).

Different wavelengths probe different regions of an AGN. The infrared (IR) wavelength range is sensitive to thermal emission from warm dust, which is often attributed to the torus that can obscure the ultraviolet and optical emission (e.g., Padovani et al., 2017). The optical and ultraviolet (UV) bands probe emission from the accretion disk and fast moving gas (1000 - 10,000 km sec^{-1}) in the BLR, but the UV and optical emission from these regions can be obscured by dust. The X-ray band traces the emission of the hot corona and the ionized reflection of the X-ray continuum from distant neutral material like the molecular torus, the BLR and NLR or the accretion disk (Antonucci, 1993; George & Fabian, 1991; Jaffe et al., 2004; Meisenheimer et al., 2007; Bianchi et al., 2008). X-rays from AGNs are believed to be a result of inverse Compton scattering of the photons in the accretion disk by the hot corona.

Changing-look AGNs (CLAGNs) are Seyferts and quasars where the spectral type changes from broad line to narrow line and vice versa. Given that the size of the torus is on the order of 1 pc and the relevant velocities are $< 10^4$ km s^{-1}, one might expect CLAGNs to take $\sim 10^3$ years to change spectral class in the optical. We may expect variability on the viscous timescale, which for AGNs is on the order of $\sim 10^3 - 10^5$ years (Siemiginowska et al., 1996). However Tohline

& Osterbrock (1976), Penston & Perez (1984), Tran et al. (1992a), Storchi-Bergmann et al. (1993), Eracleous & Halpern (2001), Marchese et al. (2012), Marin et al. (2013), Denney et al. (2014), Shappee et al. (2014), Guo et al. (2016), Oknyansky et al. (2017), Ross et al. (2018), Noda & Done (2018) and Hon et al. (2020) for example, have identified CLAGNs that change spectral type in only a few years. CLAGNs may therefore be more common than previously believed.

Examples of low redshift CLAGNs from the literature include Mrk 833 (Canelo et al., 2018), which changed from type 1.9 to type 1.8, NGC 7603 (Tohline & Osterbrock, 1976), which changed from type 1 to type 1.5, Mrk 372 (Penston & Perez, 1984), which changed from type 1.5 to type 1.9 and NGC 1566 (Oknyansky et al., 2018), which changed from type 1.9 to type 1.2. Mrk 1018 is an example of a CLAGN that has changed type multiple types in the past 30 years from a type 1.9 to 1 over the course of < 5 years (Osterbrock & Koski, 1976) and back to a type 1.9 (McElroy et al., 2016). Another example of a CLAGN that changed type multiple times are Mrk 590, which changed from a type 1.5 to 1.0 from 1973 to 1989 and the spectra obtained in 2014 contained no evidence of broad lines (Osterbrock, 1977; Denney et al., 2014). NGC 4151 also changed from a type 1.5 to 2 back to having broad lines (Osterbrock, 1977; Antonucci & Cohen, 1983; Shapovalova et al., 2010).

While there isn't a strict definition in the literature, for consistency with the literature we classify objects as CLAGN if the broad line components completely disappears, a new broad line component appears and/or if the Osterbrock (1977) and Osterbrock (1981) spectral type changes by more than 0.1 (that is a change from type 1.8 to 1.9 and 1.9 to 2.0 and vice versa is not significant enough to be classified as a CLAGN). Some objects in our sample do show interesting spectral variability while falling below our CLAGN thresholds, and we retain them in this work while not classifying them as CLAGNs. AGNs such as Mrk 883, which change type by only 0.1 do not meet our CLAGN criteria, however it is considered an CLAGN by Canelo et al. (2018).

2.2.1 Why CLAGN change spectral type

There are two main reasons why AGNs change their spectral type. One scenario is an obscuring cloud crosses the line of sight, causing changes in observed light curves. Goodrich (1989) and Guo et al. (2016) have found AGNs which vary due to obscuring clouds. In this case, light from the inner disk and BLR is obscured by the dusty cloud, causing broad lines to disappear from the spectra. IR emission is sensitive to thermal emission from warm dust, which is often attributed to the torus, as the change in spectral type in this scenario is caused by obscuration of the BLR, we do not expect to measure a change in IR. Thus, the spectra of the AGNs should return to their original state after a period of time. A likely example of such a CLAGN is quasar SDSS J231742.60+000535.1 (Guo et al., 2016), where the change in its spectral type was caused by rapid outflow or inflow with an obscuring cloud passing along the line of sight. This scenario is in agreement with the unified model as changes in the spectral type are due to changes along the line of sight.

The second and more complex cause for change in spectral type is due to changes in accretion rate of the central black hole, changes in accretion disk structure, or tidal disruptions (Dexter & Agol, 2011; Kelly et al., 2011; Merloni et al., 2015; Kokubo, 2015; MacLeod et al., 2016). Ross et al. (2018) use models of the innermost stable circular orbit around a black hole to determine if this is a possible driver for changes in the spectra of SDSS J1100-0053, where the different models have combinations of zero torque, non-zero torque, spectral hardening factor[1] and radii. Ross et al. (2018) attributed the change in spectral type to mass flow rate switching from cold, high mass flow rate to hot, low mass flow rate. Kubota & Done (2018) have also developed a new spectral model for the broad band SED of AGNs which includes the outer disk, an optically thick region, warm Comptonizing electrons and an inner region that emits the X-ray component of the power law. They calculate the optical variability resulting from a stochastic change in X-ray flux which predicts that the fast variability in the optical should be a decreasing function of the Eddington fraction. This

[1]The spectral hardening factor, also referred to as the color correction, is used to interpret multi-temperature black body fitting results (Davis & El-Abd, 2019). Where for a canonical blackbody spectral, the spectral hardening factor is 1.

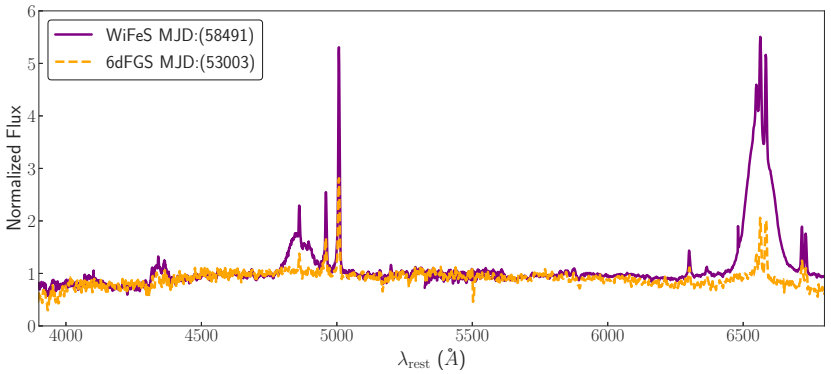

FIGURE 2.1: Spectra of NGC 2617, a previously identified CLAGN with still evolving spectra from type 1.8 to type 1 Seyfert (Oknyansky et al., 2017). Véron-Cetty & Véron (2010) identify the 6dFGS spectrum as type 1.8, while our WiFeS 2019 January shows NGC 2617 is currently a type 1, which agrees with observations from Oknyansky et al. (2017).

finding matches some of the trends seen in systematic surveys for varying AGN (e.g., MacLeod et al., 2010). Unlike the previous scenario, the change in spectral type is caused by changes in accretion. Thus, it does not agree with the unified model as the spectral type change is not caused by changes along the line of sight.

2.2.2 Known CLAGNs

Until recently, the most common method by which studies have identified CLAGNs is by serendipity. For example, NGC 2617 is a CLAGN that was identified by Shappee et al. (2014) after an outburst triggered a transient source alert, and the corresponding changing optical spectra are displayed in Figure 2.1. NGC 2992 was identified by Gilli et al. (2000) using *Beppo*SAX observations (Scarsi, 1997) which caught a rise in nuclear emission from the AGN, and there was a corresponding change in the optical classification from type 1.9 to type 2.

It is only recently that targeted searches for CLAGNs such as LaMassa et al. (2015), MacLeod et al. (2016), Ruan et al. (2016), Runnoe et al. (2016), Gezari et al. (2017), Yang et al. (2018), Stern et al. (2018) and MacLeod et al. (2019) have been conducted. This is because there is now more readily available archival

data and multi-epoch photometry such as NEOWISE (Mainzer et al., 2014), Pan-STARRS (Chambers et al., 2019), SDSS (Eisenstein et al., 2011), SkyMapper (Wolf et al., 2018) and GAIA (Gaia Collaboration et al., 2016). These targeted searches are focused mainly on detecting changing-look quasars that are well beyond $z \sim 0$. That said, a number of changing-look Seyferts have been identified in the $z < 0.04$ Universe, and these and their key details including previous and current type are summarised in Table 2.1. The CLAGNs in Table 2.1 were identified by serendipity or X-ray monitoring of known AGNs.

TABLE 2.1: Known $z < 0.04$ CLAGNs and their respective types and references.

ID	Ra(J2000)	Dec(J2000)	redshift	Previous type(s)	Current type	Reference
NGC 7603	23h18m56.65s	+00d14m37.9s	0.030	1	1.5	Tohline & Osterbrock (1976)
NGC 4151	12h10m32.65s	+39d24m20.7s	0.003	1, 2	1.5	Penston & Perez (1984)
NGC 2622	08h38m10.943s	+24d53m43.02s	0.029	1.8	1	Goodrich (1989)
Mrk 372	03h02m13.18s	-23d35m19.8s	0.035	1.5	1.9	Gregory et al. (1991)
Mrk 993	01h25m31.47s	+32d08m10.5s	0.016	1	1.9	Tran et al. (1992a)
NGC 1097	02h46m19.05s	-30d16m29.6s	0.004	2	1	Storchi-Bergmann et al. (1993)
NGC 3065	10h01m55.30s	+72d10m13.0s	0.007	2	1.2[a]	Eracleous & Halpern (2001)
NGC 2992	09h45m42.04s	-14d19m34.8s	0.008	1.9, 1.5	2	Gilli et al. (2000) & Trippe et al. (2008)
NGC 454E	01h14m22.50s	-55d23m55.0s	0.012		2[b]	Marchese et al. (2012)
NGC 1365	03h33m36.45s	-36d08m26.3s	0.005		1.8[b]	Marin et al. (2013)
Mrk 590	02h14m33.57s	-00d46m00.2s	0.026	1	1.9-2	Denney et al. (2014)
Mrk 6[c]	06h52m12.251s	+74d25m37.46s	0.019	2	1.5	References available in table notes.[c]
ESO 362-G018	05h19m35.80s	-32d39m27.0s	0.012	1.5	2	Agís-González et al. (2017)
NGC 7582	23h18m23.62s	-42d22m14.0s	0.005	1	2	Braito et al. (2017)
NGC 2617	08h35m38.77s	-04d05m17.2s	0.014	1.8	1	Oknyansky et al. (2017)
NGC 1566	04h20m00.41s	-54d56m16.1s	0.005	1.9	1.2	Oknyansky et al. (2018)
Mrk 883	16h29m52.84s	+24d26m37.4s	0.037	1.9	1.8	Canelo et al. (2018)
HE 1136-2304	11h38m51.00s	-23d21m32.0d	0.027	2	1.5	Zetzl et al. (2018)
NGC 3516	11h06m47.490s	+72d34m06.88s	0.009	1	2	Shapovalova et al. (2019)
1ES 1927+654	19h27m19.54s	+65d33m54.2s	0.017	2	1	Trakhtenbrot et al. (2019)
NGC 1346	03h30m13.27s	-05d32m36.3s	0.014	1.8	2	Senarath et al. (2019) & This work
2MASX J20075129-1108346	20h07m51.29s	-11d08m34.6s	0.030	2	1.8	This work

[a] While Eracleous & Halpern (2001) don't explicitly state the spectral types of the changes, they do state that NGC 3065 went from lacking broad Balmer lines to containing broad Balmer lines.

[b] NGC 1365 is an X-ray CLAGN. X-ray CLAGNs are characterised by rapid transitions between Compton-thick to Compton-thin, where this transition can be due to absorption by gas clouds passing along the line of sight or relativistic reflection on to the accretion disk (Marin et al., 2013). In the case of NGC 1365, the CLAGN classification is due to the reflection-dominated scenario.

[c] Khachikian & Weedman (1971), Khachikian et al. (2011) & Afanasiev et al. (2014)

Motivated by the frequency of ad hoc nearby CLAGN identifications, we have conducted a systematic search for $z < 0.04$ CLAGNs. Our redshift limit is chosen to keep Hα within the r band and increases availability of archival photometry and spectroscopy. We use the Véron-Cetty & Véron (2010) catalogue to identify $z < 0.04$ AGNs using SkyMapper (Wolf et al., 2018), the Panoramic Survey Telescope and Rapid Response System (Pan-STARRS, Chambers et al., 2019; Flewelling et al., 2020), the Wide-field Infrared Survey Explorer (*WISE*, Wright et al., 2010) and Sloan Digital Sky Survey (*SDSS*, Abazajian et al., 2004). We select CLAGN candidates meeting our colour and flux criteria, and then follow-up these candidates with archival and new spectroscopy. In Section 2.3 we discuss the methods by which we selected CLAGN candidates and the effectiveness of each method. In Section 2.4 we discuss what objects were observed. In Section 2.5 we discuss the new CLAGNs we identified, including NGC 1346 which we also discuss in Senarath et al. (2019). We also discuss the possible reasons why these AGNs changed spectral type in Section 2.5.

2.3 Candidate selection

To select CLAGN candidates we use photometry from PanSTARRS, SkyMapper and the Wide-field Infrared Survey Explorer (*WISE*, Wright et al., 2010). Our methods use optical and MIR fluxes and colours to search for variability in the optical continuum. Our first approach uses optical colours as a proxy of Hα equivalent widths. Our second and third approaches use variability of optical and MIR fluxes to search for changes in accretion disk and hot dust component respectively.

We use the MIR to identify changes in the dust near the accretion disk of the AGNs (presumably not associated with the larger torus). The optical and UV continuum probes emission from the disk while the optical and UV spectral lines probe ionised gas above the disk, and changes in the optical flux and color may indicate changes in spectral type resulting from changes in accretion or changing obscuration along the line of sight. We use optical colour and infrared fluxes and colours as proxies for Hα emission and hot disk emission respectively,

where variations would indicate the presence of a CLAGN. Therefore, we require photometry of known AGNs (the specifics of this are explained in Section 2.3.1). Following the photometric selection of CLAGN candidates we obtained follow-up spectroscopy.

2.3.1 Imaging surveys and catalogues

We select known $z < 0.04$ AGNs from Véron-Cetty & Véron (2010), an extensive compilation of AGNs (particularly at low redshift). We then measure optical and infrared photometry of these AGNs with SkyMapper, Pan-STARRS, and WISE. Possible CLAGNs are then selected with the colour and flux criteria described Sections 2.3.2, 2.3.3 and 2.3.4. The SkyMapper survey (with passbands *uvgriz*) contains $\approx$ 280 million objects and has a coverage area of almost the entire Southern sky. Pan-STARRS on the other hand, surveys the sky north of Declination -30° (passbands *grizy*). Together the two surveys provide data for the entire sky.

The depth of the optical catalogues are $r \sim 21.7$ mag for SkyMapper and $r \sim 23.2$ mag for Pan-STARRS, which is more than sufficient to detect all the z < 0.04 Véron-Cetty & Véron (2010) AGNs. For our analysis we use small aperture photometry. For Pan-STARRS (PS1) we measure photometry in $3''$ diameter apertures on stack images. For SkyMapper we use the DR1 $5''$ diameter aperture photometry. For SDSS we use the fibre magnitudes ($3''$ in diameter). The Véron-Cetty & Véron (2010) AGNs at z < 0.04 are far brighter than the magnitude limits of all three surveys, thus we expect photometric uncertainties to be < 0.1 mag. The $3''$ and $5''$ diameter apertures at z $= 0.04$ correspond to 1.2 kpc and 2.1 kpc in radius, respectively, so we are measuring the AGNs and the central regions of their host galaxies. To photometrically identify AGNs that may have a varying hot dust component, we use photometry drawn from the *WISE* and NEOWISE surveys (Mainzer et al., 2014). NEOWISE measures photometry in the W1 and W2 bands and surveys the entire sky at a cadence of 6 months, and has been doing so since *WISE* was brought out of hibernation in late 2013. We present a subset of our CLAGN candidate catalogues in Tables 2.2 and 2.3 for

SkyMapper and Pan-STARRS, respectively, which contain all the $z < 0.04$ AGN with information on the selection criteria and whether or not each galaxy meets the criteria. They also contain archival spectra references for the Seyferts that meet the CLAGN candidate criteria.

2.3.2 Optical colour selection

CLAGNs should change colour due to varying Hα strength, thus we use r - i as a proxy for Hα equivalent width. Our optical colour selection assumes that type 1 and type 2 AGNs have relatively blue and red r - i colours, respectively, resulting from the equivalent width of the Hα emission line. As the Pan-STARRS and SkyMapper bands differ from each other, the r - i colours they measure for individual AGNs will differ. As a consequence we compare $z < 0.04$ AGNs that appear in both catalogues, we find a linear relation as a function of r - i colour. We apply this relation when determining our r - i colour criteria for our Pan-STARRS and SkyMapper catalogues.

For our SkyMapper catalogue we select blue Seyfert type 2s with r - $i < 0.35$ mag and red type 1s with r - $i > 0.53$ mag (after removing flagged objects with spurious photometry). For our Pan-STARRS sample we select blue type 2s with r - $i < 0.25$ mag and red type 1s with r - $i > 0.43$ mag (after removing flagged objects with spurious photometry). This selects a total of 109 candidates where we select 40 and 69 AGNs in SkyMapper and Pan-STARRS, respectively. These candidates are displayed in Figure 2.2 and Figure 2.3.

We further refine this candidate list by inspecting the archival images and spectra, including identifying changes in the Hα and Hβ emission lines. We select candidates to observe on the basis that they have more than one archival spectra and there is variation in emission line widths that appear to be changing in the last 10 years (after 2008), these archival spectra are referenced in Tables 2.2 and 2.3. It should be noted that 46% of the candidates selected using the mentioned colour criteria have no readily available archival spectra or have just one readily available spectrum. Also 26% of candidates did not have archival spectra taken

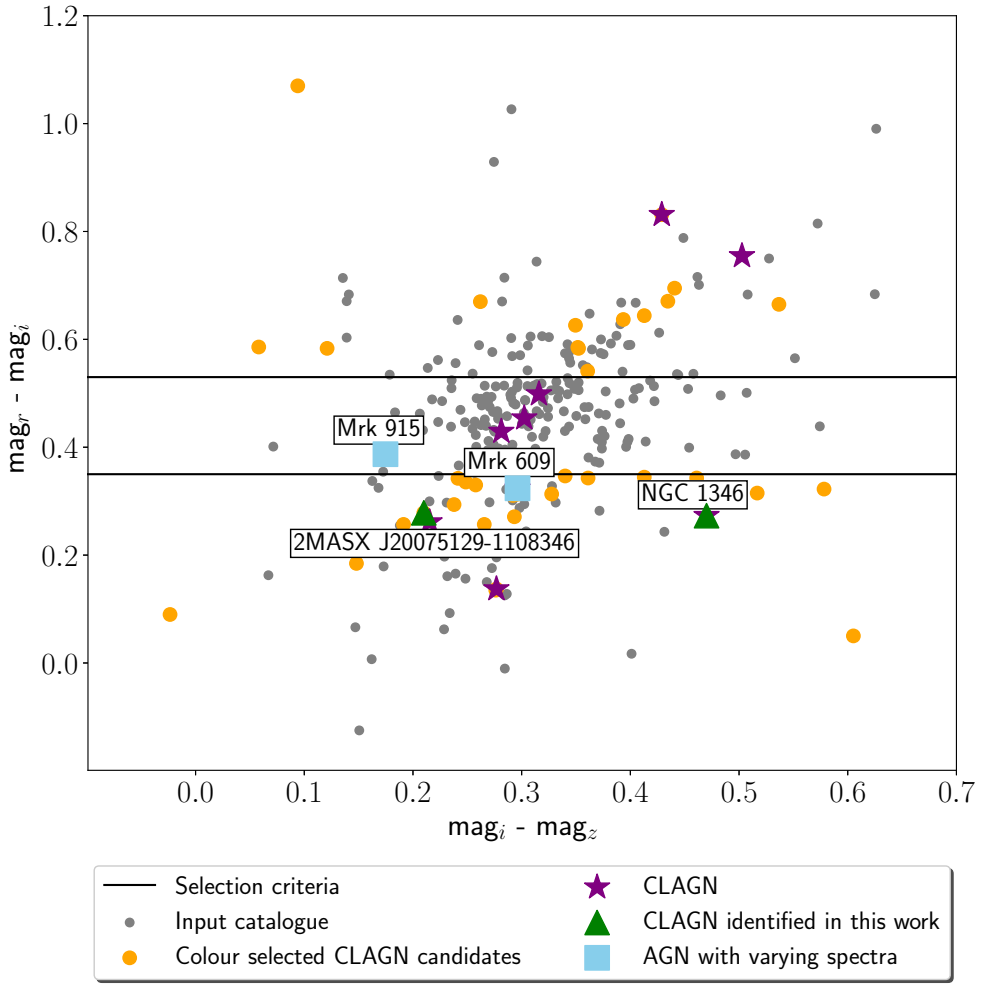

FIGURE 2.2: Skymapper *riz* colours for our CLAGN candidates with the other z < 0.04 AGNs displayed in the background. We select Véron-Cetty & Véron (2010) type 1s with $r - i > 0.53$ mag and type 2s with r - $i < 0.35$ mag as possible CLAGN candidates, these are indicated in orange.

in the last 10 years. AGNs that fall into these categories are not selected for observations.

Of the 22 known $z < 0.04$ changing-look Seyferts, 10 are known to have changed optical spectral class between 1998 and 2015, where 2015 is defined by the end of the SkyMapper observations for the data release we are using (DR1) (Wolf et al., 2018) and 1998 is defined by the beginning of the SDSS imaging we are using (Eisenstein et al., 2011), while Pan-STARRS PS1 data was obtained between 2009 and 2014 (Chambers et al., 2019). Our photometric selection has recovered five of these known CLAGNs; Mrk 883, Mrk 590, NGC 4151, NGC 7282 and NGC 2617 (further information on these CLAGNs appear in Table 2.1).

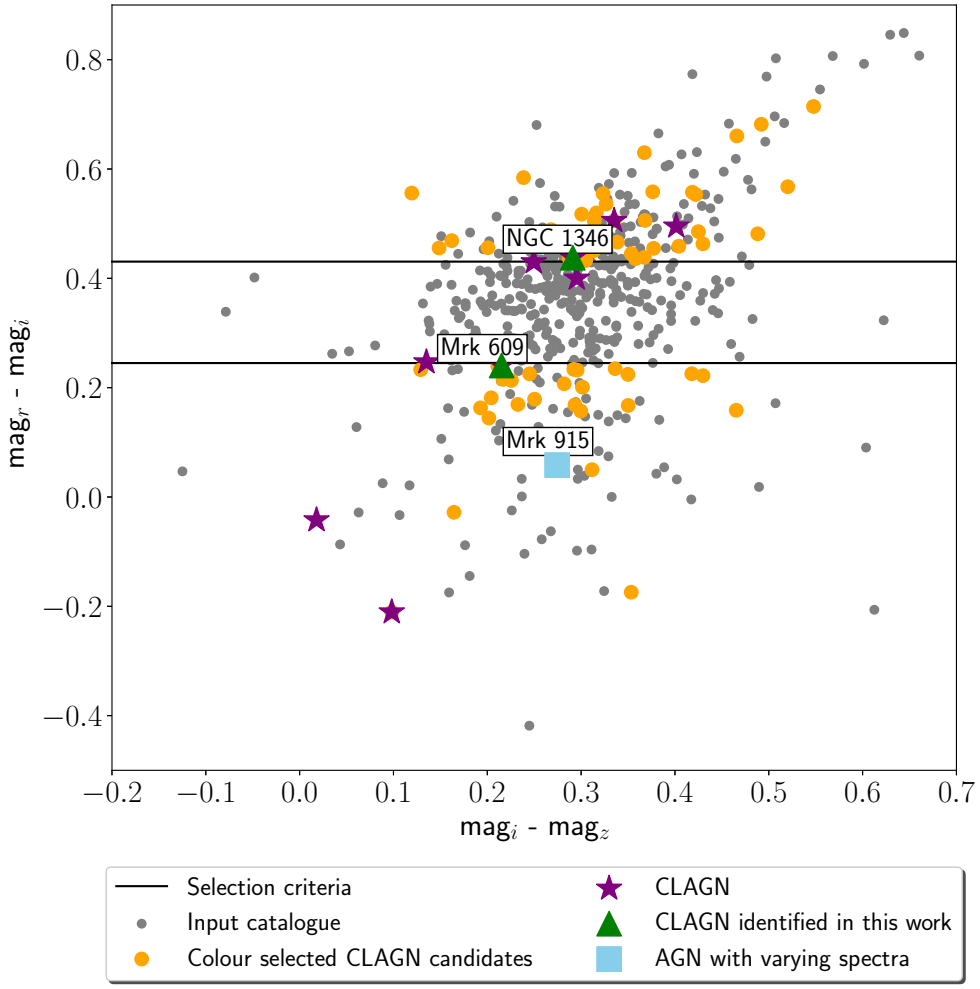

FIGURE 2.3: Pan-STARRS catalogue *riz* colours for our CLAGN candidates with the other z < 0.04 AGNs displayed in the background. We select Véron-Cetty & Véron (2010) type 1s with r - i > 0.43 mag and Véron-Cetty & Véron (2010) type 2, type 1.8 and type 1.9 with r - i < 0.25 mag as potential CLAGN candidates, these are indicated in orange.

2.3.3 Optical flux variability selection

As with r - i colour selection, we utilise the r-band flux variability to detect the changing Hα emission of CLAGNs. As, by definition this requires multiple r band epochs, we have measured the variability of the Véron-Cetty & Véron (2010) z < 0.04 AGNs in the ≈ 14,055 square degrees that have both SDSS and Pan-STARRS photometry. It should also be noted that the time between SDSS and Pan-STARRS observations can be as little as a few years or longer than a decade, while changes in Seyfert spectra can take decades to occur, or in some cases can be limited to just a few years (i.e, tidal disruptions, Guo et al., 2016).

We found that type 1.8s, 1.9s and type 2s typically showed variability $\Delta m_r <$ 0.2 mag, and these are plotted in Figure 2.4. However type 1s showed a greater variability making it impractical to select type 1s fading into type 2 on the basis of r band flux variability alone. Of the 335 type 1.8s, 1.9s and type 2s with both SDSS and Pan-STARRS photometry, we identified 22 potential CLAGNs using $\Delta m_r > 0.2$ mag. It should be noted that as these objects are relatively bright, the photon shot noise is relatively small and the scatter is dominated by PSF differences, zeropoint errors, filter curve differences and AGN variability. The dominant source of error is systematic errors rather than easily quantifiable errors, thus we have not included individual error bars into Figure 2.4, but as we can see the 1σ scatter, quantified by NMAD, is 0.07 mag.

After further investigation of the 22 potential CLAGNs, four CLAGN candidates were removed as their measurement of variability resulted from centroid errors, where two of these AGNs were in galaxy pairs. We also recover the known CLAGNs NGC 2617 (Oknyansky et al., 2017) and Mrk 883. Further inspection into archival spectra of the AGNs with $\Delta m_r > 0.2$ (NGC1048A, SDSSJ03205-0020, Zw497.016, NPM1G-16.0109, MCG+08.15.009, NGC4565, Mrk 1392, Mrk 673, Mrk 609, UGC 4145, Zw098.038, HS1656+3927, NGC6264, Mrk 248 and IC1725) showed all had archival spectra. Inspecting these archival spectra, we found no evidence of variation (no clear appearance or disappearance of broadening). As such, we did not undertake spectroscopic follow up of these AGNs.

2.3.4 Infrared flux variability selection

We use NEOWISE variability to search for $z < 0.04$, Véron-Cetty & Véron (2010) AGNs where the contribution of hot dust to the SEDs may be changing. Unlike optical flux variability selection where we measure the difference between SDSS and Pan-STARRS photometry, in this scenario we measure the change in magnitude over time using different epochs of NEOWISE. Each NEOWISE epoch has multiple photometry measurements, so we use the median photometry measurement for each epoch and measure the difference between the highest and lowest magnitude epochs, we present this in Figure 2.5.

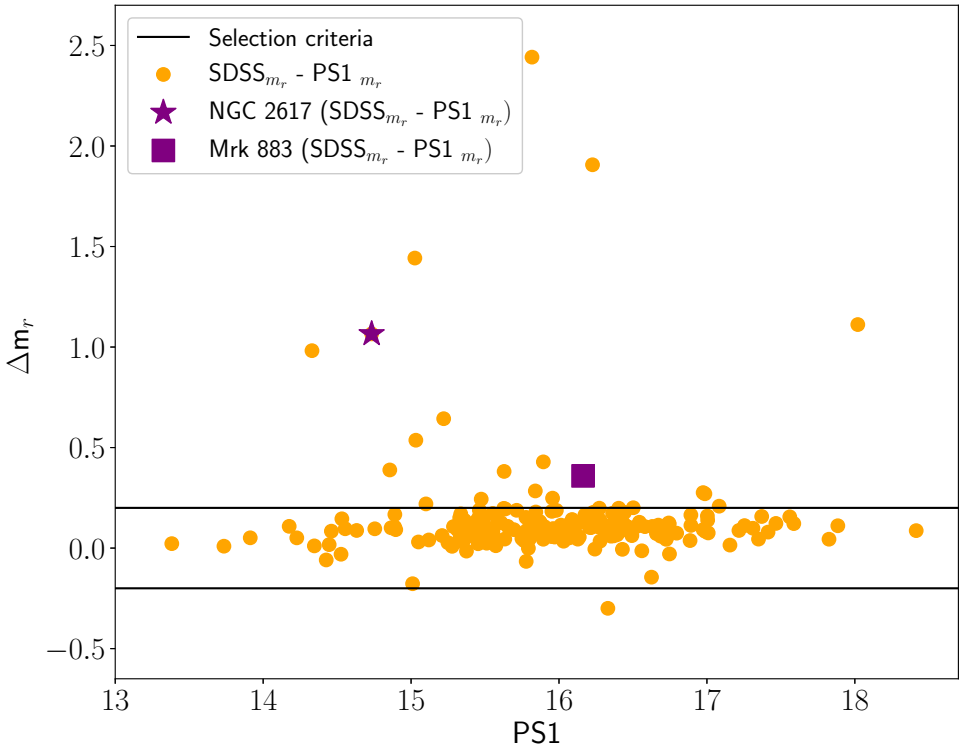

FIGURE 2.4: The r-band magnitude as a function of apparent magnitude for Véron-Cetty & Véron (2010) type 1.8s, type 1.9s and type 2s, measured with SDSS and Pan-STARRS 3″ aperture photometry. Known CLAGNs NGC 2617 and Mrk 883 are highlighted, NGC 2617 became 1 magnitude brighter in r-band between the SDSS and Pan-STARRS imaging surveys.

Most of the AGNs that display a high change are type 1 Seyferts which naturally vary over time. Variability on the timescale of months or a few years indicated some emission is occurring close to the central engine (de Ruiter & Lub, 1986; Burtscher et al., 2015), and the varying MIR emission is attributed to a dusty wind in the AGNs polar region (Hönig et al., 2013). As with the previous CLAGN candidate selection methods, we inspect the archival spectra of AGNs where 1.8s, 1.9s and type 2s had ΔW1 $>$ 0.3 mag. In all instances where we identified a type 2 with *WISE* variability and spectra more recent than 2017, we found that the recent spectra still exhibited narrow lines (i.e., NGC 4135, NGC 6230, IC 1495 and Mrk 670). Thus, we did not undertake any spectroscopic follow up of AGNs on the basis of infrared variability alone.

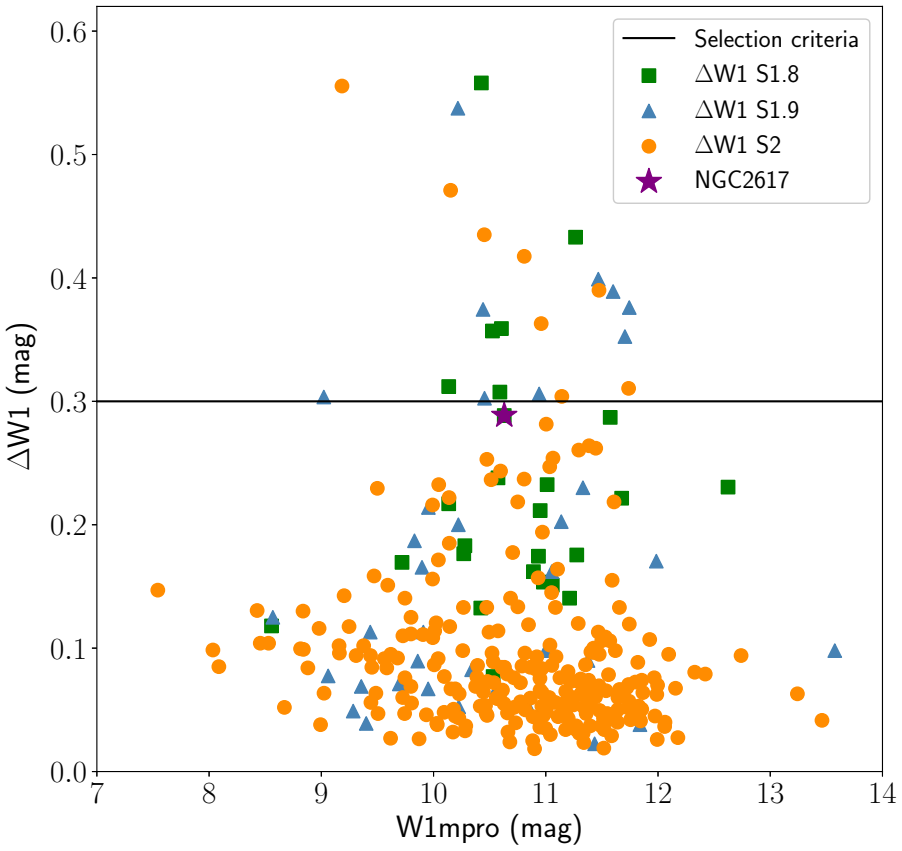

FIGURE 2.5: Change in NEOWISE W1 photometry as a function of W1 photometry. As type 1s vary at ~ 3.5 μm without changing spectral type, we can only plot and draw CLAGN candidates from AGNs classes type 1.8s, 1.9s and type 2.0s. The purple star is NGC 2617, a known CLAGN.

2.3.5 AGNs with 2 or more archival spectra

To measure the completeness of our colour and flux selection criteria we inspected AGNs that have 2 or more archival spectra. Our main sources of spectra are WiFeS Siding Spring Southern Seyfert Spectroscopic Snapshot Survey (S7; Dopita et al., 2015), SDSS, 6dFGS and Ho et al. (1995). The date ranges for these spectra sources are as follows: S7 spectra were observed from 2013-2016, SDSS spectra were observed between 2000-2019 (where DR16 spectra were observed through 2019), 6dFGS spectra were observed from 2001-2009 and Ho et al. (1995) spectra were observed between 1984-1990. Of all the z <0.04 AGNs in our sample, 21% do not have readily available spectra online and 52% have

TABLE 2.2: Sample taken from our SkyMapper catalogue used to select CLAGN candidates. Note that the full table is available online.

					SkyMapper			SDSS				Pan-STARRS[a]						
RA (deg)	Dec (deg)	Name	z	VCV Spec. Type	r (mag)	i (mag)	z (mag)	MJD	r (mag)	i (mag)	z (mag)	MJD	r (deg)	i (deg)	z (deg)	Flag[b]	Spectra Notes[c]	Spec. Sources[d]
0.8839	-10.7446	NGC7808	0.03	1	15.11	14.62	14.39	51792	15.92	15.48	15.13	55866	15.85	15.38	15.09	0	3	2,3
2.7260	-21.0675	ESO538-G25	0.03	2	15.77	15.32	14.93	53353	16.67	16.20	15.78	56028	16.56	16.08	15.78	0	2	2
2.7776	-12.1079	MARK938	0.02	2	14.48	13.95	13.69	0	0.00	0.00	0.00	56170	15.44	15.03	14.56	0	2	2
6.8176	-1.7802	NGC118	0.04	2	14.52	14.16	13.90	54769	15.29	14.90	14.65	55618	15.26	14.89	14.69	0	0	0
8.5568	-21.4386	ESO540-G01	0.03	1.8	14.61	14.32	14.08	53995	15.38	15.07	14.79	55913	15.33	15.03	14.84	2	0	0
8.9533	-13.6106	NGC166	0.02	2	15.43	15.04	14.55	0	0.00	0.00	0.00	56123	16.34	15.94	15.54	0	0	0
9.3992	0.2807	MARK955	0.04	2	15.14	14.72	14.46	52231	15.94	15.56	15.26	55541	15.87	15.43	15.22	0	2	3
10.7200	-23.5410	NGC235	0.02	1	14.50	14.04	13.66	53995	15.07	14.73	14.42	55937	14.99	14.65	14.35	0	2	5
11.0909	-17.3512	ESO540-G17	0.03	2	16.52	16.10	15.73	0	0.00	0.00	0.00	56026	17.41	16.99	16.66	0	2	2
13.3747	-8.7677	NGC291	0.02	2	15.55	14.88	14.74	51814	16.38	15.98	15.57	55768	16.32	15.96	15.59	0	3	2,3
13.7271	-32.0317	ESO411-G029	0.03	2	15.60	15.01	14.75	0	0.00	0.00	0.00	0	0.00	0.00	0.00	0	2	2
14.5930	-36.6601	ESO351-G025	0.04	2	16.20	15.77	15.45	0	0.00	0.00	0.00	0	0.00	0.00	0.00	0	2	2
16.3203	-58.4375	ESO113-G10	0.03	1.8	14.89	14.53	14.29	0	0.00	0.00	0.00	0	0.00	0.00	0.00	0	0	0
18.0802	-32.0612	NGC427	0.03	1.2	15.52	15.22	14.99	0	0.00	0.00	0.00	0	0.00	0.00	0.00	0	2	2
18.2025	-0.2902	SDSSJ01128-0017	0.02	2	14.44	13.95	13.63	52963	15.16	14.74	14.35	55635	15.11	14.65	14.42	0	2	3
18.5293	-32.6509	IC1657	0.01	2	15.39	14.68	14.55	0	0.00	0.00	0.00	0	0.00	0.00	0.00	0	3	2,4
18.7029	-0.4961	UGC793	0.03	1.5	16.09	15.59	15.30	53272	16.91	16.54	16.23	55834	16.81	16.46	16.27	0	3	3,32
18.9802	-50.1894	ESO195-G35	0.02	2	14.84	14.43	14.16	0	0.00	0.00	0.00	0	0.00	0.00	0.00	0	2	2
20.0821	-44.1287	ESO244-G17	0.02	1.5	15.47	15.13	14.84	0	0.00	0.00	0.00	0	0.00	0.00	0.00	0	0	0
20.8383	-1.9766	UM319	0.02	2	16.19	15.73	15.43	54770	17.08	16.74	16.35	55913	17.03	16.65	16.38	0	2	2
20.9766	-35.0654	NGC526A	0.02	1.9	14.93	14.42	14.00	0	0.00	0.00	0.00	0	0.00	0.00	0.00	0	3	2,5
23.4906	-36.4932	NGC612	0.03	2	15.27	14.64	14.25	0	0.00	0.00	0.00	0	0.00	0.00	0.00	0	3	2,5
25.9065	-33.7054	ESO353-G38	0.03	2	15.11	14.64	14.40	0	0.00	0.00	0.00	0	0.00	0.00	0.00	0	0	0
25.9907	2.3499	MARK573	0.02	1	14.46	14.12	13.89	54742	15.12	14.95	14.62	56011	15.03	14.88	14.57	0	2	4
27.9245	-36.1878	ESO354-G04	0.03	1	15.13	14.64	14.37	0	0.00	0.00	0.00	0	0.00	0.00	0.00	0	2	2
28.2042	-3.4468	MCG-01.05.047	0.02	2	15.94	15.43	15.10	54770	16.92	16.44	16.02	56294	17.50	16.79	16.28	0	3	2,5
29.9634	-6.8404	IC184	0.02	2	15.55	15.15	14.78	54832	16.48	16.10	15.78	56178	16.41	15.96	15.74	0	3	2,15
30.2769	-6.8159	NGC788	0.01	1	14.39	13.99	13.70	54832	15.28	14.93	14.57	56178	15.19	14.78	14.57	0	2	5
32.3525	-10.1359	NGC835	0.01	2	13.84	13.37	13.07	51813	14.68	14.25	13.93	56091	14.50	14.12	13.85	0	3	2,4
33.4098	-0.7173	SDSSJ02136-0043	0.02	1	15.21	14.87	14.71	52963	16.17	15.79	15.45	56254	16.06	15.65	15.46	0	2	3

[a] NOTE: The Pan-STARRS photometry in this table has been measured by us using the Pan-STARRS cutouts (where available) with a 3″ diameter aperture for the AGNs in our Skymapper catalogue.
[b] Optical colour selection flag where 1 indicates possible narrowing spectra and 2 indicates possible broadening spectra.
[c] CLAGN spectra flag where: 0 No archival spectra online, 1 Varying in archival and/or WiFeS spectra, 2 Only one archival spectrum found and no WiFeS, 3 Two or more archival spectra, not varying in WiFeS and archival spectra, 4 No archival spectra found from the last 10 years, but shows signs of varying before then and 5 No archival spectra found from the past 10 years, does not show signs of varying before then.
[d] If Spectra Notes is 0, then this is also 0. 1 WiFeS 2 6dFGS 3 SDSS 4 S7 5 BASS 6 2dFGRS 7 Ho et al. (1995) 8 MaNGA 9 Fosbury et al. (1982) 10 Phillips et al. (1983) 11 Kennicutt & Keel (1984) 12 Bergvall et al. (1986) 13 Veron-Cetty & Veron (1986a) 14 Veron-Cetty & Veron (1986b) 15 Kollatschny & Fricke (1987) 16 Maia et al. (1987) 17 Rudy et al. (1988) 18 Morris & Ward (1988) 19 Storchi Bergmann et al. (1990) 20 Winkler (1992) 21 de Grijp et al. (1992) 22 Moran et al. (1994) 23 Cruz-Gonzalez et al. (1994) 24 Goodrich (1995) 25 Maia et al. (1996) 26 Moran et al. (1996) 27 Reimers et al. (1996) 28 Scarpa et al. (1996) 29 Coziol et al. (1997) 30 Pietsch et al. (1998) 31 Fraquelli et al. (2000) 32 Jansen et al. (2000) 33 Kewley et al. (2001a) 34 Reunanen et al. (2003) 35 Márquez et al. (2004) 36 Georgantopoulos et al. (2004) 37 Masetti et al. (2006a) 38 Masetti et al. (2006b) 39 Moustakas & Kennicutt (2006) 40 Ho & Kim (2009) 41 Trippe et al. (2010) 42 Dopita et al. (2014) 43 Schmidt et al. (2016) 44 Ramos Almeida et al. (2016) 45 Thomas et al. (2017)

TABLE 2.3: Sample taken from our Pan-STARRS (PS1) catalogue used to select CLAGN candidates. Note that the full table is available online.

					Pan-STARRS (PS1)			SDSS						
RA (deg)	Dec (deg)	Name	z	VCV Spec. Type	r (mag)	i (mag)	z (mag)	MJD	r (mag)	i (mag)	z (mag)	Flag[a]	Spectra Notes[b]	Spec. Sources[c]
0.4933	36.6489	Zw517.014	0.032	2	16.13	15.78	15.53	0	0.00	0.00	0.00	0	0	0
0.6100	3.3517	MARK543	0.026	1.5	15.75	15.64	15.38	54742	15.76	15.58	15.31	0	0	0
0.7900	21.9600	MARK334	0.022	1.8	15.51	15.27	14.89	54849	15.54	15.27	14.86	0	0	0
0.8837	-10.7447	NGC7808	0.029	1	15.86	15.38	15.10	51792	15.92	15.48	15.13	1	3	2,3
1.5813	20.2031	MARK335	0.026	1	14.35	14.45	14.21	55119	14.43	14.90	14.45	0	2	5
2.7262	-21.0675	ESO538-G25	0.026	2	16.54	16.07	15.77	53353	16.67	16.20	15.78	0	2	2
2.7775	-12.1075	MARK938	0.019	2	15.23	14.80	14.32	0	0.00	0.00	0.00	0	2	2
4.5979	30.0631	NGC71	0.022	2	15.95	15.48	15.18	55122	16.02	15.59	15.21	0	0	0
6.8175	-1.7797	NGC118	0.037	2	15.28	14.90	14.71	54769	15.29	14.90	14.65	0	0	0
8.5575	-21.4389	ESO540-G01	0.027	1.8	15.33	15.03	14.84	53995	15.38	15.07	14.79	0	0	0
8.9533	-13.6103	NGC166	0.020	2	16.33	15.94	15.54	0	0.00	0.00	0.00	0	0	0
9.3992	0.2808	MARK955	0.035	2	15.89	15.47	15.25	52231	15.94	15.56	15.26	0	2	3
9.7392	48.3372	NGC185	0.000	2	17.34	16.99	16.76	0	0.00	0.00	0.00	0	2	7
10.6846	41.2694	M31	0.000	2	12.52	100.00	12.21	0	0.00	0.00	0.00	2	3	7,39,50
10.7200	-23.5411	NGC235	0.022	1	15.00	14.67	14.37	53995	15.07	14.73	14.42	0	2	5
11.0908	-17.3517	ESO540-G17	0.031	2	17.34	16.94	16.62	0	0.00	0.00	0.00	0	2	2
11.8308	14.7033	MARK1146	0.039	1	16.77	16.25	15.95	51878	16.51	16.12	15.82	1	2	3
12.1967	31.9569	MARK348	0.014	1	15.63	15.36	15.08	55121	15.78	15.52	15.13	0	2	5
12.8958	29.4011	UGC524	0.036	1	15.77	15.18	14.94	55122	15.75	15.36	15.05	1	0	0
13.3742	-8.7678	NGC291	0.019	2	16.31	15.95	15.60	51814	16.38	15.98	15.57	0	3	2,3
13.7608	-19.0047	ESO541-G001	0.021	2	16.20	15.83	15.57	0	0.00	0.00	0.00	0	0	0
14.9171	15.3308	UGC615	0.018	2	15.63	15.19	14.90	51464	15.68	15.20	14.94	0	2	3
14.9721	31.8269	MARK352	0.015	1	15.87	15.47	15.52	55121	15.76	15.69	15.48	0	2	5
17.1983	-15.8425	IC78	0.040	2	16.04	15.57	15.12	0	0.00	0.00	0.00	0	0	0
18.2025	-0.2900	SDSSJ01128-0017	0.018	2	15.12	14.66	14.43	52963	15.16	14.74	14.35	0	2	3
18.7025	-0.4958	UGC793	0.034	1.5	16.83	16.48	16.28	53272	16.91	16.54	16.23	0	2	3
19.0300	33.0894	MARK1	0.016	2	15.92	15.95	15.78	0	0.00	0.00	0.00	2	2	41
20.8383	-1.9767	UM319	0.016	2	17.01	16.63	16.37	54770	17.08	16.74	16.35	0	2	2
21.1117	33.7994	NGC513	0.019	1	15.61	15.16	14.85	53263	15.71	15.26	14.85	1	2	5
21.3808	32.1364	MARK993	0.017	1.5	15.50	15.10	14.81	53263	15.63	15.21	14.82	0	0	0

[a] Optical colour selection flag where 1 indicates possible narrowing spectra and 2 indicates possible broadening spectra.

[b] CLAGN spectra flag where: 0 No archival spectra online, 1 Varying in archival and/or WiFeS spectra, 2 Only one archival spectrum found and no WiFeS, 3 Two or more archival spectra, not varying in WiFeS and archival spectra, 4 No archival spectra found from the last 10 years, but shows signs of varying before then and 5 No archival spectra found from the past 10 years, does not show signs of varying before then.

[c] If Spectra Notes is 0, then this is also 0. 1 WiFeS 2 6dFGS 3 SDSS 4 S7 5 BASS 6 2dFGRS 7 Ho et al. (1995) 8 MaNGA 9 MUSE 10 Phillips et al. (1983) 11 Goodrich & Osterbrock (1983) 12 Penston & Perez (1984) 13 Osterbrock (1985) 14 Bergvall et al. (1986) 15 Veron-Cetty & Veron (1986a) 16 Rudy et al. (1988) 17 Morris & Ward (1988) 18 Sabbadin et al. (1989) 19 Gregory et al. (1991) 20 Kennicutt (1992) 21 Tran et al. (1992b) 22 de Grijp et al. (1992) 23 Durret (1994) 24 Kim et al. (1995) 25 Goodrich (1995) 26 Moran et al. (1996) 27 Owen et al. (1996) 28 Scarpa et al. (1996) 29 Coziol et al. (1997) 30 Pietsch et al. (1998) 31 Wei et al. (1999) 32 Gonçalves et al. (1999) 33 White et al. (2000) 34 2000UZC...C.....0F 35 Reichardt et al. (2001) 36 Stepanian et al. (2002) 37 Rossa et al. (2006) 38 Moustakas & Kennicutt (2006) 39 Lira et al. (2007) 40 Buttiglione et al. (2009) 41 Stoklasová et al. (2009) 42 Tsalmantza et al. (2009) 43 Trippe et al. (2010) 44 Gavazzi et al. (2013) 45 Barth et al. (2015) 46 Dopita et al. (2015) 47 Schmidt et al. (2016) 48 Ramos Almeida et al. (2016) 49 Thomas et al. (2017) 50 Greenawalt et al. (1997)

TABLE 2.4: CLAGN candidates that were observed with WiFeS between 2018 July and 2019 March.

2MASX ID	Name	redshift	Initial type	WiFeS classification	MJD
J03252538-0608380	Mrk 609	0.0345	1.9,2	1.9	58375
J03301327-0532363[a]	NGC 1346	0.0135	1.8	2	58457
J05521140-0727222	NGC 2110	0.0078	1	1	58491
J08044636+1046363	UGC 04211	0.0344	1	1	58548
J08353877-0405172[b]	NGC 2617	0.0142	1.8	1	58491
J10445172+0635488	NGC 3362	0.0277	2	2	58491
J13254405-2950012	NGC 5135	0.0137	2	2	58549
J13311382-2524096	ESO 509- G 038	0.0260	1	1	58548
J13352457+0124376	NGC 5227	0.0175	2	2	58548
J15461637+0224558	NGC 5990	0.0128	2	2	58549
J20075129-1108346[a]		0.03	2	1.8	58308
J21141259+0210406	IC 1368	0.0130	2	2	58310
J21522605-0810248		0.0348	2	2	58375
J22590139-2531423	ESO 535- G 001	0.0303	2	2	58309
J22364648-1232426	Mrk 915	0.0241	2	1.9	58724

[a] New CLAGN that we have identified
[b] Known CLAGN

only one available spectrum and 27% have multiple archival spectra. As we are refining our CLAGN candidates by selecting candidates where the archival spectra already show some signs of change, there is the potential to miss CLAGNs where the spectra have changed after the last archival spectra was taken and this will decrease our completeness. Of the AGNs that were not identified by our CLAGN candidate selection methods and have multiple archival spectra, we identified AGNs that appeared to have some small variations in the spectra, however these variations were not significant enough to require further investigation (i.e. changes in spectral class were 0.1 or less, where there are no clear signs of the appearance or disappearance of broadening in the spectra). Thus, while our three candidate selection criteria select many AGNs that are not CLAGNs, our selection criteria are not missing a large number of nearby CLAGNs.

2.4 Spectroscopic follow-up

Once candidates were identified using the colour and flux criteria discussed in Sections 2.3.2, 2.3.3 and 2.3.4, we inspected the archival spectra of these objects in order to identify potential CLAGNs without obtaining new spectra. It should be noted that we did not follow up candidates where archival spectra from the past two decades showed no variability (irrespective of the selection criteria).

We used the Wide Field Spectrograph (WiFeS, Dopita et al., 2010) Integral Field Unit (IFU) on the Australian National University's 2.3 m telescope at Siding Spring to obtain new spectra of our candidates to confirm that they are indeed CLAGN. WiFeS has a field of view of $25'' \times 38''$, divided into 950 spaxels. The advantage of using an IFU for follow-up observations of candidates is that extraction aperture size can be matched to previous observations (e.g. the $7''$ fibre of 6dF, Jones et al., 2009). The wavelength coverage is $3800 - 9200$ Å, which spans the Hα, Hβ and [OIII] lines at $z < 0.04$, and we expect Hα to show the most clear signs of change in CLAGNs.

We observed in nod-and-shuffle mode taking at least three frames with 60s on object, 60s on sky and 10 cycles per frame. This results in 40 min on object, 40 min on sky, and $\sim$ 15 min on overheads including telescope nod time, guide star re-acquisition and CCD readout. In total we allow $\sim$100 mins per galaxy. Our observations were taken between July 2018 and 2019 March. We reduced our data with PyWiFeS, Python-based pipeline (Childress et al., 2014). We observed 15 CLAGN candidates over multiple observing sessions, the AGNs are presented in Table 2.4.

2.5 Spectral variability and new CLAGNs

We next present the spectra of the new CLAGNs that we have identified using the selection criteria mentioned in Sections 2.3.2, 2.3.3 and 2.3.4, where we compare archival spectra of the galaxies with spectra taken using WiFeS. We plot archival spectra, where available, with the spectra taken using WiFeS to display the change. Multiplicative scaling has been applied so that the continuum spectra agree, highlighting changes in the emission lines. We match apertures of the multiple spectra of the new CLAGNs and AGNs with varying spectra below (where possible). It should be noted however, that the features in our observed WiFeS spectra displayed their respective broad line and narrow line features irrespective of the extraction aperture used.

2.5.1 2MASX J20075129-1108346

2MASX J20075129-1108346 was classified as a type 1.9 by Véron-Cetty & Véron (2010), however it has SkyMapper r - $i < 0.35$ mag, which according to the optical colour selection criteria we adopt in Section 2.3.2, suggests that the spectra of this AGN may have broadened. The 6dFGS spectrum in Figure 2.6 is consistent with a type 2 as the spectra contains only narrow line components. Our 2018 WiFeS spectrum shows broad line components (irrespective of the extraction aperture used, an aperture of 7″ was used for Figure 2.6) and we classify it as a type 1.8. As 2MASX J20075129-1108346 changes from type 2 to type 1.8. This change meets our criteria for a CLAGN.

2.5.2 Mrk 609

Mrk 609 is classified by Véron-Cetty & Véron (2010) as a type 1.8 using the spectra from Rudy et al. (1988), but has r - $i < 0.35$ mag in SkyMapper, indicating according to our colour selection criteria that it may have broad line components. Mrk 609 was one of the first Seyferts to be classified as an intermediate type. Mrk 609 was classified as a type 1.8 by Osterbrock (1981). Rudy et al. (1988) note that the spectral lines were inconsistent with a type 1 Seyfert, i.e. it lacks broad lines. Trippe et al. (2010) report small variability in Mrk 609 spectra. They note the absence of broad line components in their observed spectra which they classified as type 2, although prior observations of Mrk 609, including Osterbrock (1981), note broad Hα components. As the Rudy et al. (1988) spectral classification is inconclusive, we use the SDSS and 6dFGS spectra in Figure 2.7 as the baseline for determining whether Mrk 609 is changing spectral type. We classify the SDSS and 6dFGS spectra as type 1.9 and type 2, respectively, in accordance with the criteria outlined by Osterbrock (1981). Our WiFeS spectra is consistent with that of a type 1.9 and is similar to that of SDSS indicating that Mrk 609 changed spectral type between 2001 and 2018 to a type 2, and has returned to being a type 1.9. This small variation in spectra is not consistent with our CLAGN criterion, but additional spectroscopy may reveal further changes in the spectral class of Mrk 609.

2.5.3 Mrk 915

Mrk 915 was classified as a type 1.8 by Véron-Cetty & Véron (2010) using the Dahari & De Robertis (1988) spectrum, but has Pan-STARRS r - $i < 0.25$ mag. This colour, according to our Pan-STARRS colour selection criteria, suggests that the spectra of Mrk 915 has broadened. Goodrich (1995) first reported the varying spectrum of Mrk 915, with a narrowing of emission lines between 1984 to 1993. Giannuzzo & Stirpe (1996) also note a variation in the spectrum of Mrk 915, where they observed a broadening of the Hα line between 1993 and 1994. While the 1993 spectrum in Figure 2.8 is of relatively poor quality, it does not show the broad line component of subsequent spectra, and we conclude Mrk 915 as a type 2 Seyfert at the time. We classify the *BAT AGN Spectroscopic Survey* (BASS: Koss et al., 2017) spectrum as type 1.9; the 2019 WiFeS spectrum in Figure 2.8 is also consistent with a type 1.9. The Hα line is broader in the 2008 and 2010 spectrum (note: both spectra are from the same survey) and is broader still in the WiFeS 2019 spectrum. This variation in spectra from type 2 to type 1.9 does not meet our criteria for CLAGN. Although this may be the case, it is a good candidate CLAGN and further observations are needed.

2.5.4 NGC 1346

NGC 1346 is a newly discovered CLAGN. We identified NGC 1346 as a broad-line AGN with unusually red colours with the SDSS and Pan-STARRS photometry and we designated it as a CLAGN via visual inspection of spectra from SDSS, 6dFGS and S7. NGC 1346 was classified as a Seyfert 1 galaxy by Véron-Cetty & Véron (2003) using the SDSS spectra in Figure 2.9. We classify this spectrum as a type 1.8 according to the definitions outlined by Osterbrock (1981). The spectrum from SDSS (taken in 2001) showed a significant broad line component, however the 2004 December 6dFGS (Jones et al., 2009) spectrum contains only narrow emission lines. The S7 spectrum of NGC 1346 and the WiFeS 2018 spectrum showed only narrow lines. Therefore, NGC 1346 was a type 1.8 prior to 2004 and it changed spectral type between 2001 and 2004. We use infrared photometry to investigate why this AGN is changing spectral type.

To determine if a varying hot dust component of NGC 1346 could be responsible for the change in spectral type we use NEOWISE photometry and compared 2MASS photometry with recent targeted InfraRed Survey Facility (IRSF; Nagayama, 2012) photometry. The NEOWISE photometry was taken between 2014 and 2018 with a cadence of 6 months, and was thus taken after the change in spectral type. We measure a change in NEOWISE photometry of 0.11 mag; this is not a significant change and is not considered high enough to suggest a change in spectral type. This is because the NEOWISE survey has data from 2014 onward, and as suggested by the spectra, NGC 1346 had already changed spectral types by then.

We find that NGC 1346 has faded by 0.82 mag in the K_s-band between 1998 and 2018, where we measure photometry from 2MASS and IRSF, respectively. IR wavelength is sensitive to emission from warm dust attributed to the torus. We measure a change in the IR photometry, this indicates that the change in spectral type we measure may be a result of changes in the torus. That being said, we cannot rule out that nuclear continuum is not contributing to the K_s-band flux. The K_s-band will have contributions from both the torus and nuclear continuum, however the torus dominates.

2.6 Conclusions

We have conducted a systematic survey for CLAGNs by identifying candidates using optical and infrared photometry from SkyMapper, Pan-STARRS, SDSS and NEOWISE. Using SkyMapper, we select type 1s with $r - i > 0.53$ mag and type 2s with r - $i < 0.35$ mag and using Pan-STARRS we select type 1s with $r - i > 0.43$ mag and type 2s with r - $i < 0.25$ mag. We also select candidates with optical r-band flux where type 1.8s, 1.9s and type 2s had $\Delta m_r > 0.2$, and search for AGNs with variability in *WISE* W1(3.4 μm) (type 1.8s, 1.9s and type 2s where $\Delta W1 > 0.3$ mag). Identifying candidates using optical colour selection provided the largest number of plausible candidates, with our new CLAGNs being selected in this manner. While this is the case, this selection criteria also produced the largest number of contaminants. The optical flux variability

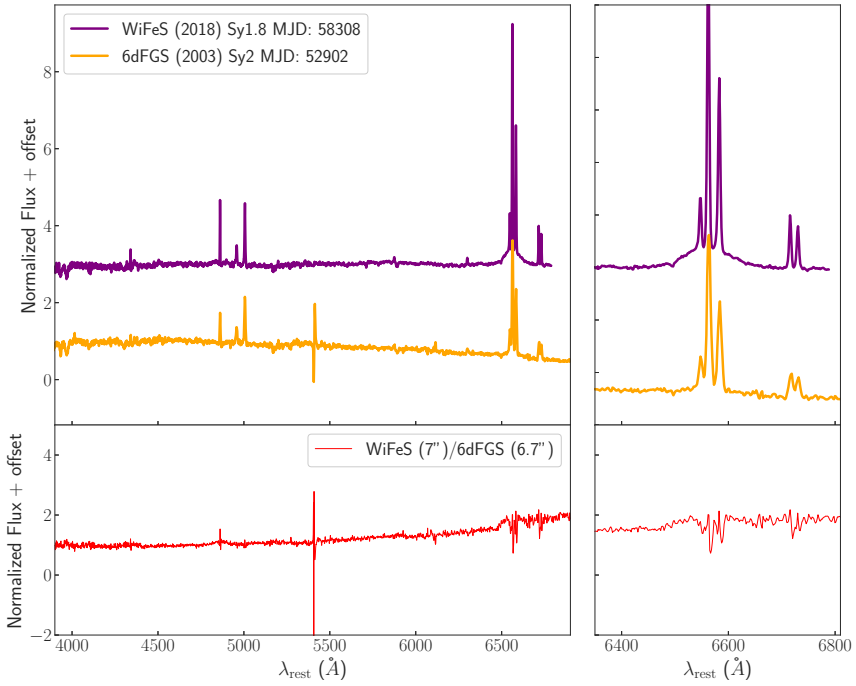

FIGURE 2.6: 2MASX J20075129-1108346 is a new CLAGN which was a type 2 in the 6dFGS spectrum observed in 2003, and was determined to be a broad type 1.8 in the WiFeS spectrum taken in 2018. These classifications were made in accordance to the descriptions in Osterbrock (1981).

selection did not identify any new candidates, however it identified NGC 2617 as a candidate, showing it is a plausible method to identify CLAGNs.

Using NEOWISE W1 (3.4 μm) photometry we find majority of type 1s and type 2s have exhibited > 0.3 mag and < 0.3 mag, respectively, of variability during 2014 - 2018. While this allowed us to select type 2s displaying variability of > 0.3 mag as CLAGN candidates, in practice all of the candidates selected appear to be (on the basis of archival spectra) misclassified broad line AGN. Thus *WISE* W1 variability didn't prove useful for identifying changing-look Seyferts, but it could work with cleaner input catalogues and it has been used to identify changing-look quasars (e.g., Guo et al., 2016; Ross et al., 2018; Stern et al., 2018).

Using our optical colour selection method we were able to identify four AGNs with varying spectra. 2MASX J20075129-110834 and NGC 1346 are new CLAGNs that were identified in this work using optical colour selection. Mrk 915 and Mrk

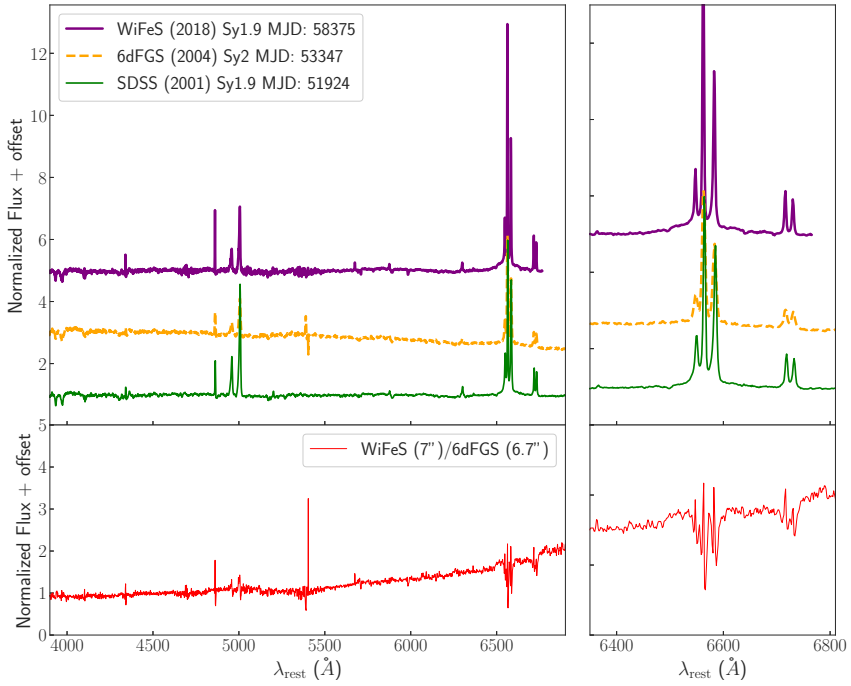

FIGURE 2.7: Mrk 609 has varying spectra and was identified using optical colour selection. The SDSS spectrum is consistent with a type 1.9 where the 6dFGS spectrum is completely narrow indicating it is a type 2. We classify Mrk 609 as type 1.9 using our WiFeS spectrum, and thus the changes in spectral class are insufficient to meet our CLAGN criterion.

609 have varying spectra which do not meet our criteria for CLAGN and only have a small change from type 2 to type 1.9 and type 1.9 to type 2, respectively. These AGNs remain CLAGN candidates and additional followup spectroscopy may reveal further changes in their spectral types. 46% of candidates selected using this method either didn't have archival spectra at all, didn't have archival spectra from the last 10 years or only had one archival spectrum. Extrapolating this, we can estimate that we have only identified 54% of possible CLAGNs in this sample due to lack of spectra. The optical colour selection method also only identifies $\approx$ 50 % of known CLAGN.

We note that as we refined our CLAGN candidates by selecting candidates where the archival spectra already showed signs of change, we may have missed CLAGNs that may have changed after the last archival spectra was taken and/or changed type relatively briefly (i.e. $<$ 2 years). To estimate the number of

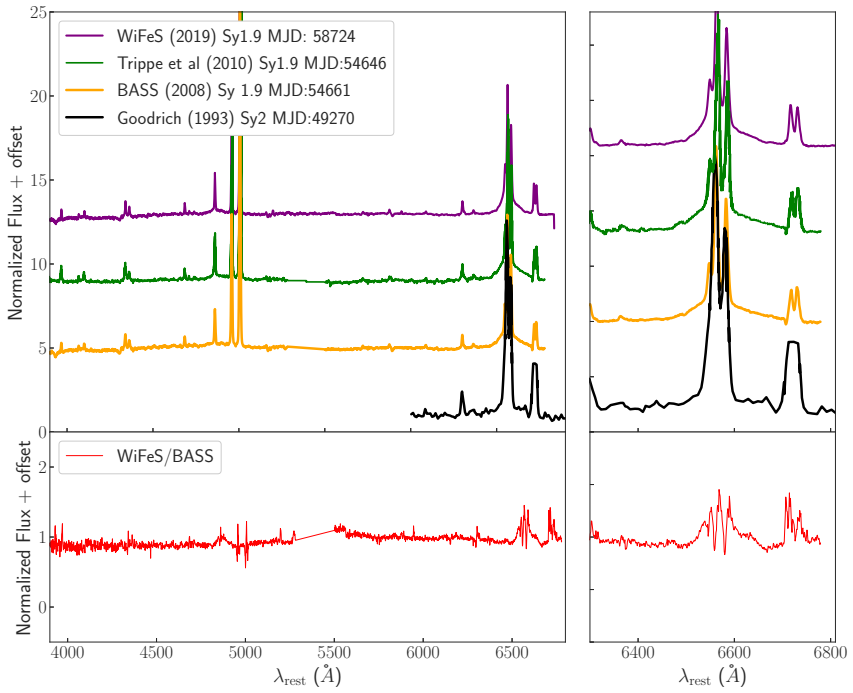

FIGURE 2.8: Mrk 915 is a varying AGN that was identified using optical colour selection. We classify the 1993 (Goodrich, 1995) spectrum as a type 2 as it contains only narrow lines and the BASS 2008 spectrum is consistent with a type 1.9. The WiFeS 2019 spectra is that of an type 1.9 . However, this change from type 2 to type 1.9 is not significant enough to meet out CLAGN criteria. Although this is the case, it is a good CLAGN candidate that will require further investigation.

CLAGN candidates that could have changed spectral type rapidly or briefly, we need an estimate of the numbers of CLAGNs as a function of the timescale of variability. 1ES 1927+654 (z = 0.017) is a CLAGN that changed from type 2 to type 1, where the change lasted for 11 months (Trakhtenbrot et al., 2019). For our candidates selected via optical and infrared flux changes the variability is on timescales of a decade to 6 months respectively. Optical flux variability will miss CLAGNs that vary only briefly from their usual state, and while NEOWISE has the cadence to detect such candidates the NEOWISE variability of 1ES 1927+654 remained < 0.2 mag (although the TDE produced ~ 2 mags brightening in the optical) and thus it wasn't flagged as a *WISE* selected CLAGN candidate. We also note that clouds of dust moving across the line of

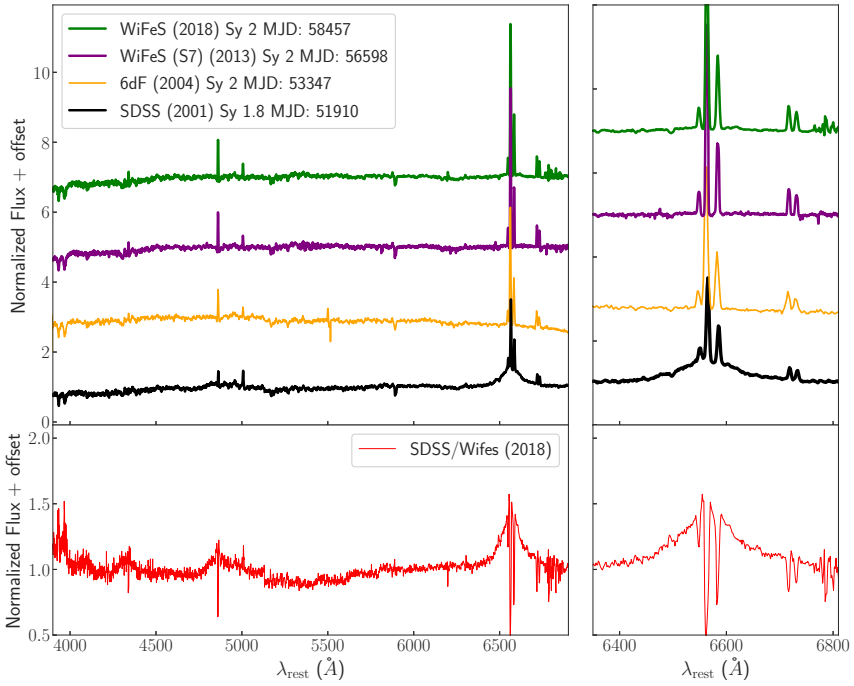

FIGURE 2.9: Spectra of CLAGN NGC 1346, with the SDSS spectrum revealing broad Hα consistent with a type 1.8, while subsequent archival 6dFGS and WiFeS spectra, and our new WiFeS spectra, indicate a Seyfert 2 (Senarath et al., 2019).

sight may not significantly impact the NEOWISE photometry as this can occur on relatively short time scales (Guo et al., 2016), thus this subclass of CLAGN could be underrepresented in our sample. As such we have a lower limit of $\approx$ 18 CLAGN as $z < 0.04$, which includes 2 new CLAGNS discovered in this work, 10 previously known CLAGNs that have varied between 1998 and 2015, and as many as 6 CLAGNs that missed our candidate selection methods or didn't have archival spectra.

Chapter 3

AGN Bolometric Corrections

3.1 Introduction

The bolometric luminosities of individual AGNs and the luminosity functions of AGN populations provides a measure of the accretion rate of individual supermassive black holes (SMBH) and the accretion history of SMBHs (e.g. Barger et al., 2001; Gitti et al., 2012; Mocz et al., 2013). The bolometric luminosity of an object measures the total energy per second emitted over all wavelengths in all directions. Theoretical models of AGN feedback make predictions that are based on bolometric luminosity that require bolometric corrections and are measured using bolometric quasar luminosity functions (e.g. Richards et al., 2006a; Shen et al., 2020; Florez et al., 2021; Yung et al., 2021).

Bolometric luminosities are measured by integrating over the entire AGN SED. The shape of an AGN SED depends on the physical properties and structure of the AGN. These are the accretion disk, central black hole, dusty torus, emission from radio structures that may be present and heated dust in the host galaxy (heated by AGN and star formation) (e.g. Padovani et al., 2017, and references therein). Different wavelengths trace different regions in the AGN and this is illustrated in Figure 1.10. The IR emisson results from warm dust often attributed to the torus, the UV/optical probes emission from the accretion disk and fast moving gas (1000 - 10,000 km sec^{-1}) in the BLR (and is often obscured

by dust), and the X-ray traces emission on the hot corona and ionized reflection (e.g. Padovani et al., 2017, and references therein).

We require SEDs that span a broad wavelength range to measure bolometric luminosities. To create an SED that covers a wide wavelength range requires observations from multiple telescopes and the data collected must be homogenised. The leading composite AGN SEDs are based on many bright quasars, where Richards et al. (2006b) uses photometry from thousands of AGNs to produce composite SEDs, while Brown et al. (2019) uses spectroscopy and photometry of dozens of AGNs to produce SEDs of individual AGNs. However, it is important to observe more AGNs to make these SEDs more accurate and to observe a variety of different AGN types. The best available AGN SEDs of individual AGNs are currently Brown et al. (2019), which span from at least 0.09 to 30 μm and often include X-ray and radio, covering bolometric luminosities of $\mathrm{Log}(L_{bol}) \approx$ 42.5 - 47.5 erg s^{-1}. We go into more detail on the Brown et al. (2019) SEDs in Section 3.2.

The integration range used by the literature to measure bolometric corrections varies, and is often limited to the wavelength range the SEDs cover. Studies such as Nemmen & Brotherton (2010), Runnoe et al. (2012a), Runnoe et al. (2012b) and Krawczyk et al. (2013) integrate over a shorter wavelength range that excludes the IR (1 μm - 8 keV). Their reasoning for not including the IR is that the IR may be reprocessed light from UV and optical photons which could cause double counting of photons. Also, some SEDs did not contain spectra that extended to the IR. Richards et al. (2006b) and Elvis et al. (1994) however, integrate over a much wider wavelength range including the IR and beyond. The specific integration ranges used by these studies are shown in Table 3.1. The IR wavelengths are unaffected by dust obscuration and the shape of the IR spectrum can vary for each AGN, particularly between obscured and unobscured AGNs. The risk of double counting is lower for obscured AGNs than it is unobscured AGNs. The consequence not including the IR, in particular for unobscured AGNs is that there is a lot of activity in the IR, which will lead to underestimating the bolometric luminosity. This chapter will consider how different selections impact

TABLE 3.1: Wavelength range archival bolometric corrections integrate over to measure bolometric luminosities.

Study Name	Number of SEDs	Bolometric luminosity λ range
Elvis et al. (1994)	47	100 μm - 10 keV
Richards et al. (2006b)	259	100 μm - 10 keV
Nemmen & Brotherton (2010)		10^{14} - 10^{17} Hz (3 μm - 0.5 keV)
Runnoe et al. (2012a)	63	1 μm - 8 keV
Runnoe et al. (2012b)	63	1 μm - 8 keV
Krawczyk et al. (2013)	119,652	1 μm - 2 keV
Pennell et al. (2017)	63	1 μm - 8 keV
Duras et al. (2020)	991	type 1: 20 Å- 1 μm, type 2: 1 μm - 1000 μm
This work	27	24 μm - 8 keV

bolometric corrections and our sample of AGN SEDs. Therefore, we include the IR in our measurements of bolometric luminosity.

Studies of bolometric corrections, such as Richards et al. (2006b), Shang et al. (2011) Runnoe et al. (2012a) and Runnoe et al. (2012b) tend to favour luminous and unobscured AGNs. The bolometric corrections of these studies are thus representative of AGNs with higher luminosity. In particular, Richards et al. (2006b) measure bolometric corrections for 259 luminous type 1 (unobscured), using the IR to select their type 1 quasar sample. They measure bolometric corrections for both individual SEDs and a mean SED, finding that the mean SED can be in error by ≈ 50 % for individual type 1 quasars and that this error translates directly to the presumed accretion rate. This is also the approach used by Elvis et al. (1994), who was perhaps the first to use a mean SED to measure bolometric corrections in the UV, visible and IR. The errors observed by Richards et al. (2006b) mean SEDs may be poor matches to some AGNs.

Motivated by this, in this chapter we use the Brown et al. (2019) AGN SEDs to measure IR, UV/ optical and X-ray bolometric corrections at 1.5 μm, 2 μm, 3 μm, 7 μm, 12 μm, 15 μm, 24 μm, 1450 Å, 3000 Å, 5100 Å and 2 - 10 keV. We use the IR wavelengths in particular as these wavelengths allow for our bolometric corrections to be used for objects that have been observed with *WISE* (Wright et al., 2010), *Spitzer* (Werner et al., 2004) or will be observed by the James Webb Space telescope (JWST; Bouchet et al., 2015) with a range of redshifts. These wavelengths allow for direct comparison between our bolometric corrections and those within the literature. This means that we are able to fully characterise the bolometric corrections at these wavelengths and discuss how using different samples may impact measurements of bolometric corrections.

In Section 3.2 we introduce the Brown et al. (2019) AGN SED sample, in Section 3.3 we explain how we measure the bolometric corrections using our sample and in Sections 3.4, 3.5 and 3.6 we discuss the measured bolometric corrections and what can impact these measurements, including fitting method, contributions from the host galaxy light, and sample selection.

3.2 The SED Sample

We use the AGN SED templates from Brown et al. (2019) to calculate IR bolometric corrections as these are the best available SEDs of individual AGNs at this time. These AGNs span a wide range of luminosities and AGN types including obscured, unobscured and BL Lacs. Most of these SEDs span at least 0.09 to 30 μm, while many (27 AGNs) have wavelength coverage beyond this into the X-ray. Brown et al. (2019) have combined spectroscopic data from multiple sources to create the AGN SEDs and the sample spans a redshift range of $z \approx$ 0.01 - 0.37.

To construct their SEDs, Brown et al. (2019) use ground-based optical and near-IR spectroscopy including from Shang et al. (2005), Riffel et al. (2006), Landt et al. (2008) and Landt et al. (2013). At other wavelengths Brown et al. (2019) use spectroscopic data from the Nuclear Spectroscopic Telescope Array (NuSTAR), *Suzaku*, the Far Ultraviolet Spectroscopic Explorer (FUSE), *XMM-Newton*, the *Chandra* X-ray observatory, the International Ultraviolet Explorer (*IUE*), the Hopkins Ultraviolet Telescope (HUT), the Galaxy Evolution Explorer (GALEX), *Hubble Space Telescope* (*HST*), *Spitzer*, *Akari*, the Infrared Space Observatory (*ISO*), the Wisconsin Ultraviolet Photo-Polarimeter Experiment (WUPPE), and *Herschel*. Of the 41 SEDs in the Brown et al. (2019) sample, only 27 have SEDs that extend to the X-ray wavelengths, and thus these 27 SEDs make up the core sample used to measure our bolometric corrections.

To produce continuous SEDs using the archival data mentioned above, Brown et al. (2019) multiplicatively scale the necessary spectra so that they will agree with photometry and to produce continuous SEDs. These scalings were between 0.33 and 3.0. Some SEDs have gaps between archival spectra, which are filled

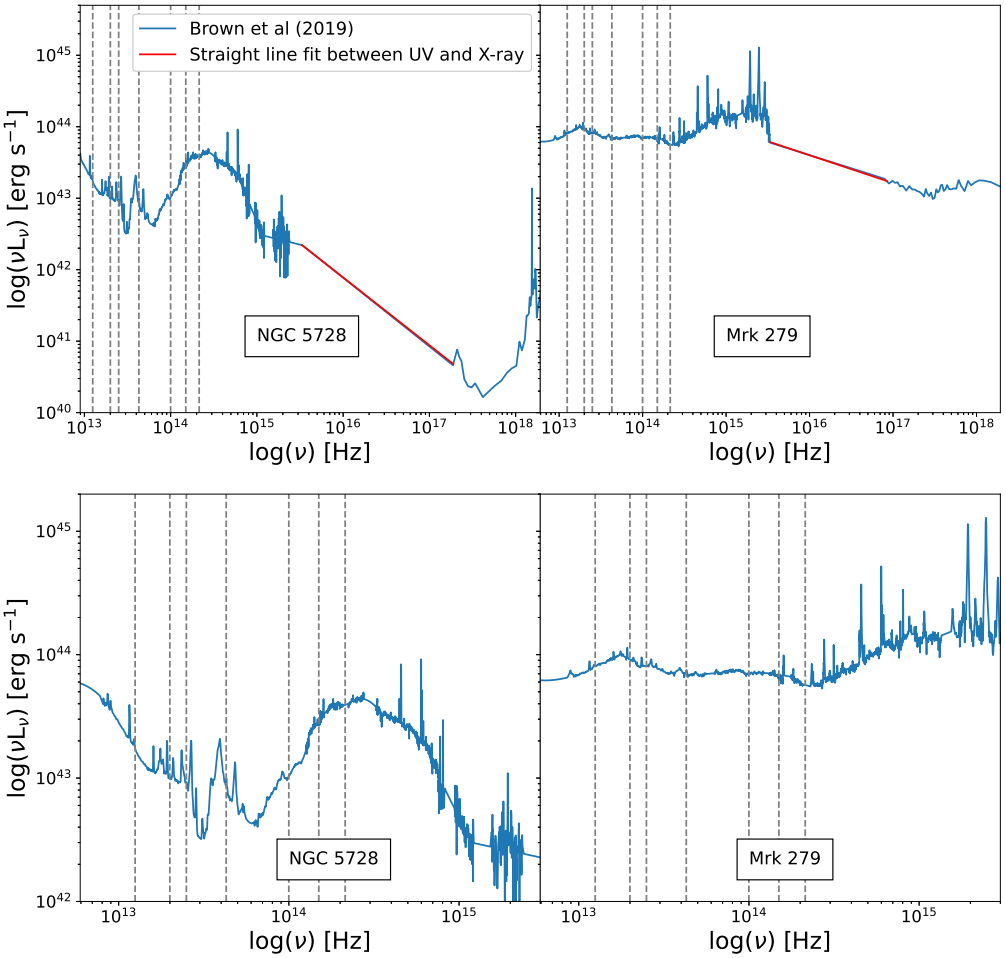

FIGURE 3.1: SEDs of NGC 5728 (left) and Mrk 279 (right) from Brown et al. (2019). The vertical dashed lines represent the IR wavelengths at which we measure our bolometric corrections, these are 1.5 µm, 2 µm, 3 µm, 7 µm, 12 µm, 15 µm and 24 µm. PAHs can clearly be seen in the IR in NGC 5728 (left) and thus this AGN and four other AGNs with visible PAHs have been removed when calculating the bolometric corrections for our 'AGNs with no PAH' sample and our 'no host contamination' sample. We also display zoomed in panels of the UV, optical and IR for the two AGNs to show more detail.

using simple models (often polynomials or power-laws) which interpolate or extrapolate from the spectra available. When multiple archival spectra cover the same wavelength range for the same AGN, Brown et al. (2019) combine the spectra together to attain higher signal-to-noise. We present examples of Brown et al. (2019) SEDs in Figure 3.1, where we can see that the wavelength coverage of these SEDs is from the IR to the X-ray.

3.3 Calculating Bolometric Luminosity.

We use the methods outlined by Hogg et al. (2002) (and used by Runnoe et al., 2012a) to calculate bolometric luminosities for our AGN sample. The measured observed flux can be converted to observed luminosity using:

$$L_{obs,\nu_{obs}} = \int_0^{2\pi} \int_0^{\pi} F_{obs,\nu_{obs}} d_L^2 \sin\theta \ \mathrm{d}\theta \ \mathrm{d}\phi \tag{3.1}$$

if the source is isotropic, then this becomes the following;

$$L_{obs,\nu_{obs}} = 4\pi d_L^2 F_{obs,\nu_{obs}} \tag{3.2}$$

where $\mathrm{F}_{obs,\nu_{obs}}$ is the observed flux density, d_L is the luminosity distance, and ν_{obs} is the observed frequency. The integration from Equations 3.1 to 3.2 becomes 4π. The observed luminosity is then converted to rest luminosity using:

$$L_{rest,\nu_{rest}} = \frac{L_{obs,\nu_{obs}}}{1+z} = \frac{4\pi d_L^2 F_{obs,\nu_{obs}}}{1+z} \tag{3.3}$$

where ν_{rest} is the rest frequency (Hogg et al., 2002). Integrating $\mathrm{L}_{rest,\nu_{rest}}$ over frequency will give the bolometric luminosity (L_{bol}).

The Brown et al. (2019) AGN SEDs have spectra that span from the X-ray to the IR. To measure bolometric luminosities we integrate from 24 µm to 8 keV ($\nu = 1.25 \times 10^{13} - 1.93 \times 10^{18}$ Hz), where we integrate over the IR and to the X-ray. This integration range is wider than studies such as Nemmen & Brotherton (2010), Runnoe et al. (2012a), Runnoe et al. (2012b) and Krawczyk et al. (2013). Runnoe et al. (2012a) and Runnoe et al. (2012b) use a sample of bright mostly unobscured AGNs and integrate over 1 µm to 8 keV. Richards et al. (2006b) measure bolometric corrections for a sample of unobscured quasars and integrate over a larger range (100 µm - 10 keV). We list the specific integration used by quasar studies in Table 3.1.

The data coverage between the FUV and X-ray ($\nu \sim 3\times\ 10^{15}$ - $1\ \times\ 10^{17}$) is not present in the Brown et al. (2019) SEDs. It should be noted that all SEDs contain this deficit, i.e. there is data missing between the FUV to X-ray, thus calculations of AGN bolometric luminosities must extrapolate between the FUV and X-ray. The use of different models for this has been explored by Runnoe et al. (2012a), including the Mathews & Ferland (1987) model and the Korista et al. (1997) model, however, Runnoe et al. (2012a) ultimately chose a straight line fit between FUV to X-ray in log space. The reason for this is that they found that Mathews & Ferland (1987) and Korista et al. (1997) models were not good descriptions of the SEDs in many cases. In some objects the X-ray data was either overestimated or underestimated, by as much as a order of magnitude, for over an order of magnitude in frequency.

For simplicity, we use the same approach used by Runnoe et al. (2012a) and Runnoe et al. (2012b) and use a straight line fit between the FUV to X-ray data and interpolate between this region of the SEDs when calculating the bolometric luminosities. NGC 5278 (left panel of Figure 3.1) is an example of an AGN SED in our sample, the red line in the figure displays the frequency range that we interpolated over.

We determined the exact frequency boundaries for the FUV to X-ray by visual inspection, making sure not to include the Lyα absorption. While the choice of exact frequencies does affect the bolometric luminosity we calculate, the effect is only $\log(L_{bol})\ \approx 0.10$ dex and thus ultimately has very little affect on the bolometric luminosity calculated. It should be noted that there are many sources of uncertainty when measuring bolometric luminosities. These include how we deal with the gap between FUV to X-ray, interpolation of the SED, host galaxy corrections (which we go into more detail about in Section 3.4.3) and orientation of the AGN, which is generally unknown (Nemmen & Brotherton, 2010; Runnoe et al., 2012a).

We present our IR bolometric luminosity (L_{bol}) and our monochromatic luminosity (λL_λ) measurements in Table 3.2 for λ = 1.5 µm, 2 µm, 3 µm, 7 µm, 12 µm, 15 µm and 24 µm. PG0052+251, 3C 351 and PG2349-014 appear in both our sample and that of Runnoe et al. (2012b). To compare with Runnoe

et al. (2012a) we calculated test luminosities over the integration range used by Runnoe et al. (2012a) (1 μm - 8 keV) and find the Log(L_{bol}) measurement for these three AGNs differ by -0.07, +0.01 and +0.07, respectively, between us and Runnoe et al. (2012b). This is very encouraging, and these minor differences are likely caused by differences in the Shang et al. (2011) and Brown et al. (2019) SEDs used.

TABLE 3.2: Our bolometric luminosities ($\log(L_{bol})$) and IR monochromatic luminosities ($\log(\lambda L_{\lambda})$). Note all are in units of erg s^{-1}.

Object	$\log(L_{bol})$	$\log(\lambda L_{\lambda}1.5\mu m)$	$\log(\lambda L_{\lambda}2\mu m)$	$\log(\lambda L_{\lambda}3\mu m)$	$\log(\lambda L_{\lambda}7\mu m)$	$\log(\lambda L_{\lambda}12\mu m)$	$\log(\lambda L_{\lambda}15\mu m)$	$\log(\lambda L_{\lambda}\ 24\mu m)$	$\log(L_{bol:1\mu m-8keV})$
3C120	45.48	44.04	44.20	44.29	44.21	44.29	44.31	44.32	45.39
3C273	47.04	45.78	45.89	45.98	45.83	45.76	45.75	45.71	46.94
3C351	46.72	45.70	45.83	45.93	45.69	45.77	45.80	45.89	46.51
3C390-3	45.28	44.13	44.26	44.30	44.25	44.32	44.36	44.33	45.11
Ark120	45.26	44.28	44.39	44.41	44.24	44.16	44.10	43.97	45.09
Fairall9	45.47	44.38	44.58	44.63	44.56	44.55	44.56	44.43	45.26
Mrk110	44.94	43.64	43.73	43.78	43.68	43.65	43.65	43.41	44.86
Mrk231	45.72	44.74	44.98	45.06	45.22	45.26	45.44	45.62	44.56
Mrk279	44.88	43.75	43.81	43.85	43.87	43.91	43.96	43.91	44.72
Mrk290	44.48	43.46	43.53	43.55	43.54	43.62	43.67	43.62	44.26
Mrk421	45.66	44.16	44.07	43.96	43.73	43.57	43.53	43.39	45.64
Mrk509	45.37	44.24	44.34	44.39	44.34	44.37	44.42	44.41	45.20
Mrk590	44.27	43.80	43.72	43.42	43.26	43.51	43.62	43.63	43.84
Mrk817	45.02	43.96	44.08	44.11	44.10	44.25	44.33	44.51	44.76
Mrk876	46.00	44.86	44.99	45.06	45.03	45.04	45.01	45.03	45.82
Mrk926	45.26	44.29	44.45	44.48	44.22	44.12	44.15	44.14	45.07
NGC3227-central	43.12	42.33	42.33	42.22	42.52	42.52	42.66	42.79	42.61
NGC3516-central	43.90	43.09	43.07	43.07	43.10	43.11	43.16	43.21	43.58
NGC4051-central	42.72	41.80	41.89	41.91	42.03	42.17	42.19	42.25	42.28
NGC4151-central	43.69	42.57	42.69	42.81	42.85	42.95	43.05	42.99	43.41
NGC5548-central	44.21	43.34	43.41	43.37	43.40	43.56	43.63	43.68	43.82
NGC5728	43.94	43.59	43.44	43.02	42.99	42.97	43.00	43.24	43.52
NGC7469	44.73	43.76	43.82	43.79	44.01	44.07	44.16	44.44	44.34
PG0026+129	46.06	44.58	44.76	44.83	44.64	44.58	44.53	44.30	45.99
PG0052+251	45.98	44.69	44.81	44.90	44.78	44.81	44.83	44.60	45.87
PG2349-014	45.99	44.86	45.01	45.10	44.89	44.90	44.86	44.90	45.84
PKS-1345+12	45.47	44.54	44.47	44.53	44.79	45.13	45.27	45.46	44.50

Quasar emission is anisotropic, and this varies from object to object and is also dependent on the wavelength in question. When measuring bolometric luminosities, they are measured under the assumption of isotropy. For unobscured quasars, one can directly observe photons from near the central black hole and one can also observe IR photons from hot dust, which is heated by UV/optical photons that originally were not travelling towards the observer. Thus including the IR in bolometric luminosities for quasars could result in "double counting" and overestimates of bolometric luminosities. Studies such as Nemmen & Brotherton (2010), Runnoe et al. (2012a), Runnoe et al. (2012b) and Krawczyk et al. (2013) measure bolometric corrections using wavelength ranges that exclude the IR. The reason for this is that they assume that some IR photons could result from double counting. It should also be noted that another reason for them not including IR is that lack of wavelength coverage in some AGN SEDs. In order to investigate this further we measured bolometric luminosities for the same wavelength as Runnoe et al. (2012a) of 1 μm - 8 keV and these are provided in Table 3.2.

For blue quasars the differences between bolometric luminosities calculated with and without IR are within 0.20 dex, while for more obscured AGNs larger differences are seen (which make sense given most photons travelling directly towards the observer are absorbed by dust). Given we want bolometric corrections that apply to as broad a range of AGN classes as possible, we include the IR in our bolometric luminosities. We have also provided bolometric luminosities measured using a wavelength range of 1 μm - 8 keV (in Table 3.2) so that the reader is able to utilise them to measure bolometric corrections if they choose to.

3.4 Bolometric corrections

3.4.1 Calculating Bolometric correction

Typically bolometric corrections are determined in the form:

$$L_{bol} = \zeta \lambda L_{\lambda} \tag{3.4}$$

where λL_λ is the monochromatic luminosity and the bolometric correction is ζ. This form of the bolometric correction assumes a linear relationship between the bolometric and monochromatic luminosities. The SED shape can vary with luminosity, so λL_λ may not be directly proportional to L_{bol} thus the assumption that the relationship has an intercept of zero is imprecise. For this reason we calculate our bolometric corrections in the form used by Nemmen & Brotherton (2010):

$$\log(L_{bol}) = A + B\log(\lambda L_\lambda) \tag{3.5}$$

where we fit a linear relationship between the bolometric luminosity and the monochromatic luminosity in log-space with A and B varying freely. As displayed in Table 3.7 the intercepts of the luminosities are in fact not zero.

3.4.2 Effects of different fitting techniques

We use the Hyper-fit function from Robotham & Obreschkow (2015), which uses a maximum likelihood technique, to measure our bolometric corrections. Hyper-fit fits data points in D-dimensions; (D-1)-dimensional plane (fitting points in 2 dimensions by a line). They assume that the data presented represents a random sample of a population with intrinsic Gaussian scatter, which can be described by a (D-1) dimensional plane. The objective of Hyper-fit is to determine the most likely generative model, which is done by simultaneously fitting for the (D-1)-dimensional plane and the intrinsic Gaussian scatter. It is assumed that the data has multivariate Gaussian uncertainties. That is, given that the uncertainties are different and independent for each data point and that the uncertainties are not covariant between orthogonal directions. We display a schematic of the Hyper-fit model in Figure 3.2 from Robotham & Obreschkow (2015).

We compare our bolometric corrections to that of Runnoe et al. (2012a) who use a minimising χ^2-statistics which utilises the Levenberg-Markwardt least-squared method (Markwardt, 2009). Minimised χ^2 fitting provides a reasonable approximation when one has Gaussian scatter in the y and no scatter in the x.

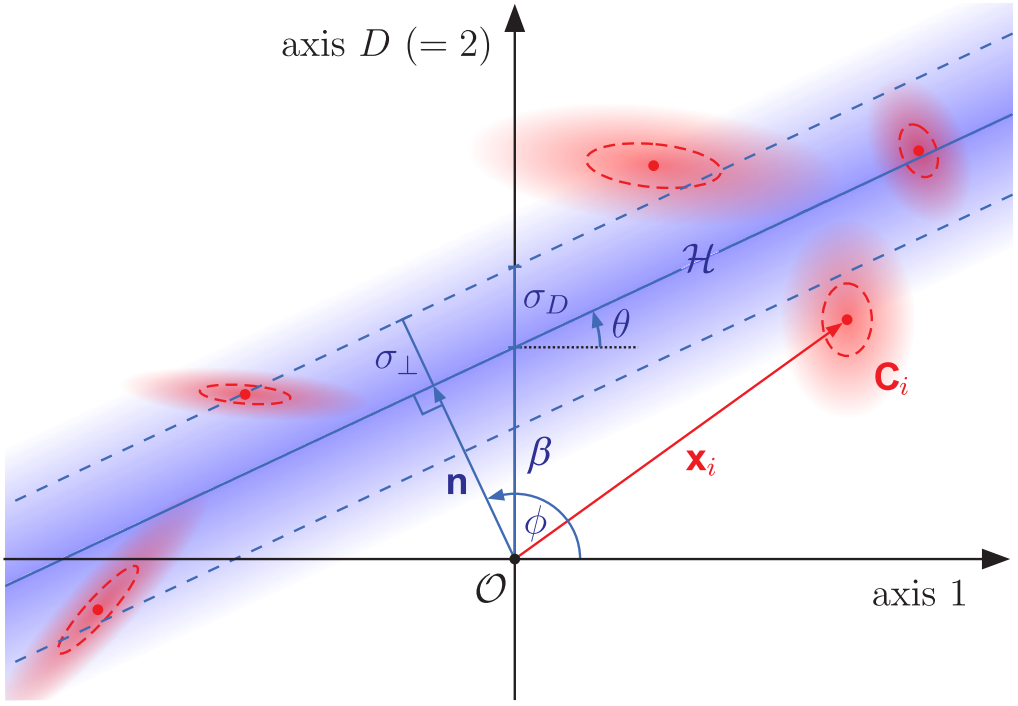

FIGURE 3.2: Schematic of the Hyper-fit linear model. Hyper-fit is a maximum likelihood technique. Gaussian distributions are assumed for both the model and the data, representing intrinsic model scatter (Robotham & Obreschkow, 2015).

However as this assumption does not apply to our data, we use Hyper-fit. The difference in the two different fitting techniques results in different overall fits to the data. For consistency, we refit the Runnoe et al. (2012a) and Runnoe et al. (2012b) luminosities with Hyper-fit and we present the results of this later in the chapter.

3.4.3 Effects of Host galaxy light

AGN emission can be significantly contaminated by the host galaxy particularly in the NIR and optical. Thus it is important to remove host galaxy light from AGNs where there is a large host galaxy contribution. In the near-infrared (NIR) we see a drop in the quasar emission and a peak in the host galaxy emission (Cardelli et al., 1989), where the host galaxy light contamination is not large for AGNs that are UV/optically bright. The H-band can be used to determine the fraction of host galaxy contamination and Shang et al. (2011) determine this by using observations of their AGNs (either archival or obtained by Shang et al.

TABLE 3.3: H-band host galaxy fractions of AGNs in our sample.

Object	H-band fraction	Source
3C273	0.13	Shang et al. (2011)
3C351	0.22	Shang et al. (2011)
Mrk290	0.11	Shang et al. (2011)
Mrk509	0.22	Shang et al. (2011)
Mrk876	0.58	McLeod & Rieke (1994b)
PG0026+129	0.22	McLeod & Rieke (1994a)
PG0052+251	0.22	Shang et al. (2011)
PG2349-014	0.65	Shang et al. (2011)

(2011) themselves) and calculating small aperture photometry of the central region of the AGN and comparing it to SDSS magnitudes, where they assume SDSS magnitudes as the total magnitude of the AGN.

Shang et al. (2011) use the elliptical galaxy template of NGC 584 from Dale et al. (2007) to remove effects of host galaxy light. They use the fraction of host galaxy light in the H-band to determine the amount of host galaxy light to subtract using NGC 584. We present an example of this in Figure 3.3 from Runnoe et al. (2012a), where the host galaxy light is subtracted from 4C 19.44 from the NIR to the UV. At Optical-FUV wavelengths, SEDs can also suffer from Galactic extinction (Milky Way) from dust.

Runnoe et al. (2012a) use the sample of AGNs from Shang et al. (2011) for their bolometric correction measurements. Shang et al. (2011) obtain H-band fraction from McLeod & Rieke (1994a) and McLeod & Rieke (1994b) and conduct their own observations, with the Infrared Telescope Facility (IRTF) or HST, when archival data is unavailable. To determine the host fraction in the H-band McLeod & Rieke (1994a) use a standard star observed directly before or after the target object. The point spread function (PSF) of the star was then scaled to the innermost pixel of the one-dimensional surface brightness profile (quasar plus host) of the target object. Using this they measured the fraction of stellar PSF needed to make the brightness profile of the quasar minus the PSF in the center and this fraction is then subtracted from the target object profile (quasar plus host), the result of this is the estimate of the host emission. For IRTF observations, Shang et al. (2011) use the same procedure as McLeod & Rieke (1994a) to measure H-band fractions.

Our sample of AGNs are located at $z < 0.37$. Of the 27 AGNs in our sample, we have archival H-band host galaxy light fractions from McLeod & Rieke (1994a) and McLeod & Rieke (1994b) for 8 AGNs and these are provided in Table 3.3. The H-band fractions for these AGNs range between 0.11 - 0.65, with a median H-band fraction of 0.22. PG 2349-014 and Mrk 876 have the largest host galaxy contribution of 0.65 and 0.58, respectively. These AGNs have bolometric luminosities ($\log(L_{bol})$) of 45.99 erg s^{-1} and 46.00 erg s^{-1} for PG 2349-014 and Mrk 876, respectively, which lies in the middle of our bolometric luminosity range.

While it is recommended to measure the H-band host galaxy contamination fraction, as discussed by Runnoe et al. (2012a), this will require us to observe the remaining 19 objects that did not have archival H-band host galaxy fractions e.g, using the HST and have left this as an avenue for important future work. In order to reduce the effects of host galaxy light in our bolometric corrections, we remove PG 2349-014 and Mrk 876, which had the highest host galaxy contribution, from our sample of 'AGNs with little or no host galaxy'.

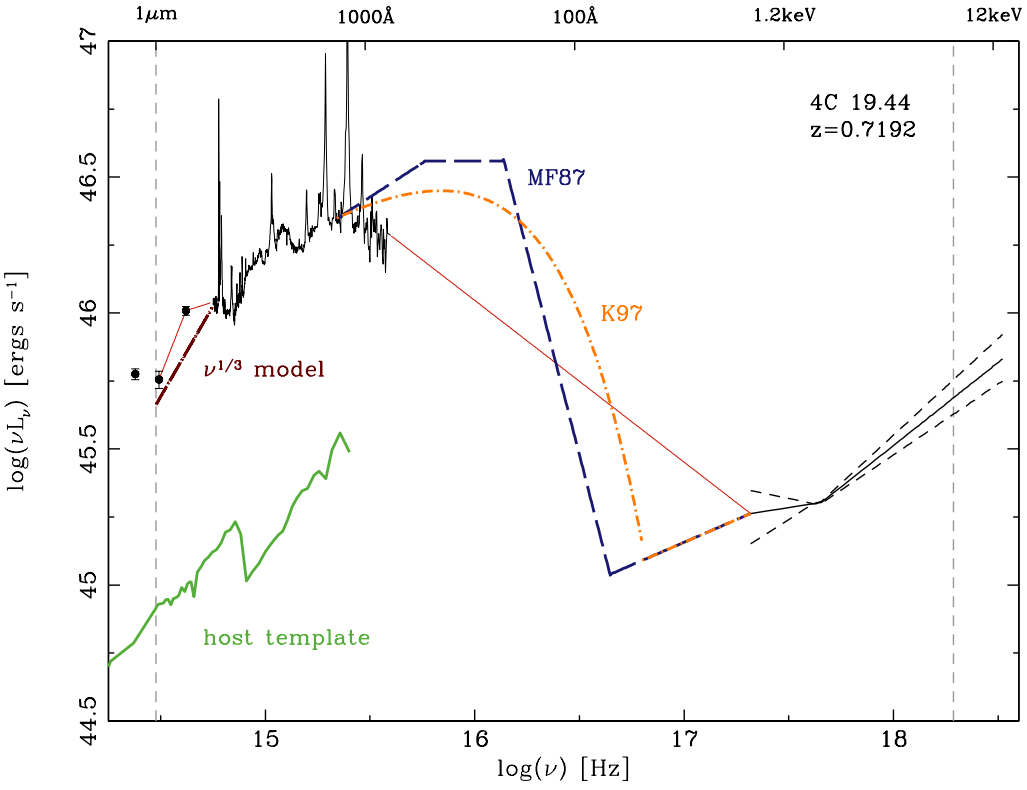

FIGURE 3.3: 4C 19.44 SED (Shang et al., 2011) NIR to X-ray region of SED, which is displayed by the solid black line from Runnoe et al. (2012a). The solid green line is the elliptical galaxy template of NGC 584 from Dale et al. (2007).

TABLE 3.4: Our bolometric luminosities ($\log(L_{bol})$) and IR monochromatic luminosities ($\log(\lambda L_\lambda)$) after subtracting NGC 584 host galaxy template. Note all are in units of erg s^{-1}.

Object	$\log(L_{bol})$	$\log(\lambda L_\lambda$ 1.5μm)	$\log(\lambda L_\lambda$ 2μm)	$\log(\lambda L_\lambda$ 3μm)	$\log(\lambda L_\lambda$ 7μm)	$\log(\lambda L_\lambda$ 12μm)	$\log(\lambda L_\lambda$ 15μm)	$\log(\lambda L_\lambda$ 24μm)
3C273	47.04	45.78	45.89	45.98	45.83	45.76	45.75	45.71
3C351	46.72	45.69	45.83	45.93	45.69	45.77	45.80	45.89
Mrk290	44.45	43.24	43.41	43.51	43.54	43.62	43.67	43.62
Mrk509	45.36	44.18	44.30	44.38	44.34	44.37	44.42	44.41
Mrk876	46.00	44.82	44.97	45.05	45.037	45.04	45.01	45.03
pg0026+129	46.06	44.56	44.75	44.82	44.64	44.58	44.53	44.30
PG0052+251	45.98	44.67	44.80	44.90	44.78	44.81	44.83	44.60
PG2349-014	45.99	44.81	44.99	45.09	44.88	44.90	44.86	44.90

Using the same approach as Shang et al. (2011), we removed host galaxy light from the AGNs in our sample that do have archival H-band fractions using the template of NGC 584 from Brown et al. (2014). We present the bolometric luminosities as well as the IR monochromatic luminosities of AGNs with host galaxy removed in Table 3.4. The differences in bolometric luminosities between AGNs with the host galaxy removed and without is only seen in Mrk 290 and Mrk 509, with decreases in luminosity of 0.03 and 0.01 dex, respectively. The other 6 AGNs had differences < 0.01 dex in the bolometric luminosity, and the reason for this is that host galaxy dominates in the H-band (peaking at 1.64 μm), however is low in other parts of the spectrum that we integrate over, and therefore we do not measure significant differences in the bolometric luminosity.

The decrease in monochromatic luminosities from the AGNs with host light and those with it removed can clearly be seen at 1.5μm, 2μm and 3μm. The decrease in monochromatic luminosity ($\log(\lambda L_\lambda)$) for longer IR wavelengths is < 0.01 dex, this is because the peak of the H-band is at 1.64 μm. The range in monochromatic luminosity decrease at 1.5μm is from 0.01 - 0.22 dex, at 2 μm there is a decrease of 0.00 - 0.12 dex and at 3 μm it is between 0.00 - 0.04 dex. We see similar results in the optical/UV, where we measure a decrease in the monochromatic luminosity at 5100 Å by 0.00 - 0.17 dex. We do not measure any changes in monochromatic luminosity at any other IR or optical/UV wavelengths.

When HST host galaxy imaging is unavailable, on obvious option is to explore SED AGN and host galaxy decomposition. Pacifici et al. (in prep., private communication) performed an analysis on various SED fitting techniques, focusing on the uncertainties that can be caused by different modelling choices and priors used. They used 5 different different codes that can include AGNs to measure the AGN fraction as a function of H-band magnitude of AGNs in the CANDELS (Grogin et al., 2011; Koekemoer et al., 2011) photometric catalogue. Overall they find that when used to interpret the same dataset, the codes provided significantly different results, in particular when the host galaxy fraction was greater than 20%. They find that the reason for this is that the codes are highly dependent on priors and the library of models that the code employs. It should also be noted that the AGN models used can also be unconstrained.

Therefore doing measurements of galaxy decomposition on individual SEDs can produce varying results.

3.4.4 PAHs

IR spectra are complex and can include emission from the host galaxy and the AGN, as well as features attributed to polycyclic aromatic hydrocarbons (PAHs), silicate absorption and the blue end of the black body spectrum of warm dust (Leger & Puget, 1984). Emission from PAHs, which are located in photo-disassociation regions, appear in the immediate surroundings of star forming regions (Wen et al., 2014) and strong PAH peaks are seen in wavelengths of 5 to 9 μm (Roussel et al., 2001). Photo-disassociation regions are regions of dense, warm gas which resides at the boundary between HII regions and molecular clouds. In star forming galaxies, emission lines attributed to PAHs are significant contributors to the overall emission. An example of an AGN with PAHs in our sample is NGC 5728 and is displayed in Figure 3.1 (left).

For this reason we characterise the bolometric correction for a number of subsets of the original 27 AGNs in addition to measuring bolometric corrections for the full sample. We measure bolometric corrections for AGNs without PAHs as well as a subset where the AGNs have no visible PAHs and H-band host galaxy fraction < 0.20 (where available). To identify AGNs with PAHs, we systematically inspect the spectra and check for PAH features at the relevant wavelengths. Of our 27 AGNs, 22 have no visible PAHs, and only 16 have both no PAHs and little or no host galaxy contamination. We discuss the differences in bolometric corrections for these samples later in the chapter.

To determine if AGNs in our sample have any significant contributions from host galaxy light, we also constructed a *WISE* colour-colour diagram. This is displayed in Figure 3.4, where we use the Jarrett et al. (2011) AGN criterion for the *WISE* colours. The hot dust from the dusty torus causes the colour of AGNs to go up; this is a good selection for AGNs because star forming galaxies do not typically have colours that reach as high as the AGN box. When W1 and W2 are dominated by host galaxy light, they typically measure the Rayleigh-Jeans tail

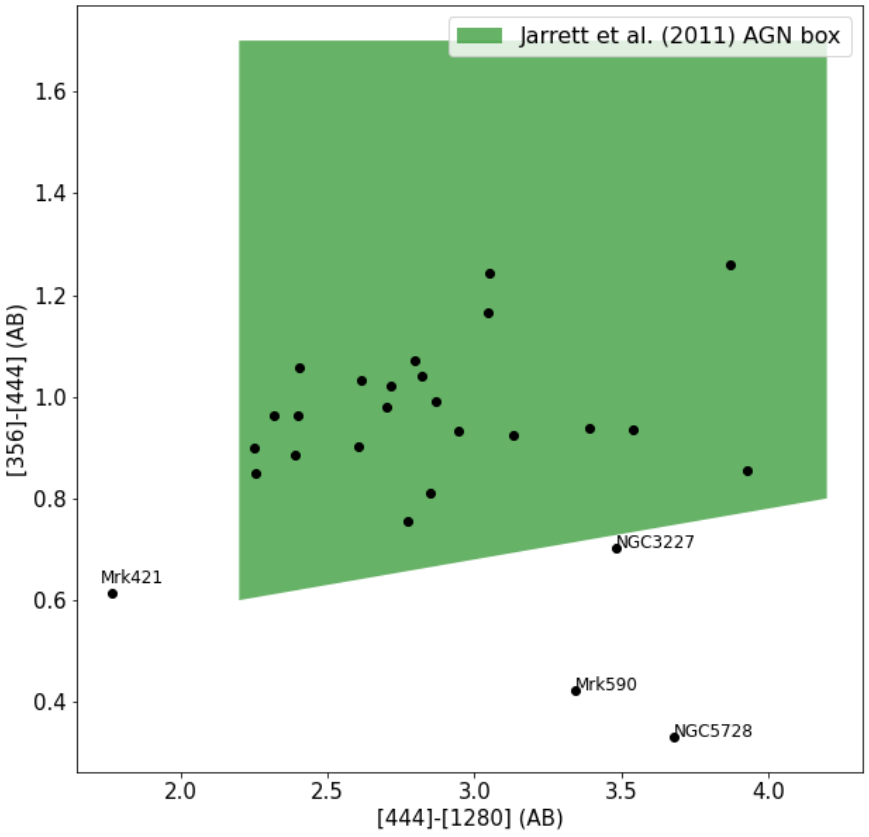

FIGURE 3.4: Colour-colour diagram of the 27 Brown et al. (2019) AGN SEDs using *WISE* colours (Jarrett et al., 2011). NGC 5728 and NGC 3227 have contributions from PAHs in their SED and have been removed from the aforementioned samples.

of the stellar population. All but four of the AGNs appear in the Jarrett et al. (2011) AGN box. Star forming galaxies occupy -0.2 < W1 - W2 (mag) < 0.5. The colours of the four AGNs outside the box (NGC 3227, Mrk 421, Mrk 590 and NGC 5728) are high and are approaching the criterion for AGN, indicating that they are AGN with some contribution from the host galaxy. This being the case, however, the contribution from the host galaxy for these AGNs is not significant enough to remove them from the sample on the basis of this alone. We note that NGC 5728 and NGC 3227 have contributions from PAHs in their SED and have been removed from the aforementioned samples.

TABLE 3.5: Our optical and UV bolometric corrections with non zero intercept in the form $\log(L_{bol}) = A + B\log(\lambda L_\lambda)$ measured using Hyper-fit.

λ (Å)	Bolometric Correction	Source	1σ vertical scatter
1450	$(12.79 \pm 2.92) + (0.73 \pm 0.07)\log(\lambda L_\lambda)$	This work, all AGNs	0.44
	$(13.52 \pm 4.54) + (0.72 \pm 0.10)\log(\lambda L_\lambda)$	This work, AGNs with no PAH	0.47
	$(4.74 \pm 1.00) + (0.91 \pm 0.02)\log(\lambda L_\lambda)$	Runnoe et al. (2012a), minimising-χ^2 fitting	
	$(4.06 \pm 1.00) + (0.92 \pm 0.02)\log(\lambda L_\lambda)$	Runnoe et al. (2012a), Hyper-fit	0.11
3000	$(4.72 \pm 2.40) + (0.92 \pm 0.05)\log(\lambda L_\lambda)$	This work, all AGNs	0.30
	$(5.49 \pm 3.67) + (0.90 \pm 0.08)\log(\lambda L_\lambda)$	This work, AGNs with no PAH	0.33
	$(1.85 \pm 1.27) + (0.98 \pm 0.03)\log(\lambda L_\lambda)$	Runnoe et al. (2012a), minimising-χ^2 fitting	
	$(0.75 \pm 1.28) + (1.00 \pm 0.03)\log(\lambda L_\lambda)$	Runnoe et al. (2012a), Hyper-fit	0.13
5100	$(-1.11 \pm 1.51) + (1.05 \pm 0.03)\log(\lambda L_\lambda)$	This work, all AGNs	0.17
	$(0.35 \pm 1.97) + (1.02 \pm 0.04)\log(\lambda L_\lambda)$	This work, AGNs with no PAH	0.16
	$(4.89 \pm 1.66) + (0.91 \pm 0.04)\log(\lambda L_\lambda)$	Runnoe et al. (2012a), minimising-χ^2 fitting	
	$(3.01 \pm 1.69) + (0.95 \pm 0.04)\log(\lambda L_\lambda)$	Runnoe et al. (2012a), Hyper-fit	0.17

3.4.5 UV/optical Bolometric corrections

In Figure 3.5 and Table 3.5 we present our bolometric corrections for $\lambda = 1450$ Å, 3000 Å and 5100 Å. The Brown et al. (2019) AGNs cover a wide luminosity range $\log(L_{bol}) = 42.5$ - 47.5 erg s^{-1}. The SEDs used by Runnoe et al. (2012a) cover a $\log(L_{bol}) = 45$ - 47.5 erg s^{-1} and the sample from Nemmen & Brotherton (2010) cover a $\log(L_{bol}) = 44.5$ - 48.5 erg s^{-1}. The broader luminosity range of our work should allow us to better constrain the model fit for the bolometric corrections better than some of the literature.

To determine if sample selection is impacting our bolometric corrections we measure corrections for a sample of SEDs with no PAHs, in addition to the full 27 AGN SED sample. We find that the gradients of the bolometric corrections for AGNs without PAHs is shallower by 0.01 - 0.03 in comparison to the bolometric corrections for the whole 27 AGN sample. The gradients of our bolometric corrections for 3000 Å and 5100 Å differ from Runnoe et al. (2012a) bolometric corrections refitted using Hyper-fit, by 0.08 and 0.10. We see the most variation in the 1450 Å bolometric correction, with a difference in gradients of 0.19 between our bolometric correction and the remeasured Runnoe et al. (2012a) slope. This variation is reflected in the high 1σ scatter of 0.44 dex in 1450 Å compared to the 0.30 dex and 0.17 dex of 3000 Å and 5100 Å, respectively. This is caused by the diversity of SEDs for our objects at 1450 Å. Our bolometric corrections appear to agree with those of Runnoe et al. (2012a) at higher luminosities. This is to be expected because Runnoe et al. (2012a) AGNs occupy brighter luminosities whereas our AGNs cover a wider luminosity range (as stated above). Our bolometric corrections appear to agree better with that of Runnoe et al. (2012a) than Nemmen & Brotherton (2010), which have gradients of 0.87, 0.81 and 0.76 for 1450 Å, 3000 Å and 5100 Å, respectively.

3.4.6 X-ray bolometric corrections

In this section we present our hard X-ray bolometric corrections (2 keV- 10keV). In order to compare our X-ray bolometric corrections to the literature we measure $\kappa_{Bol} = \mathrm{L}_{bol}/\mathrm{L}_X$, where L_X is the hard X-ray luminosity, and then plot this as a

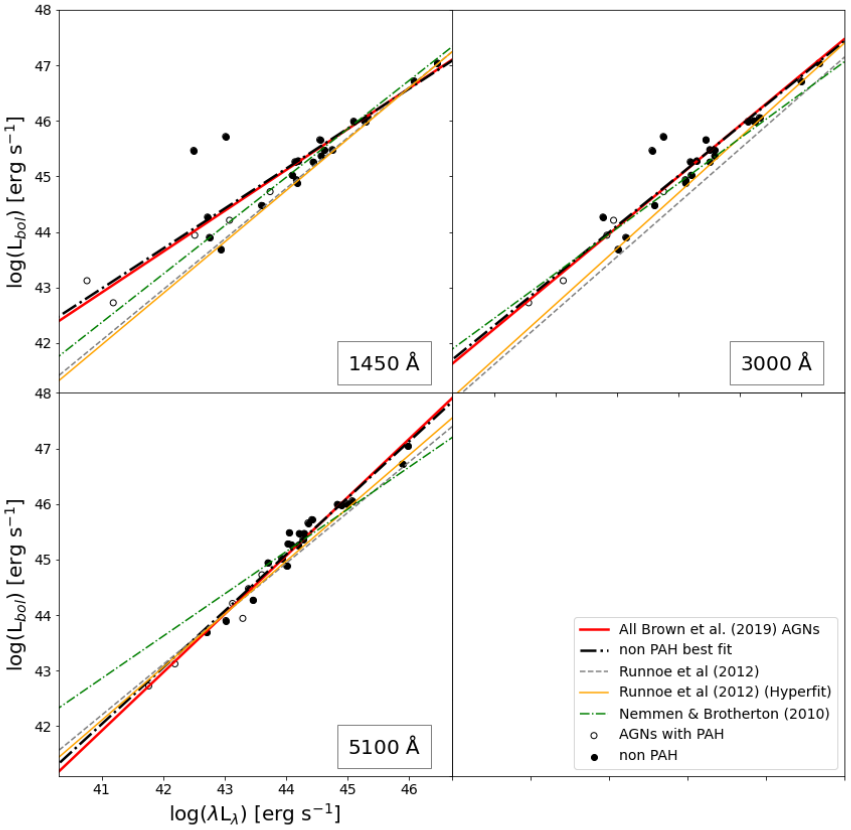

FIGURE 3.5: UV/Optical bolometric corrections for the Brown et al. (2019) SEDs. We compare our bolometric corrections to the Runnoe et al. (2012a) and Nemmen & Brotherton (2010) bolometric corrections. The Nemmen & Brotherton (2010) bolometric corrections have gradients of 0.87, 0.81 and 0.76 for 1450 Å, 3000 Å and 5100 Å, respectively. Our bolometric corrections seem agree better with that of Runnoe et al. (2012a).

function of the bolometric luminosities of our sample. We find Mrk 231, Mrk 421 and NGC 5728 (Tanimoto et al., 2018), three Compton thick AGN, are major outliers in our X-ray bolometric correction (Mrk 231 and Mrk 421 were also outliers in our IR bolometric corrections) and for this reason we exclude them when measuring the X-ray bolometric correction for all samples; including the non-PAH sample, as well as the sample with no host galaxy contributions.

We find that our X-ray bolometric corrections have κ_{Bol} measurements that are representative of the literature, in particular Marconi et al. (2004) as is evident

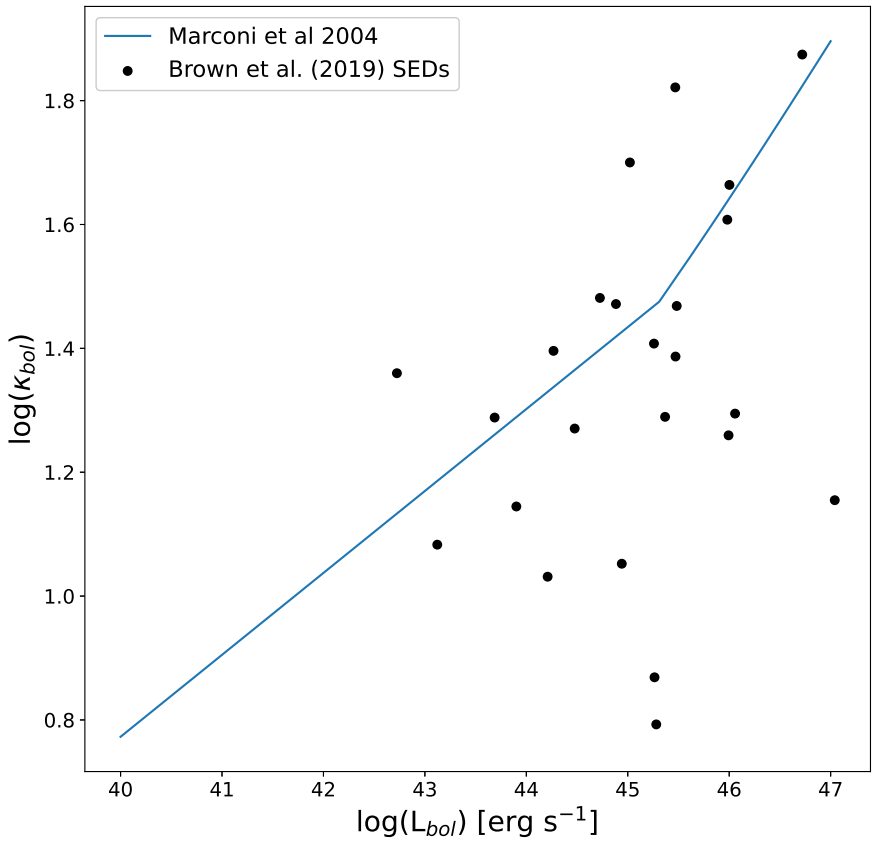

FIGURE 3.6: X-ray luminosity function measured using $\log(\kappa_{bol})$ measured for an energy range pf 2 - 10 keV as a function of $\log(L_{bol})$. We use this plot to compare our bolometric luminosities to that of Marconi et al. (2004), and find reasonable agreement with the median absolute deviation in $\log(\kappa_{bol})$ of 0.24 dex.

from Figure 3.6. Our κ_{bol} have median absolute deviation in $\log(\kappa_{bol})$ of 0.24 dex. We measure κ_{bol} to be approximately 40, which is comparable to Barger et al. (2001) and Márquez et al. (2004).

Our X-ray bolometric corrections are presented in Figure 3.7 and Table 3.6. We find that our $\log(L_{2-10\ \mathrm{keV}})$ cover a wide luminosity range of $\approx$ 41.5 - 46 erg s^{-1} and have scatter of 0.47 dex for the full AGN SED sample (minus Mrk 231, Mrk 421 and NGC 5728). It should be noted that the bolometric corrections depend little on the AGN subsample used, in part because host galaxy light is negligible in the X-ray.

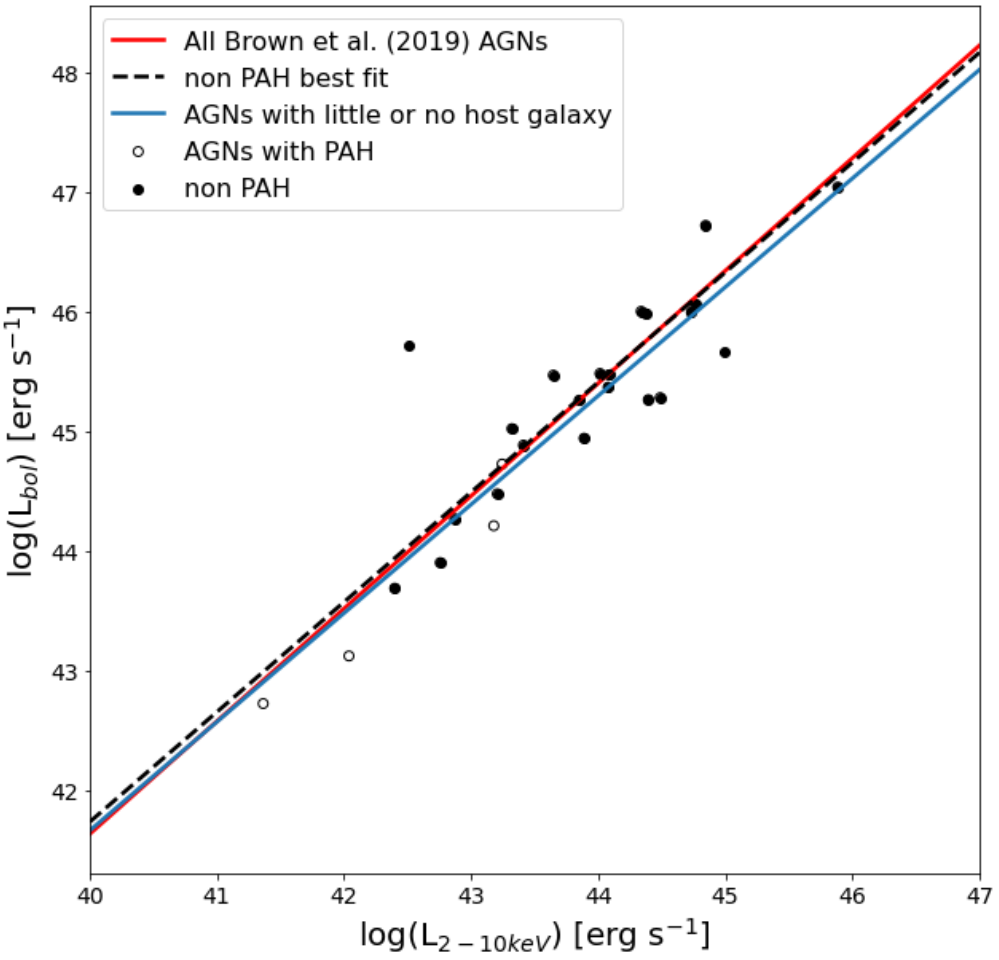

FIGURE 3.7: Hard X-ray bolometric corrections.

TABLE 3.6: Our X-ray bolometric corrections with non zero intercept in the form $\log(L_{bol}) = A + B\log(\lambda L_\lambda)$ measured using Hyper-fit.

Bolometric Correction	Source	1σ vertical scatter
$(3.99 \pm 3.94) + (0.94 \pm 0.09)\log(\lambda L_\lambda)$	This work, all AGNs	0.47
$(5.00 \pm 5.63) + (0.92 \pm 0.13)\log(\lambda L_\lambda)$	This work, AGNs with no PAH	0.47
$(5.34 \pm 3.79) + (0.91 \pm 0.09)\log(\lambda L_\lambda)$	This work, no host contamination	0.25

3.5 IR Bolometric corrections

We present our IR bolometric corrections in Table 3.2 for λ = 1.5 µm, 2 µm, 3 µm, 7 µm, 12 µm, 15 µm and 24 µm. We measure bolometric corrections for these wavelengths as they allow for our bolometric corrections to be used for objects that have been observed with *WISE* (Wright et al., 2010), *Spitzer* (Werner et al., 2004) or the JWST (Bouchet et al., 2015) with a range of redshifts. These also allow for direct comparison of our corrections with those from the literature, such as from Runnoe et al. (2012b), and references therein. Our AGN sample

covers bolometric luminosities between $\log(L_{bol}) \approx 42.5$ - 47.5 erg s^{-1}, covering a wide luminosity range.

We present the Runnoe et al. (2012b) IR bolometric corrections determined using Hyper-fit in Table 3.7. The difference in gradients of the bolometric corrections using the different fitting methods is 0.06 - 0.24 where this difference increases with increasing wavelength. The Runnoe et al. (2012a) bolometric corrections measured using Hyper-fit have gradients that are much closer to the gradients of our bolometric corrections, where the gradients measured using minimising-χ^2 are between 0.69 - 0.98, and measured using Hyper-fit these are between 0.89 - 1.07. This result shows that the choice of fitting function plays a significant role in the bolometric correction itself. The longer wavelength bolometric corrections have a steeper gradient than those measured using minimising-χ^2. It should be noted that when we compare our fits to Runnoe et al. (2012b), we are referring to the bolometric corrected remeasured using Hyper-fit.

The Runnoe et al. (2012a) SEDs cover a $\log(L_{bol}) \approx 45.5$ - 47.5 erg s^{-1}, whereas our SED sample spans this luminosity range as well as lower luminosities with $\log(L_{bol}) \approx 42.5$ - 47.5 erg s^{-1}. The Runnoe et al. (2012a) corrections agree for the higher luminosity AGNs, particularly where our luminosity range overlaps theirs. The scatter across the different bolometric corrections comes from the variability of the spectra from object to object at specific wavelengths. We see the largest amount of scatter in the 24 μm bolometric correction of 0.51 dex and this is also seen by Runnoe et al. (2012a), and this is to be expected as SED shapes vary greatly at this wavelength (see Figure 4 of Brown et al., 2019).

We present all of our IR bolometric corrections in Figures 3.8 and 3.9. From Table 3.7 we can see that our bolometric corrections for all our AGNs have gradients between 1.04 -1.14. That is, the gradients of our bolometric corrections remain constant with wavelengths whereas the Runnoe et al. (2012b) gradients vary between 0.69 and 0.98 (this can clearly be seen in Figures 3.8 and 3.9). We also see little scatter in the shorter wavelength bolometric corrections (1.5 μm, 2 μm and 3 μm) as there is little variation in the SEDs at these wavelengths. Our 3 μm bolometric correction agrees well with that of Richards et al. (2006b) and

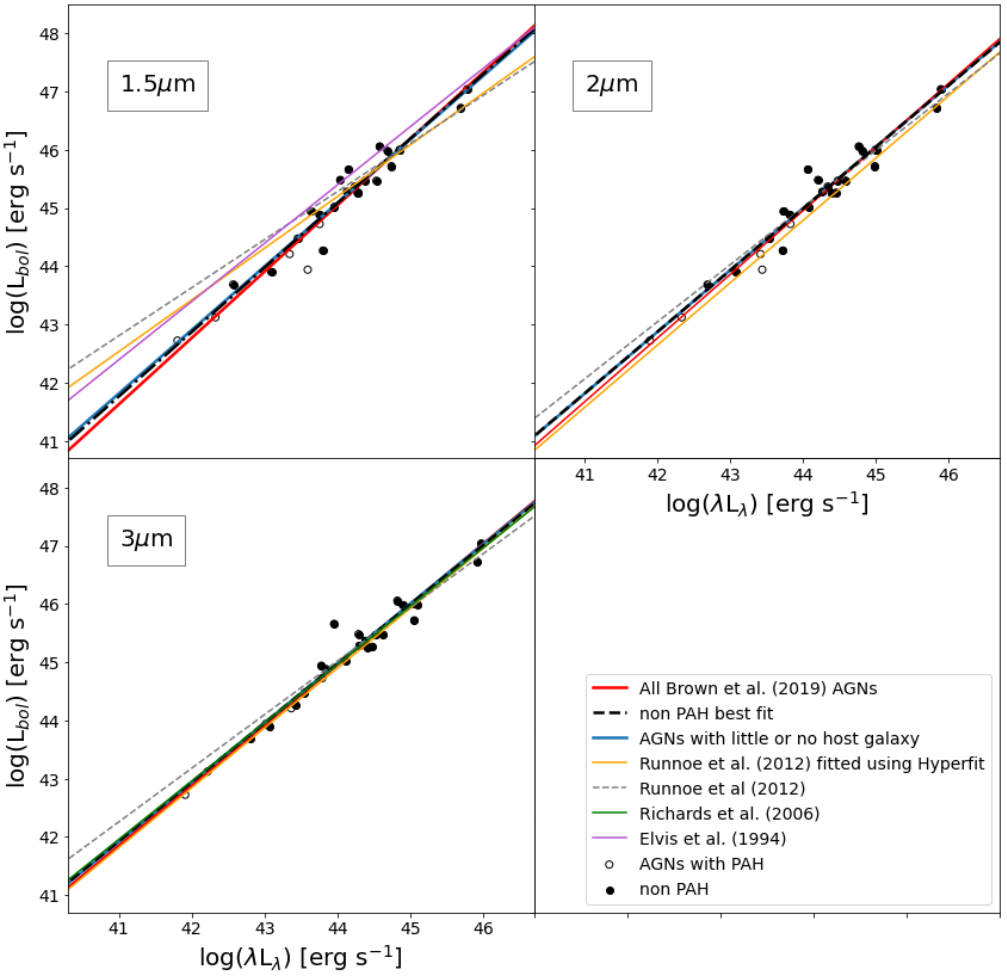

FIGURE 3.8: 1.5 μm, 2 μm and 3 μm bolometric corrections. Our bolometric corrections agree with that of Elvis et al. (1994), Richards et al. (2006b) and Runnoe et al. (2012a) at higher luminosities.

Runnoe et al. (2012b) with gradients of 0.96 and 1.03, respectively, in comparison to the 1.04 gradient of our best fit for all AGNs.

As stated in Section 3.4.3, we measured bolometric corrections for multiple subsamples of the full 27 Brown et al. (2019) AGN SEDs. These subsamples include a sample of AGNs with no visible PAHs and a sample of AGNs with no PAHs and little or no host galaxy contamination. We find that the bolometric correction gradients for the sample of AGNs with no PAHs varies between 0.02 - 0.15 (with the median difference in variation being 0.06) of that of the full sample, where the largest variation is in the 24 μm bolometric correction. This result reflects what we see for the sample of AGNs with little or no host galaxy contamination. The gradients vary between 0.02 - 0.14 for $\lambda < 24$ μm, and the variation for

24 μm is 0.26. This large variation in 24 μm slopes can be attributed to the large 1σ scatter of ≈ 0.50 dex for the bolometric corrections, which reflects the variability in SEDs at this wavelength.

The median host galaxy light fraction of our AGNs (discussed in Section 3.4.3), measured in the H-band, was 0.22; this corresponds to just 0.11 dex. This fraction is relatively small in comparison to our scatter which is between 0.19 - 0.51 dex for the full AGN sample. Our bolometric corrections for AGNs with little or no host galaxy light match closer to Runnoe et al. (2012b) corrections than any of our other subsamples. This makes sense as Runnoe et al. (2012b) use H-band host galaxy light fractions to correct their SEDs for host galaxy contamination. As with all of our bolometric corrections, the Runnoe et al. (2012b) corrections agree with ours at higher luminosities.

The three major outliers in our bolometric corrections are Mrk 421, Mrk 231 and PKS 1345+12, where Mrk 231 and PKS 1345+12 are red objects, which produce most of their energy beyond 24 μm. The Brown et al. (2019) SEDs for these two AGNs extends out to 500 μm and we remeasure the bolometric luminosity for these two AGNs, integrating from 500 μm to 8 keV. We find that their $\log(L_{bol})$ increase to 46.17 ± 0.10 erg s^{-1} and 45.93 ± 0.10 erg s^{-1} from 45.72 ± 0.10 erg s^{-1} and 45.47 ± 0.10 erg s^{-1} for Mrk 231 and PKS 1345+12, respectively. These bolometric luminosities would move these AGNs upward in Figure 3.9, where they would sit much closer to our measured bolometric correction line of best fit. This increase in bolometric luminosity shows that the choice of integration range can effect the measured bolometric correction, whereby a wider integration range will allow the measured bolometric luminosities of objects to be closer to the true bolometric luminosity. This is particularly true when determining the bolometric corrections for a range of AGN types with differing emission mechanisms. Mrk 421 is a BL Lac object, the SED for this AGN is featureless and different to the other AGNs in our sample and thus we do not expect it to agree with the best fits for our bolometric corrections.

Mrk 421 and Mrk 231 (Compton thick AGNs) are two major outliers in our IR bolometric corrections. For this reason, we removed these AGNs from our 'all AGNs' sample and our 'AGNs with no PAH' sample in order to see the effects

that Compton thick AGNs may have on our sample. The bolometric corrections of the samples excluding the Compton thick AGNs are provided in Table 3.8. From the results we can see that the gradients of the bolometric corrections in the optical and UV varies by 0.01 - 0.05 for the full sample minus the Compton thick AGNs compared to the original sample. In the optical and UV, for the sample of AGNs with no PAH minus the Compton thick AGNs, the gradients vary by 0.01 - 0.04 from the original 'AGNs with no PAHs' sample. These variations in the gradient is within the stated uncertainties for the gradients, and thus does not affect the overall bolometric correction in a significant way.

The IR bolometric corrections gradients varied by 0.0 - 0.05 for the full sample minus the Compton thick AGNs compared with the original full sample. For the sample of AGNs with no PAH minus the Compton thick AGNs, the IR bolometric corrections gradients varied by 0.01 - 0.10. The largest variations in the bolometric corrections were seen at 15 μm and 24 μm with variations of 0.07 and 0.10 in gradient. This variation is at the 1σ level. For all wavelengths (optical, UV and IR) we measure a 1σ vertical scatter that is less than the original samples and this is to be expected as Mrk 421 and Mrk 231 were outliers.

3.6 Bolometric corrections for all Brown et al 2019 SEDs

To test whether our results depend on the sample selection, we undertake tests using an expanded sample. As mentioned in previous sections, we measured the bolometric corrections using 27 AGNs from Brown et al. (2019) as these SEDs had data that extended to the X-ray, whereas the remaining 14 AGN SEDs from Brown et al. (2019) did not. For the 14 SEDs that did not have X-ray data, we populate the X-ray wavelengths using archival data from the NASA/IPAC Extragalactic Database (NED)[1]. We find that 13 AGNs have archival X-ray photometry (IRASF16156+0146 did not have photometry in the X-ray), with two AGNs having only one data point in the X-ray. The X-ray data for each

[1] https://ned.ipac.caltech.edu The NASA/IPAC Extragalactic Database (NED) is funded by the National Aeronautics and Space Administration and operated by the California Institute of Technology.

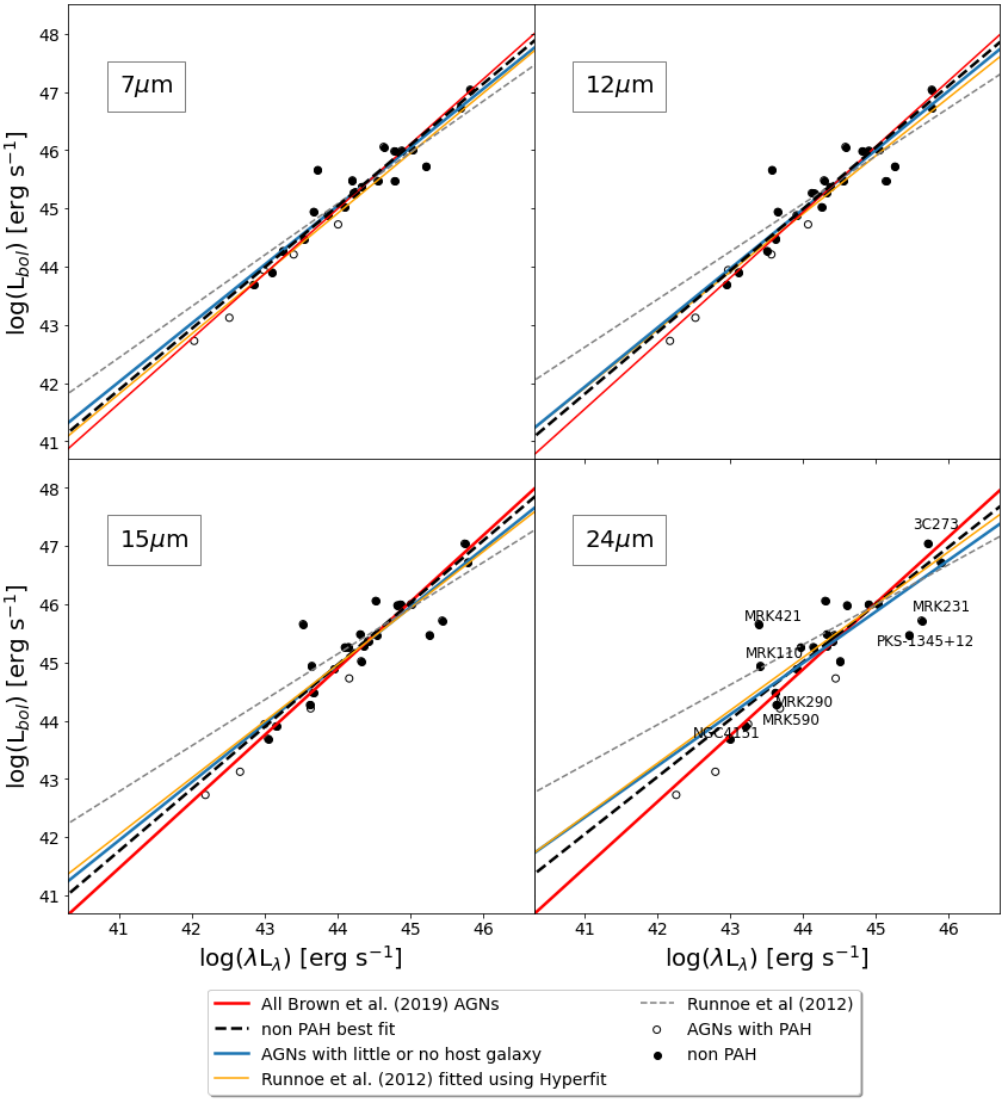

FIGURE 3.9: 7 μm, 12 μm, 15 μm and 24 μm bolometric corrections, where the grey dashed line and yellow lines are Runnoe et al. (2012a) bolometric corrections, measured using minimising-χ^2 and Hyper-fit, respectively. Our bolometric corrections agree with that of Runnoe et al. (2012a) at higher luminosities. An important point that this figure displays is the consistency of our gradients with wavelength, where the gradients from Runnoe et al. (2012b) vary by small amounts with wavelength.

TABLE 3.7: Our IR bolometric corrections with non zero intercept in the form $\log(L_{bol}) = A + B\log(\lambda L_\lambda)$ measured using Hyper-fit.

λ (μm)	Bolometric Correction	Source	1σ vertical scatter
1.5	$(-5.06 \pm 2.37) + (1.14 \pm 0.05)\log(\lambda L_\lambda)$	This work, all AGNs	0.24
	$(-3.57 \pm 2.96) + (1.11 \pm 0.07)\log(\lambda L_\lambda)$	This work, AGNs with no PAH	0.22
	$(-2.87 \pm 4.03) + (1.09 \pm 0.09)\log(\lambda L_\lambda)$	This work, no host contamination	0.23
	$(-1.18 \pm 1.70) + (1.05 \pm 0.04)\log(\lambda L_\lambda)$	This work, extended list of AGNs	0.24
	$(8.98 \pm 2.03) + (0.83 \pm 0.05)\log(\lambda L_\lambda)$	Runnoe et al. (2012a), minimising-χ^2 fitting	
	$(6.17 \pm 2.10) + (0.89 \pm 0.05)\log(\lambda L_\lambda)$	Runnoe et al. (2012a), Hyper-fit	0.22
2	$(-3.18 \pm 2.02) + (1.09 \pm 0.05)\log(\lambda L_\lambda)$	This work, all AGNs	0.22
	$(-1.56 \pm 2.74) + (1.06 \pm 0.06)\log(\lambda L_\lambda)$	This work, AGNs with no PAH	0.22
	$(-1.62 \pm 3.98) + (1.06 \pm 0.09)\log(\lambda L_\lambda)$	This work, no host contamination	0.23
	$(0.16 \pm 1.53) + (1.02 \pm 0.03)\log(\lambda L_\lambda)$	This work, extended list of AGNs	0.22
	$(1.85 \pm 3.18) + (0.98 \pm 0.07)\log(\lambda L_\lambda)$	Runnoe et al. (2012a), minimising-χ^2 fitting	
	$(-2.29 \pm 3.31) + (1.07 \pm 0.07)\log(\lambda L_\lambda)$	Runnoe et al. (2012a), Hyper-fit	0.18
3	$(-0.60 \pm 1.71) + (1.04 \pm 0.04)\log(\lambda L_\lambda)$	This work, all AGNs	0.19
	$(0.31 \pm 2.58) + (1.02 \pm 0.06)\log(\lambda L_\lambda)$	This work, AGNs with no PAH	0.19
	$(0.05 \pm 3.76) + (1.02 \pm 0.08)\log(\lambda L_\lambda)$	This work, no host contamination	0.23
	$(2.01 \pm 1.41) + (0.98 \pm 0.03)\log(\lambda L_\lambda)$	This work, extended list of AGNs	0.22
	$(4.54 \pm 3.42) + (0.92 \pm 0.08)\log(\lambda L_\lambda)$	Runnoe et al. (2012a), minimising-χ^2 fitting	
	$(-0.29 \pm 3.61) + (1.03 \pm 0.08)\log(\lambda L_\lambda)$	Runnoe et al. (2012a), Hyper-fit	0.21
7	$(-4.01 \pm 2.62) + (1.11 \pm 0.06)\log(\lambda L_\lambda)$	This work, all AGNs	0.28
	$(-1.22 \pm 3.59) + (1.05 \pm 0.09)\log(\lambda L_\lambda)$	This work, AGNs with no PAH	0.28
	$(0.76 \pm 4.94) + (1.01 \pm 0.11)\log(\lambda L_\lambda)$	This work, no host contamination	0.30
	$(3.04 \pm 3.51) + (0.95 \pm 0.08)\log(\lambda L_\lambda)$	This work, extended list of AGNs	0.27
	$(6.31 \pm 4.03) + (0.88 \pm 0.09)\log(\lambda L_\lambda)$	Runnoe et al. (2012a), minimising-χ^2 fitting	
	$(-0.56 \pm 4.42) + (1.03 \pm 0.10)\log(\lambda L_\lambda)$	Runnoe et al. (2012a), Hyper-fit	0.25
12	$(-4.70 \pm 3.40) + (1.13 \pm 0.07)\log(\lambda L_\lambda)$	This work, all AGNs	0.35
	$(-1.63 \pm 4.69) + (1.06 \pm 0.11)\log(\lambda L_\lambda)$	This work, AGNs with no PAH	0.36
	$(0.21 \pm 6.66) + (1.02 \pm 0.15)\log(\lambda L_\lambda)$	This work, no host contamination	0.39
	$(-1.26 \pm 2.33) + (1.05 \pm 0.05)\log(\lambda L_\lambda)$	This work, extended list of AGNs	0.33
	$(8.92 \pm 4.30) + (0.82 \pm 0.10)\log(\lambda L_\lambda)$	Runnoe et al. (2012a), minimising-χ^2 fitting	
	$(1.00 \pm 4.43) + (1.00 \pm 0.11)\log(\lambda L_\lambda)$	Runnoe et al. (2012a), Hyper-fit	0.27
15	$(-5.40 \pm 4.01) + (1.14 \pm 0.09)\log(\lambda L_\lambda)$	This work, all AGNs	0.40
	$(-1.94 \pm 5.49) + (1.07 \pm 0.12)\log(\lambda L_\lambda)$	This work, AGNs with no PAH	0.41
	$(0.89 \pm 7.57) + (1.00 \pm 0.17)\log(\lambda L_\lambda)$	This work, host contamination	0.44
	$(-2.07 \pm 2.67) + (1.07 \pm 0.06)\log(\lambda L_\lambda)$	This work, extended list of AGNs	0.36
	$(10.51 \pm 4.39) + (0.79 \pm 0.10)\log(\lambda L_\lambda)$	Runnoe et al. (2012a), minimising-χ^2 fitting	
	$(2.23 \pm 4.98) + (0.97 \pm 0.11)\log(\lambda L_\lambda)$	Runnoe et al. (2012a), Hyper-fit	0.28
24	$(-5.19 \pm 5.25) + (1.14 \pm 0.12)\log(\lambda L_\lambda)$	This work, all AGNs	0.51
	$(1.57 \pm 6.29) + (0.99 \pm 0.14)\log(\lambda L_\lambda)$	This work, AGNs with no PAH	0.49
	$(6.09 \pm 7.89) + (0.88 \pm 0.18)\log(\lambda L_\lambda)$	This work, no host contamination	0.49
	$(-2.71 \pm 3.40) + (1.08 \pm 0.08)\log(\lambda L_\lambda)$	This work, extended list of AGNs	0.45
	$(15.04 \pm 4.77) + (0.69 \pm 0.21)\log(\lambda L_\lambda)$	Runnoe et al. (2012a), minimising-χ^2 fitting	
	$(5.11 \pm 5.66) + (0.91 \pm 0.13)\log(\lambda L_\lambda)$	Runnoe et al. (2012a), Hyper-fit	0.33

TABLE 3.8: Our optical/UV and IR bolometric corrections, when Compton thick AGNs are removed form the sample, with non zero intercept in the form $\log(L_{bol}) = A + B\log(\lambda L_\lambda)$ measured using Hyper-fit.

λ (μm)	Bolometric Correction	Source	1σ vertical scatter
1450	$(12.51 \pm 2.57) + (0.74 \pm 0.06)\log(\lambda L_\lambda)$	This work, all AGNs	0.38
	$(11.59 \pm 3.91) + (0.76 \pm 0.09)\log(\lambda L_\lambda)$	This work, AGNs with no PAH	0.40
3000	$(5.02 \pm 1.99) + (0.91 \pm 0.04)\log(\lambda L_\lambda)$	This work, all AGNs	0.25
	$(5.10 \pm 2.92) + (0.91 \pm 0.07)\log(\lambda L_\lambda)$	This work, AGNs with no PAH	0.26
5100	$(-0.07 \pm 1.32) + (1.03 \pm 0.03)\log(\lambda L_\lambda)$	This work, all AGNs	0.15
	$(0.67 \pm 1.87) + (1.01 \pm 0.04)\log(\lambda L_\lambda)$	This work, AGNs with no PAH	0.16
1.5	$(-3.91 \pm 1.94) + (1.11 \pm 0.04)\log(\lambda L_\lambda)$	This work, all AGNs	0.20
	$(-3.68 \pm 2.83) + (1.11 \pm 0.06)\log(\lambda L_\lambda)$	This work, AGNs with no PAH	0.21
2	$(-2.57 \pm 1.50) + (1.08 \pm 0.03)\log(\lambda L_\lambda)$	This work, all AGNs	0.16
	$(-2.08 \pm 2.17) + (1.07 \pm 0.05)\log(\lambda L_\lambda)$	This work, AGNs with no PAH	0.17
3	$(-0.79 \pm 1.09) + (1.04 \pm 0.02)\log(\lambda L_\lambda)$	This work, all AGNs	0.12
	$(-0.41 \pm 1.59) + (1.03 \pm 0.04)\log(\lambda L_\lambda)$	This work, AGNs with no PAH	0.13
7	$(-5.08 \pm 1.71) + (1.14 \pm 0.04)\log(\lambda L_\lambda)$	This work, all AGNs	0.17
	$(-3.04 \pm 2.16) + (1.09 \pm 0.05)\log(\lambda L_\lambda)$	This work, AGNs with no PAH	0.16
12	$(-6.25 \pm 2.49) + (1.16 \pm 0.06)\log(\lambda L_\lambda)$	This work, all AGNs	0.24
	$(-4.09 \pm 3.30) + (1.11 \pm 0.07)\log(\lambda L_\lambda)$	This work, AGNs with no PAH	0.24
15	$(-7.67 \pm 3.04) + (1.19 \pm 0.07)\log(\lambda L_\lambda)$	This work, all AGNs	0.29
	$(-5.43 \pm 4.04) + (1.14 \pm 0.09)\log(\lambda L_\lambda)$	This work, AGNs with no PAH	0.29
24	$(-7.69 \pm 4.49) + (1.19 \pm 0.10)\log(\lambda L_\lambda)$	This work, all AGNs	0.41
	$(-3.11 \pm 5.31) + (1.09 \pm 0.12)\log(\lambda L_\lambda)$	This work, AGNs with no PAH	0.39

of the 13 AGN SEDs consists of photometry from multiple sources and these sources are Piconcelli et al. (2005), Shinozaki et al. (2006), Bianchi et al. (2009), Massaro et al. (2009), Wang et al. (2016) and Paliya et al. (2017).

To utilise this data, while mitigating inaccuracies that may be caused as a result of using it, we use a straight line fit from the UV where the Brown et al. (2019) spectra ends through the X-ray data that we have obtained from NED. This is unlike what we did with the 27 original SEDs that contained X-ray data, where we determined a straight line fit from where the UV data ends to where the X-ray data begins. We show an example of this in Figure 3.10, the blue spectrum (from the IR to the UV) is the SED data from Brown et al. (2019) and the green straight line from the UV through the X-ray data points is the straight line we determined using linear regression. We set this straight line to connect with the

SED data for consistency with how we measured the bolometric luminosities of the original sample of 27 AGNs.

We present the bolometric correction for the IR wavelengths for all 40 AGNs (the original 27 and the 13 AGNs just discussed) in Table 3.7, labeled as 'extended list of AGNs'. The bolometric corrections we measure using 40 AGNs have median gradient differences of 0.04, 0.07 and 0.04 from the 'no host contamination' sample, the original 27 AGN sample and non-PAH sample, respectively. Thus we find that adding more AGNs into the sample has a negligible effect on the overall bolometric corrections that we measure. It should also be noted that changes to the 1σ scatter of the bolometric corrections are negligible with the scatter decreasing by a median of 0.02 dex between the 27 AGN sample and the extended AGN sample.

3.7 Summary and Conclusions

In this chapter we measured AGN bolometric corrections for IR wavelengths using the Brown et al. (2019) AGN SEDs, integrating from 24 μm - 8 keV. We used these SEDs as they are the best available at this time and include a range of AGN types; including obscured, unobscured and BL Lac objects. The Brown et al. (2019) SEDs cover a wide wavelength range, with coverage to at least 0.09 to 30 μm, and in some instances the wavelength coverage extends out to the X-ray, far-IR and radio. They also have more spectrophotometry of individual AGNs than previous SED libraries. Our main SED sample consisted of 27 AGNs that had data coverage from the IR to X-ray wavelengths. We measured bolometric corrections for 1.5 μm, 2 μm, 3 μm, 7 μm, 12 μm, 15 μm and 24 μm as these wavelengths allow for our bolometric corrections to be used for objects that have been observed with *WISE*, *Spitzer* or JWST with a range of redshifts.

We used several subsets of the 27 Brown et al. (2019) SEDs to measure IR bolometric corrections, including measuring bolometric corrections for all 27 AGNs. We selected a sample of AGNs that contained no PAHs (22 AGNs) and a sample with little or no host galaxy contamination (16 AGNs). To determine the effects of sample size on our bolometric corrections, we included an additional

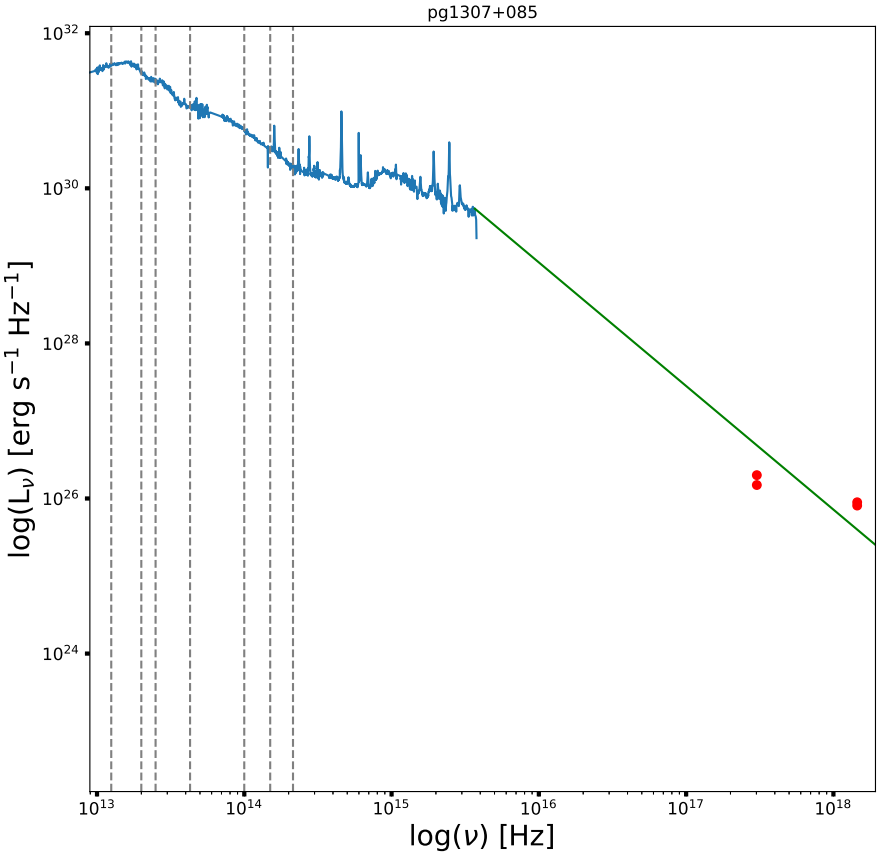

FIGURE 3.10: PG1307+085, a Brown et al. (2019) SED without X-ray data. The X-ray data for this AGN is obtained from 2 different sources. We use a straight line fit from the UV through the X-ray in log-log space, this is the green line in the figure.

13 Brown et al. (2019) AGN SEDs that do not have X-ray data, to our original 27 AGNs (bringing the sample to 40 AGNs), where we used archival X-ray data to measure bolometric corrections for this larger sample. We find that overall the bolometric corrections measured using the four AGN samples were comparable with the gradients of the bolometric corrections remaining close to 1 for all samples.

Host galaxy contamination was determined using the H-band host galaxy fractions from McLeod & Rieke (1994a) and McLeod & Rieke (1994b), where 8 of our AGNs had archival measurements. We measured bolometric and monochromatic luminosities for the 8 AGNs where we had available H-band fractions using the

same method as Shang et al. (2011) and they are provided in Table 3.4. In the IR, only the 1.5 µm, 2 µm and 3 µm monochromatic luminosities decreased as a result of host galaxy removal, which was to be expected as the H-band peaks at 1.635 µm. The largest decrease was seen at 1.5 µm, H-band, and ranged from 0.01 - 0.22 dex. Other optical/UV and IR monochromatic luminosities had decreases in monochromatic luminosity of < 0.01 dex.

When archival H-band fractions, and HST galaxy imaging is unavailable, an avenue one can take is to explore SED AGN and host galaxy decomposition. However, Pacifici et al. (in prep,. private communication) illustrate that it is difficult to use SED-fitting codes to measure the host galaxy fraction, particularly when the fraction is greater than 20 %. This is because these SED-fitting codes are highly dependant on the priors and library of models employed, AGN models used can also be constrained. Thus, measurements of galaxy decomposition on individual SEDs can be highly variable.

Our SEDs cover a wider luminosity range, ($\log(L_{bol}) \approx 42.5$ - 47.5 erg s^{-1}) extending to lower luminosities than those in the literature, where we include different types of AGNs; including obscured and unobscured AGNs and a BL Lac object. In comparison, Runnoe et al. (2012b) and Richards et al. (2006b) favour higher luminosity AGNs which are mostly unobscured ($\log(L_{bol}) \approx 45.5$ - 47.5 erg s^{-1} for Runnoe et al., 2012b). We find that our IR bolometric corrections are comparable to the literature, particularly at higher luminosities where our AGN luminosity range overlaps that of the literature.

Our bolometric corrections measured using our 'no host contamination' sample agree well with the Runnoe et al. (2012b) slopes remeasured using Hyperfit, with a median difference of 0.02 in gradients. Runnoe et al. (2012b) remove host galaxy contamination from their AGNs, which explains why our 'no host contamination' agree with Runnoe et al. (2012b) so well. It should be noted that the fitting method used also plays an important part in this agreement. The remeasured Runnoe et al. (2012b) gradients (remeasured using Hyper-fit) were steeper by 0.06 - 0.23, bringing the new gradients closer to 1 and thus closer to the gradients of our bolometric corrections.

We find that our 1σ scatter increases with wavelength for IR bolometric corrections and this is seen across all our various samples and also reflects what is observed by Runnoe et al. (2012b) for their bolometric corrections. We record the highest scatter for our 24 μm bolometric correction (0.49 dex for the 'no host contamination' sample). The lowest scatter is seen for our 1.5 μm, 2 μm and 3 μm slopes with a scatter of 0.23 dex for all three bolometric corrections.

Chapter 4

Infrared AGN Luminosity Function

4.1 Introduction

Understanding the evolution of quasars and AGNs, and their role in galaxy evolution, has been a topic of interest since the identification of the first quasars and their corresponding redshifts (Schmidt, 1963). AGNs are fueled by accretion of gas into the black hole, where some of the energy is fed back into the galaxy, leading to heating of gas which could truncate star formation (Silk & Rees, 1998; Fabian, 1999a). The luminosity function provides a constraint on the fraction of SMBHs that are actively accreting, and the rate of that accretion (e.g. Yu & Tremaine, 2002; Falcón-Barroso et al., 2006; Fabian, 2012; Yang et al., 2012; Wang et al., 2013).

The space density of AGNs has previously been measured using optical, UV and X-ray wavelengths (e.g. Dunlop & Peacock, 1990; Ueda et al., 2003; Richards et al., 2005; Ross et al., 2013; Tuccillo et al., 2015; Retana-Montenegro & Röttgering, 2020; Zhang et al., 2021). Typically AGN luminosity functions are measured at $z > 0.3$ (e.g. Fontanot et al., 2007; McGreer et al., 2013; Tuccillo et al., 2015; Niida et al., 2020; Onken et al., 2021), where the quasars appear as compact optical sources and are little impacted by host galaxy light.

However, Type 2 quasars are a population of AGNs that could be missed by most AGN surveys (Houck et al., 2005; Eckart et al., 2010; Alexandroff et al., 2013; Yuan et al., 2016, and references therein). Type 2 quasars are very luminous AGNs with only narrow optical emission lines, which according to the unified model of AGNs is caused by the torus obscuring the broad line region. The obscuring gas and dust is often very thick, with dust obscuration of $0.5 \leq$ E(B-V) ≤ 1.5 (e.g. Banerji et al., 2015, and references therein) and column densities of $N_H \simeq 1.5 \times 10^{24}$ cm^{-2} (Comastri, 2004), which is referred to as being Compton thick.

The X-ray traces emission from the hot corona and the ionized reflection of the X-ray continuum from distant neutral material like the torus, the BLR, the NLR and accretion disk (George & Fabian, 1991; Antonucci, 1993; Bianchi et al., 2008). However, the soft X-ray is sensitive to electron attenuation (Padovani et al., 2017). On the other hand, the IR traces warm dust, attributed to the torus and is therefore unaffected by dust obscuration (Padovani et al., 2017). Type 2 quasars are therefore picked up by hard X-ray and IR surveys (e.g. Brightman et al., 2017).

Yuan et al. (2016) searched for $z \leq 1$ type 2 quasars and selected a sample of 2758 type 2 quasars from the SDSS-III/BOSS spectroscopic database (Alam et al., 2015), of ≈ 1.5 million galaxies, using emission line properties. When they cross matched these quasars using *WISE* colours, they found that, even though they used IR colour, only 34 % of their 2758 type 2 quasars are identified. This result highlights difficulty in selecting complete samples of type 2 quasars.

Optical, UV and (soft) X-ray AGN surveys therefore tend to favour AGNs that are mostly unobscured (type 1 AGNs) (e.g. Ueda et al., 2003; Richards et al., 2005; Han et al., 2012) and miss obscured AGNs (type 2). This is particularly true for AGN surveys completed in the UV and optical which tend to select the same types of AGNs (i.e. Broadline AGNs). This favouring is clearly shown by Ueda et al. (2003) who compare the distribution of X-ray type 2 AGNs and optical type 2 AGNs to their whole sample. They find that the fraction of optical and X-ray type 2 AGNs is small compared to the overall sample, and the number of type 2 AGNs selected noticeably decreases with increasing redshift.

As well as showing that the fraction of optical type 2 AGNs was less than X-ray type 2 AGNs, Han et al. (2012) compare luminosity functions measured using the IR and X-ray, stating that the X-ray tends to underestimate the number of obscured IR luminous AGNs. As a result, there is a possibility that the space density measured using the UV/optical and X-ray can be an underestimate of the total AGN space density as some obscured yet powerful AGNs may have been missed. Errors in the current AGN bolometric luminosity functions and accretion rate densities therefore may be the result of systematic errors. The IR, however, allows for both obscured and unobscured AGNs to be selected, and thus can be used to measure the space density of AGNs that may be faint in the soft X-ray, UV and optical but are bright in the IR.

Motivated by this, in this chapter we use photometry and spectroscopy from the Galaxy And Mass Assembly survey (GAMA: e.g., Driver et al., 2011; Wright et al., 2016) to measure the *WISE* 3.4μm AGN luminosity function. We use the WISE W1 filter as we expect spectra at this wavelength are relatively smooth and the uncertainties in bolometric corrections are relatively small (*sim* 0.19 dex), as discussed in Chapter 3 of this thesis. We select AGNs using IR colour and emission line ratios in order to select both obscured and unobscured AGNs; we use this sample to derive our luminosity function. The use of GAMA means that spectra are available for almost all potential host galaxies in the relevant redshift range. This is different from AGN surveys that select candidates using photometry/colours which require follow up observations (e.g. Croom et al., 2004; Hasinger et al., 2005). Finally we discuss our measured IR luminosity functions and compare them with AGN luminosity functions from the literature to determine whether AGN populations have been overlooked in previous luminosity function measurements. Throughout this Chapter we use AB magnitudes (unless stated otherwise), and a Hubble constant of $H_0 = 70$ km s^{-1} Mpc^{-1}.

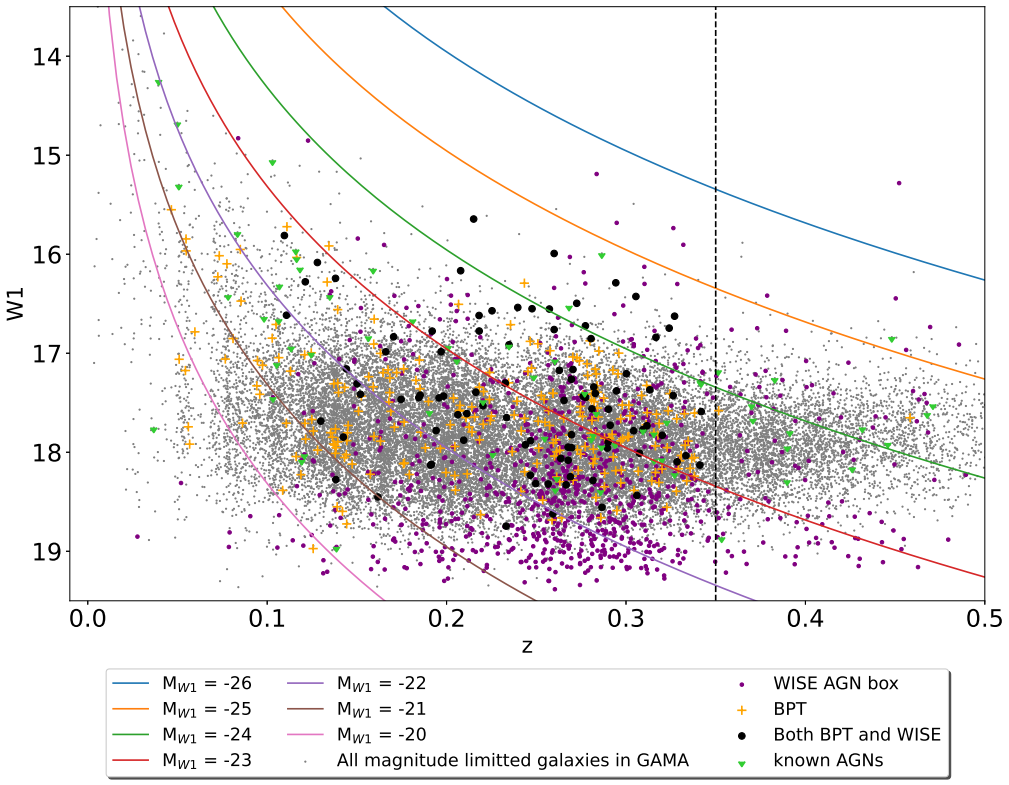

FIGURE 4.1: Apparent magnitude vs redshift figure of our GAMA galaxies with AGNs selected using BPT and *WISE* colour and known AGNs selected using Véron-Cetty & Véron (2010) indicated. We measure our luminosity function for $z < 0.35$ AGNs as this is the redshift limit that the optical emission lines used to select AGNs appear in the GAMA optical spectra. We caution the distribution of overall galaxy magnitudes includes some objects biased by neighbouring foreground stars (e.g., SDSS J084624.98+013553.3). This figure displays that the colour selection picks the most luminous AGNs, including broad line AGNs, while the BPT criterion selects lower luminosity narrow line objects. As such, there is not much overlap between the two criteria.

4.2 AGN sample selection

4.2.1 The GAMA catalogue

We utilise IR photometry and optical emission line measurements from the GAMA survey (Driver et al., 2011; Wright et al., 2016) to colour-, BPT- and emission line-select AGNs. GAMA uses both ground-based and space-based telescopes to measure photometry and spectroscopy of $\approx$ 300,000 galaxies with r-band magnitude < 19.8 mag, including $z < 1$ AGNs. We select our sample from the GAMA equatorial fields.

We use the GAMA Anglo-Australian Telescope spectroscopy for redshifts (Baldry et al., 2014) and emission line ratios determined using the SpecLineSFR GAMA version II catalogue (Gordon et al., 2017). The GAMA survey provides spectra for most of their objects, which means we are able to verify our automated AGN selection as well as visually inspect individual objects. Therefore, there is no need for spectroscopic follow-up of our AGNs. We use *WISE* IR photometry from the Lambda Adaptive Multi-Band Deblending Algorithm in R (LAMBDAR; Wright et al., 2016) catalogue. We use the r-band magnitude < 19.8 mag limit to determine the corresponding W1 limit based on AGN colours.

The goal of our selection methods is to miss as few bright quasars as possible. We measure our luminosity function for $z < 0.35$, this corresponds to the redshift limit that the optical emission lines used to select AGNs all appear in the GAMA optical spectra. The redshift and apparent magnitude range our AGN sample occupies is shown in Figure 4.1 and this figure displays that the colour selection picks up the most luminous AGNs, including broad line AGNs, while the BPT criterion selects lower luminosity narrow objects. The distribution of our AGN sample across the three GAMA equatorial regions is displayed in Figure 4.2; the even distribution of our sample across the three regions shows that our selection criteria are behaving as we would expect.

4.2.2 BPT selected AGNs

We use a BPT diagram (Baldwin et al., 1981), which utilises emission line ratios, to select AGNs in our sample. The BPT diagram uses emission line ratios to separate star forming galaxies from AGNs; this works as emission line ratios are dependent on the temperature and density of the gas, and the UV spectrum incident upon it (Baldwin et al., 1981; Kewley et al., 2001b; Kauffmann et al., 2003). We obtain emission line ratios from the SpecLineSFR GAMA version II catalogue (Gordon et al., 2017), where line measurements are derived from single Gaussian fits to spectral lines including Hα, Hβ, [OIII] and [NII]. We select AGNs according to the more conservative Kewley et al. (2001b) criterion and we also exclude LINERS in our sample (Parkash et al., 2019). The resulting

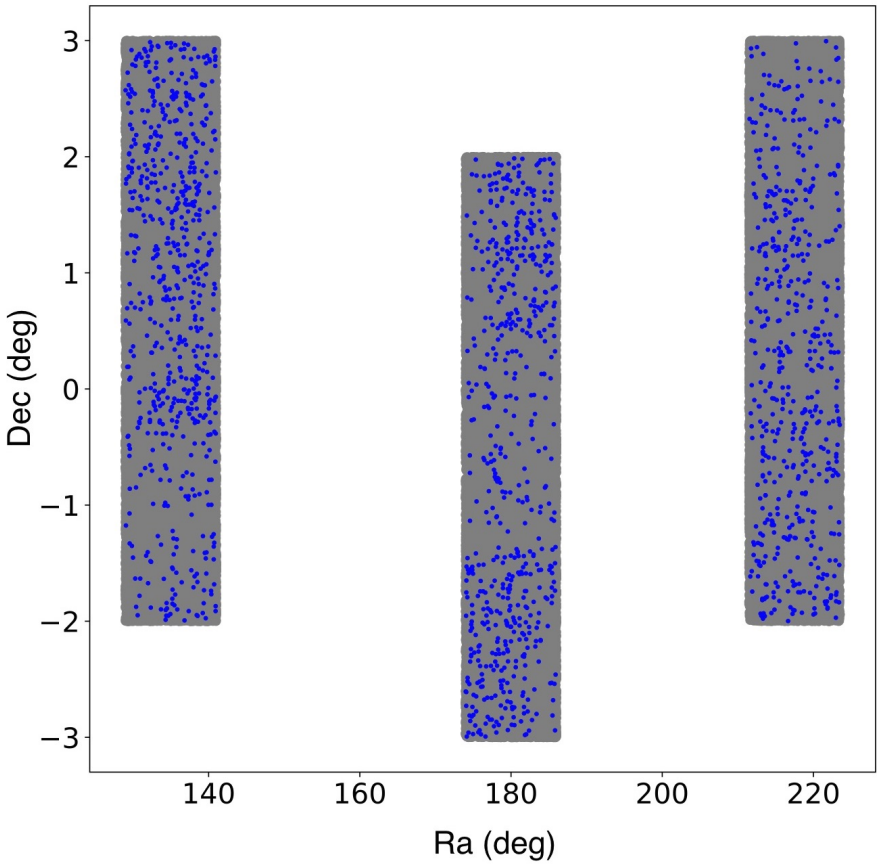

FIGURE 4.2: Distribution of our AGN sample in the three GAMA equatorial fields: G09, G12 and G15.

BPT diagram is displayed in Figure 4.3. We select 344 $z < 0.35$ AGNs based on emission line ratios and some examples of these AGN spectra are shown in Figure 4.4.

4.2.3 Colour selection

Another means by which we select AGNs is using IR colour, specifically using *WISE* colour. AGNs and star forming galaxies both have IR emission from heated dust. However, star forming galaxies have lower dust temperature than AGNs which allows the IR to be used to distinguish between AGNs and star forming galaxies. Different *WISE* colour criteria have been proposed to separate AGNs from star forming galaxies. Stern et al. (2012) and Assef et al. (2013) use

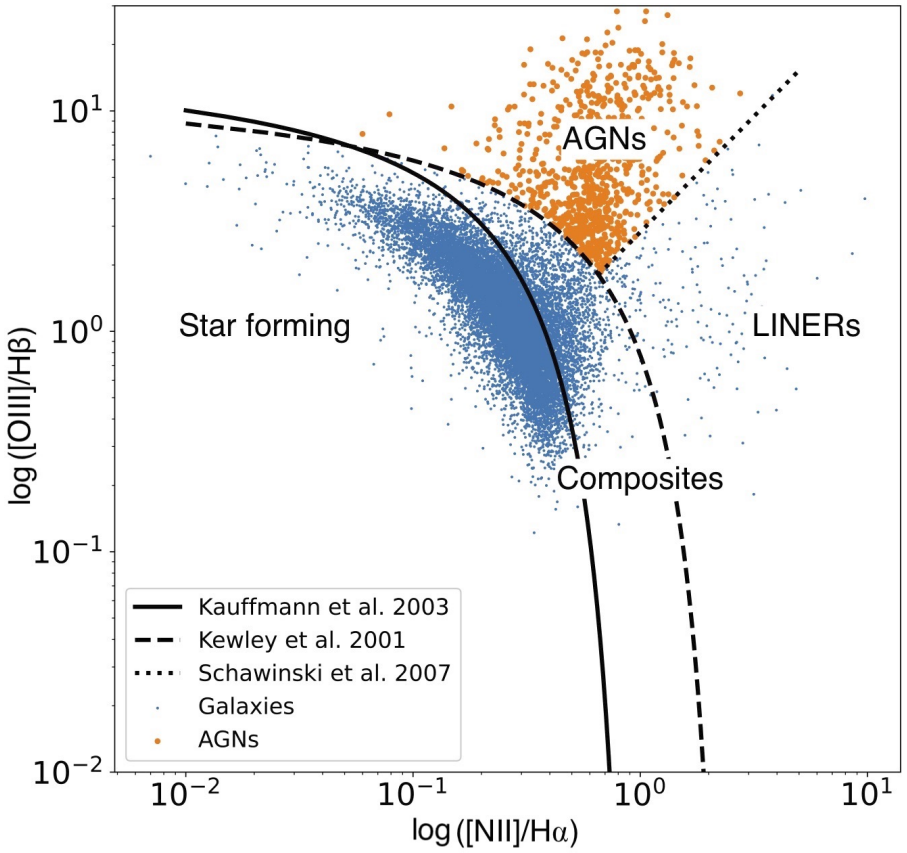

FIGURE 4.3: BPT diagram of GAMA galaxy catalogue. We are using the more conservative Kewley et al. (2001b) criterion rather than the Kauffmann et al. (2003) criterion, we also exclude LINERS.

a more conservative W1 - W2 = 0.16 mag colour criteria to select AGNs on the basis of WISE colour. Stern et al. (2012) discuss that this more conservative criterion is highly complete, whereby it is able to select both obscured and unobscured AGNs. Stern et al. (2012) investigated the use of the more conservative W1 - W2 colour by selecting AGNs from the COSMOS field (Sanders et al., 2007) and determining how many previously known AGNs were recovered. They found that the AGN sample they obtained had a contamination rate of only 5 % and recovered 80 % of possible known AGNs. Motivated by this we use the more conservative WISE colour criteria to select AGNs. We select 938 $z < 0.35$ AGNs using colour and these are displayed in the *WISE* colour-colour diagram in Figure 4.6 and Table 4.1.

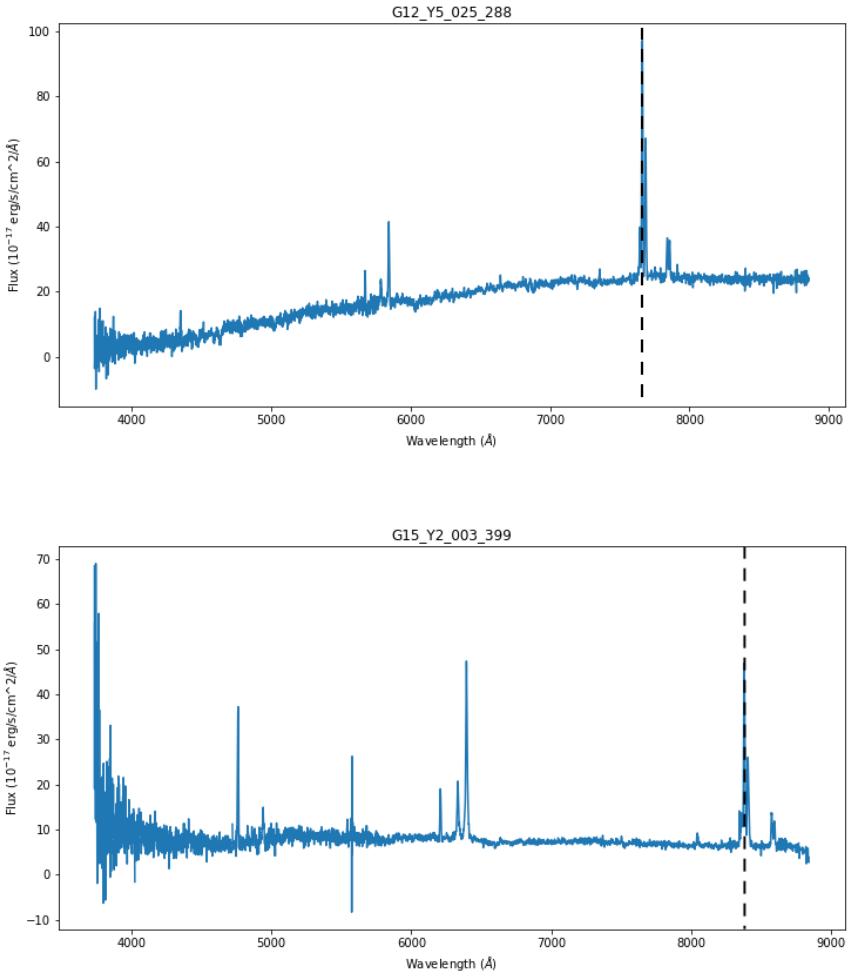

FIGURE 4.4: Examples of AGNs selected using only our BPT criterion; GAMA J121423.95-020034.9 and GAMA J143140.69-012705.2. As expected, these AGNs have narrow Hα peaks with GAMA J143140.69-012705.2 displaying some minor broadening of Hα, where the Hα peak is indicated by a dashed line.

Approximately 25% of the BPT-selected AGNs are also selected with colour, and the rest appear in the star forming region of the colour-colour diagram. Further investigation into individual AGNs in this star forming region showed that they are in fact Seyferts with star forming hosts. We display spectra of $z < 0.35$ AGNs selected with both colour and emission line ratios in Figure 4.5. As expected, these AGNs are unobscured type 1 Seyferts with broad Hα peaks.

We present examples of AGNs selected using the conservative *WISE* criterion in Figure 4.7. The Hα components of these AGNs appears to be broadened even though the Hα and [NII] peaks appear as star forming, which makes them

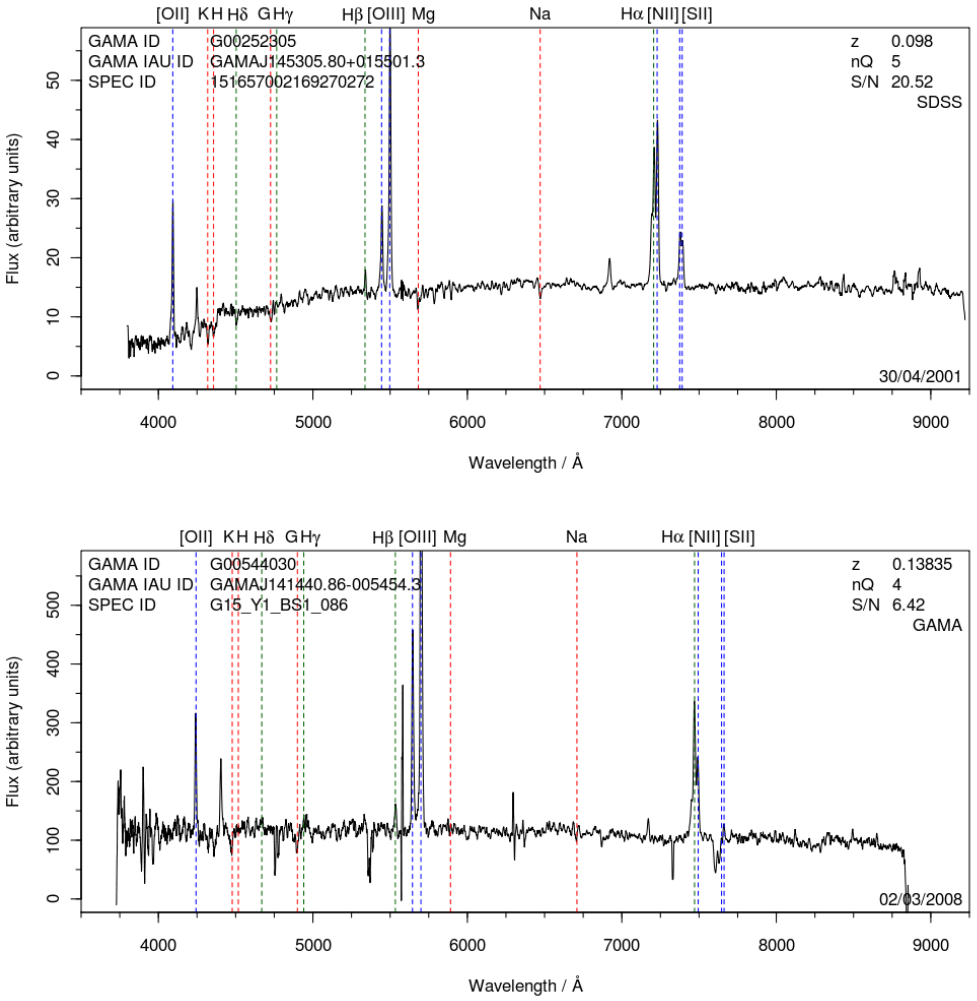

FIGURE 4.5: BPT selected AGNs that appears in the 'AGN' box region of the *WISE* colour-colour diagram. These AGNs have clear broadened Hα emission lines.

interesting as this implies the presence of an AGN. These types of AGNs have historically been classified as LIRGs, however as we see here, WISE colours and broadened emission lines imply that they do have a significant AGN component. This population of AGNs are also picked up by Yao et al. (2020). G09_Y1_GS1_242 for example has narrow lines where Hα is stronger than [NII], however there is a broadened component which has a FWHM of 45.72 $\pm$ 2.42 Å($\approx$ 2000 km/s). The star forming lines in this AGN are dominating here, which may lead to it being miss-classified in previous AGN studies.

We also present spectra of galaxies in the star forming region of the *WISE* colour-colour diagram, selected at random, in Figure 4.8 for comparison. Unlike the

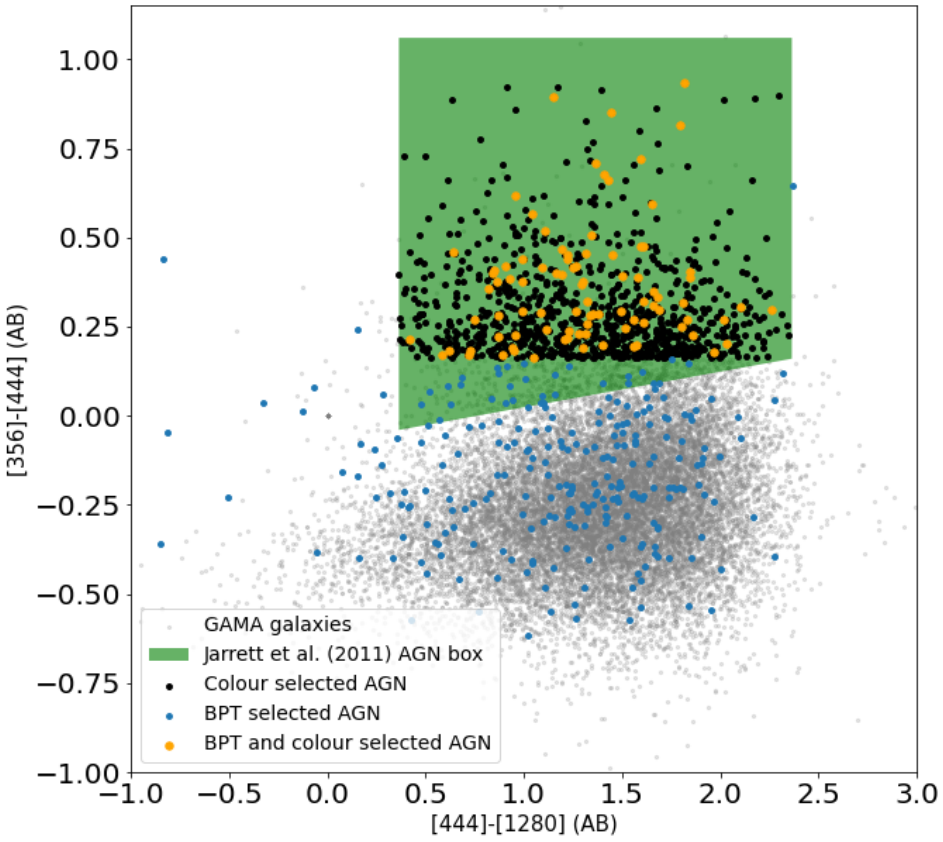

FIGURE 4.6: *WISE* colour-colour diagram of $z < 0.35$ GAMA galaxy catalogue, where AGN are selected using the more conservative Stern et al. (2012) and Assef et al. (2013) criterion, rather than the Jarrett et al. (2011) criteria presented in green. The AGNs selected using both BPT and *WISE* colour are also shown and this is approximately a 25 % of the BPT selected AGNs.

AGNs in Figure 4.7, these galaxies have narrow Hα lines and relatively weak [NII], indicating that they are not AGNs but are star forming galaxies.

4.2.4 Known AGNs

We use the Véron-Cetty & Véron (2010) AGN compilation to select known AGNs that may have been missed by the BPT and IR colour selection. We find that 52 AGNs appear in both the Véron-Cetty & Véron (2010) catalogue and the GAMA catalogue at $z < 0.35$ which also meet our redshift flags and magnitude signal to noise cuts. These AGNs either appear in either SDSS or 2dF (Croom

TABLE 4.1: Numbers of $z < 0.35$ AGNs selected with each method.

Criteria	Number of AGNs
Total BPT selected	344
Only BPT selected	255
Total colour selected	938
Only colour selected	849
Total known AGNs selected using Véron-Cetty & Véron (2010)	52
Known AGNs only selected using Véron-Cetty & Véron (2010)	6
Total =	1199

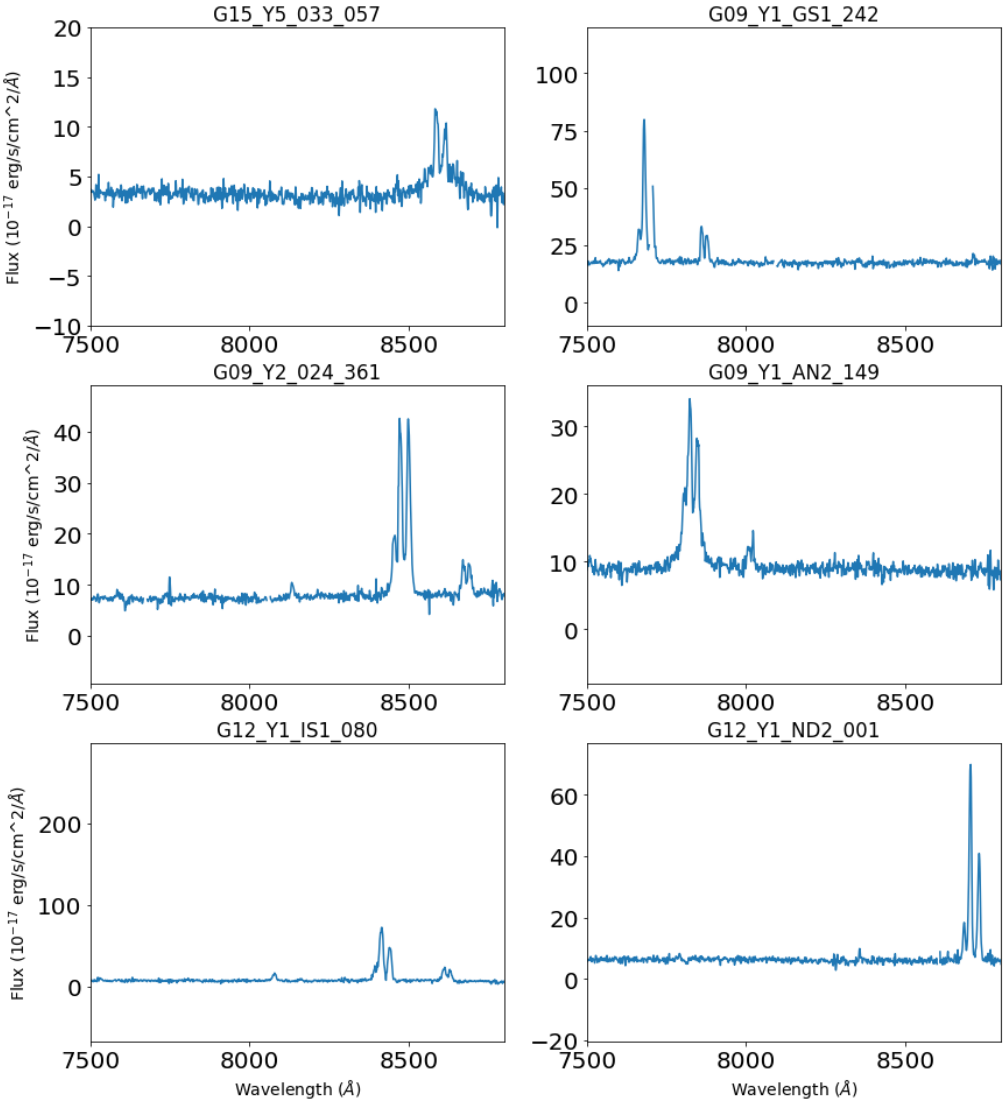

FIGURE 4.7: Examples of colour selected $z < 0.35$ AGNs, where AGN are selected using the more conservative Stern et al. (2012) and Assef et al. (2013) criterion. The Hα emission of most of these AGNs have clear broadened components, particularly at the base, whereas, the Hβ components of these AGNs are also broad.

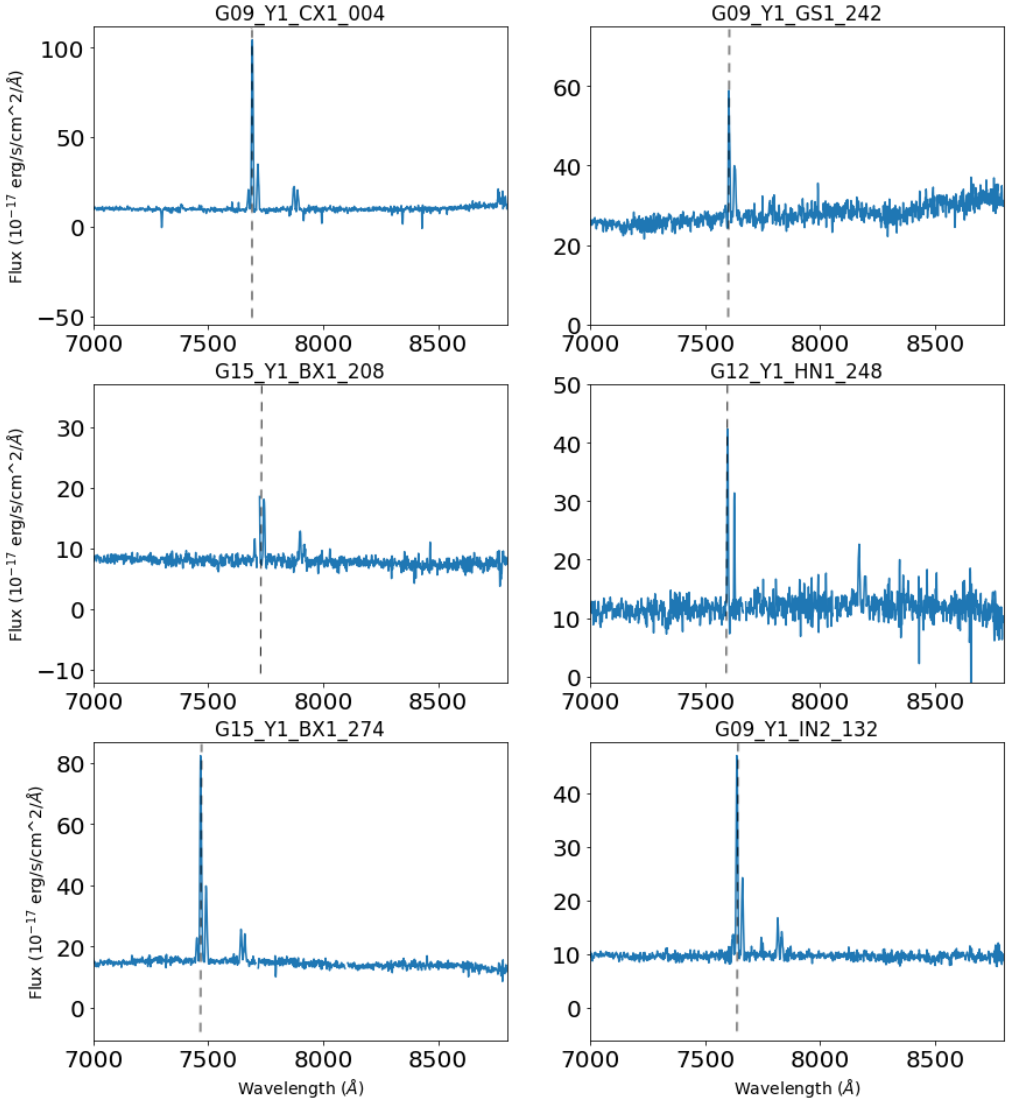

FIGURE 4.8: Galaxies that appear in the star forming region of the *WISE* colour-colour diagram. As expected, these galaxies are narrow Hα emission (indicated by the dashed lines), and do not contain any broadened emission lines.

et al., 2001; Abazajian et al., 2004; Croom et al., 2004; Greene & Ho, 2007). Most of these AGNs (46 AGNs) have been selected using our aforementioned selection criteria.

Using this method we add an additional 6 AGNs to our sample that were not selected by our other criteria. On closer inspection of each of these 6 AGNs, we find the reason that they were not chosen is because they either are in the region of the BPT diagram between the Kauffmann et al. (2003) and Kewley et al. (2001b) criteria or they fall in the star forming region of the BPT criteria. In terms of *WISE* colour, these 6 AGNs either fall in the star forming region of the *WISE* colour-colour diagram, or fall just below the more conservative Stern et al. (2012) and Assef et al. (2013) criteria. The spectra of these 6 AGNs have broad lines, indicating they are indeed AGNs and therefore we add them to our sample. These AGNs have -24 $< M_{W1}$ (mag) $<$ -21 and therefore have negligible effects on the overall luminosity function.

We did this as an exercise to determine whether or not we are selecting the majority of possible AGNs using colour and emission line ratios, rather than with the intention of adding significantly more AGNs to our sample. We do not expect the additional 6 AGNs to have any significant affect on the overall AGN luminosity function.

4.2.5 Comparison with optical colour selection and emission line widths

In order to check whether we select all possible AGNs, we look at the Hα width and flux of our GAMA sample. To obtain emission line data for the GAMA sample we use the SpecLineSFR catalogues (Gordon et al., 2017), which contains two main catalogues; the simple and complex catalogues. They differ in that the simple catalogue uses a single Gaussian fit, whereas the complex catalogue uses two Gaussian components to fit emission lines. The simple catalogue has a flag which indicates which fit to use for a specific galaxy. As the complex catalogue has two Gaussian fits, we use the dominant fit (the broader width measurement of the two fits) to aid in our selection. We select a small random sample of galaxies

with broad Hα width ($>$ 1000 km/s) and then visually inspect each of these spectra to see what percent of that sample contain galaxies with broad-lines but were not selected by our criteria (which may be due to signal to noise restrictions or redshift quality flags). We find our selection criteria are able to pick up all broad line AGNs ($>$ 1000 km/s) that meet our signal to noise restrictions.

We compare our sample with the Richards et al. (2006b) type 1 quasar sample using an optical colour-colour diagram. Richards et al. (2006b) select their quasar sample based on both IR and optical colour and morphology, purposely selecting type 1 quasars. We use an SDSS (u - g) vs (g - r) colour - colour diagram of our $z < 0.35$ AGN sample, presented in Figure 4.9, to compare to the equivalent SDSS colour-colour diagram of the Richards et al. (2006b) sample. The Richards et al. (2006b) quasars have colours of u - g $\approx$ 0.2 and g - r $\approx$ 0.2, whereas our AGNs have redder optical colours of u - g $\approx$ 1 and g - r $\approx$ 0.75. This offset is likely to be because the sample of Richards et al. (2006b) contains only luminous type 1 quasars whereas our sample contains both type 1 and type 2 AGNs. We see that our colour selected AGNs appear to be bluer than our BPT selected AGNs and picks up AGNs with spectra that have at least some broadening of Hα. We expect the BPT selection to be redder than optical colour selection in part because host galaxy light can contribute more to the optical colour. We also see that the bluest AGNs in our sample are dominated by known AGNs.

4.2.6 BPT and Colour of Brown et al. (2019) SEDs

To test the effectiveness of the BPT and WISE colour-colour criteria we use the Brown et al. (2019) AGN SEDs that are also used in Chapter 3. For in depth details into the Brown et al. (2019) SEDs please refer to Section 3.2. We use these SEDs to create a BPT and colour-colour diagram which is displayed in Figure 4.10. The full AGN sample is used to create the colour-colour diagram (left panel of Figure 4.10).

We measure the emission line ratios as well as emission line widths for the AGNs using the code of Sheil et al. (in prep., private communication). We removed AGNs where the fits to the emission lines made using Sheil et al. (in prep.,

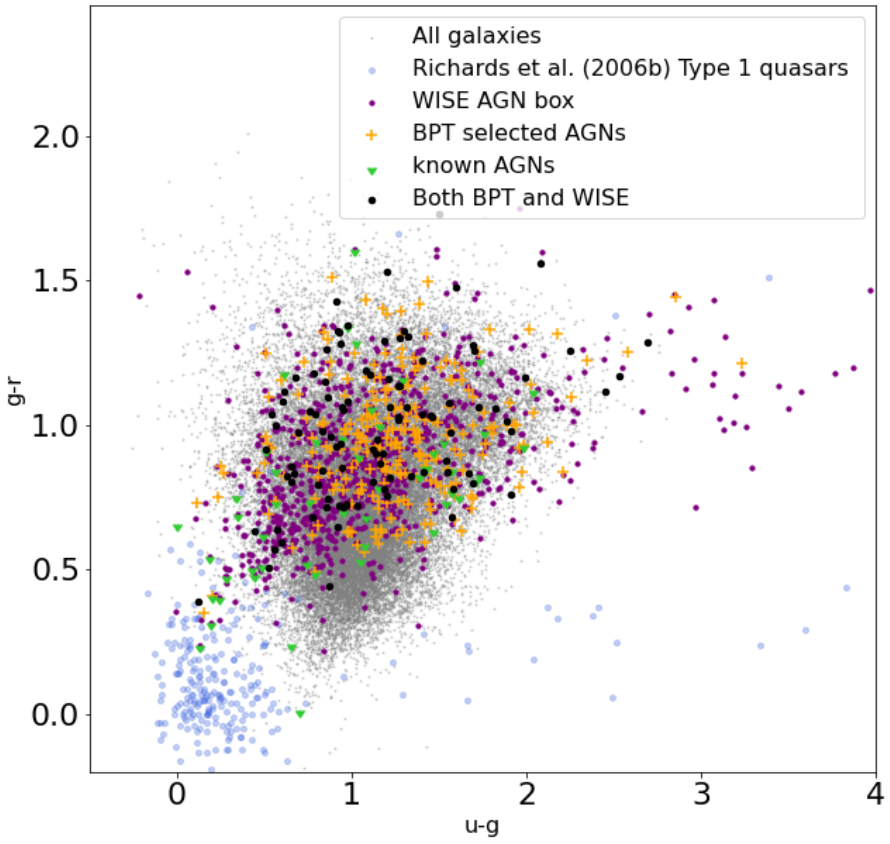

FIGURE 4.9: Optical apparent magnitude colour-colour plot of our selected $z < 0.35$ AGNs. The blue circles represent spectroscopically confirmed SDSS type 1 quasars from Richards et al. (2006b). Our AGNs extends to redder optical colours than Richards et al. (2006b) and this is because Richards et al. (2006b) sample is of Type 1 quasars. Whereas our sample is selected based on IR colour and emission line ratios thus we have both type 1 and type 2 AGNs in our sample.

private communication) didn't properly fit the spectra, by visually inspecting the fit. We found for AGNs where the Hα and [NII] widths > 12 Å(≈ 550 km/s), the Hα and [NII] widths begin to blend, therefore the measurements were inaccurate. Thus to create the BPT diagram (right panel of Figure 4.10), we used only AGNs with Hα and [NII] widths < 12 Å. BL Lacs (OQ 530) and outliers in the BPT diagram that were classified as S1s in Véron-Cetty & Véron (2010) were also removed.

Figure 4.10 shows that all the Brown et al. (2019) SEDs apart from OQ 540 (BL

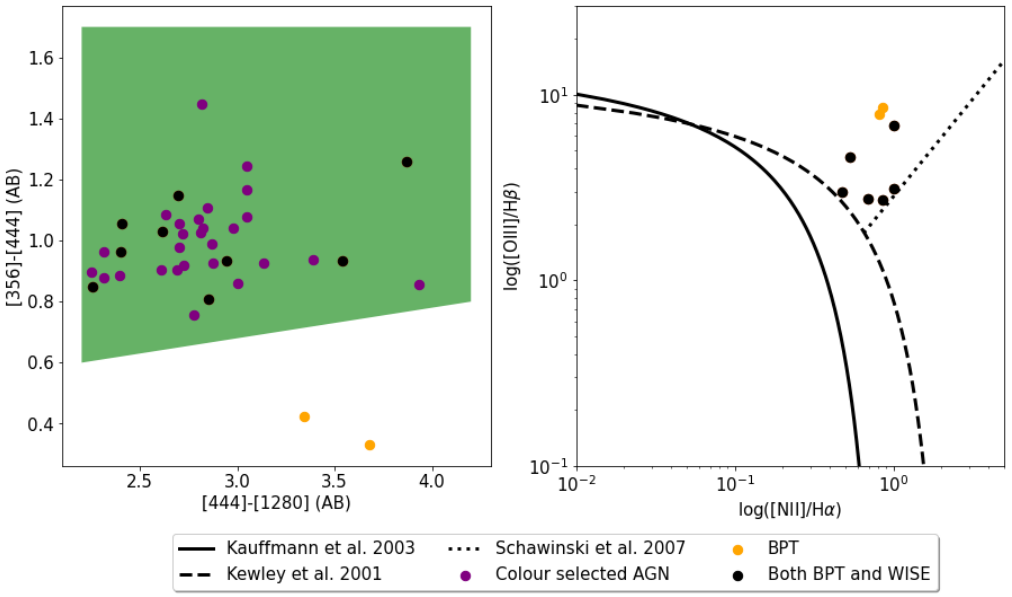

FIGURE 4.10: Colour-colour (left) and BPT (right) plots of the Brown et al. (2019) SEDs. We colour code the AGNs in terms of which criteria they would be identified by. We use all AGNs to create the colour-colour diagram (with the Jarrett et al. (2011) criteria presented in green). To create the BPT diagram we measure fluxes and widths using Sheil et al. (in prep., private communication) and use only AGNs with Hα and [NII] widths of $<$ 12 Å and remove AGNs where the fits of the emission lines were incorrect.

Lac) and Mrk 421 (BL Lac), are classified as AGNs using either the Jarrett et al. (2011) criterion, the BPT criterion or both, which gives confidence for the use of these criteria. The BPT criteria selected all narrow line AGNs and the colour criterion was able to select both narrow and broad line AGNs.

4.2.7 Type 2 quasars

The two most luminous Type 2 quasars in our sample of 1199 AGNs are GAMA J143124.72+012724.3 and GAMA J084359.39-004423.0 and their spectra are presented in Figure 4.11. These objects are selected by our BPT criterion and were picked out from our AGN catalogue by systematically plotting spectra of the brightest to faintest AGNs (in W1) until the two brightest narrow line AGNs were identified. We find that luminous Type 2 quasars make up a very small subset ($\approx$ 4 %) of the most luminous (absolute W1 $<$ -24 mag) AGNs in our full sample. Note that this absolute magnitude limit of $M_{W1} \lessapprox$ -23.95 mag corresponds roughly to the $M_B <$ -22.3 criterion for quasars (Véron-Cetty & Véron,

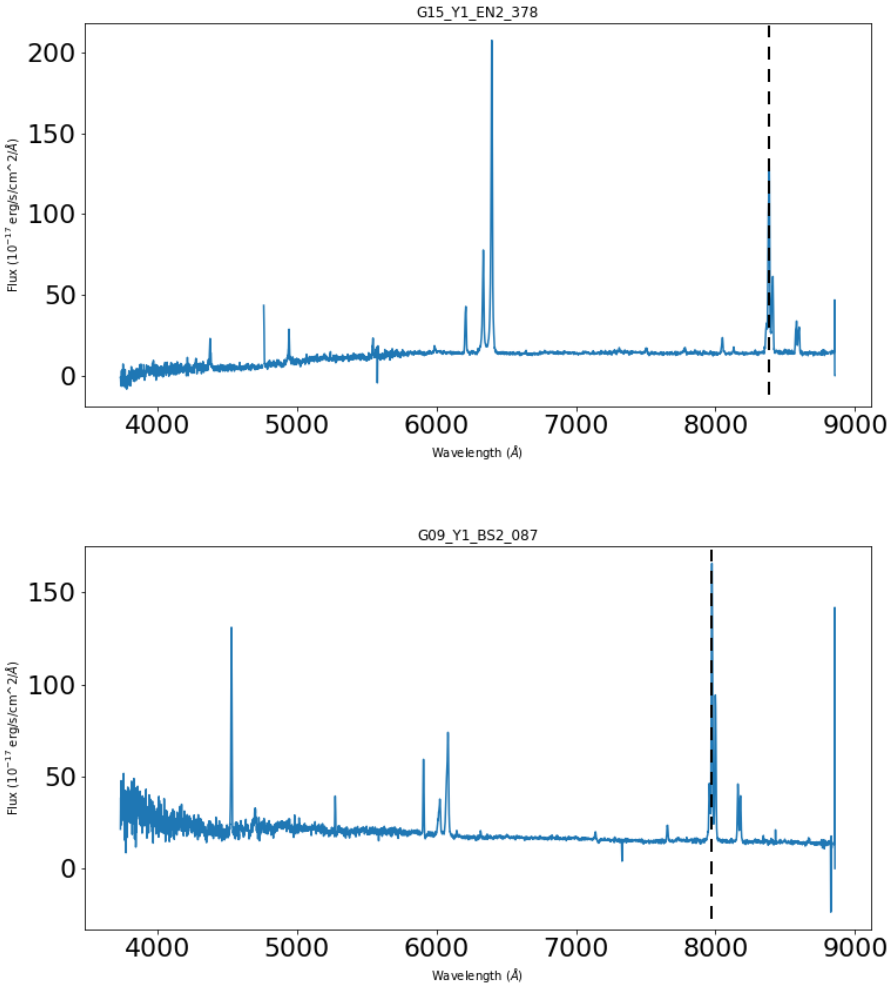

FIGURE 4.11: The two most luminous Type 2 quasars in our sample are GAMA J143124.72+012724.3 (M_{W1} = -24.16) and GAMA J084359.39-004423.0 (M_{W1} = -24.56), where Hα is indicated by the dashed lines. We find that luminous Type 2 quasars make up a very small subset ($\approx$ 4 %) of the most luminous (absolute W1 < -24 mag) AGNs in our sample.

2003). This magnitude was calculated by determining the B - W1 colour using the Brown et al. (2019) AGN SEDs and the methods prescribed in Hogg et al. (2002).

4.3 Absolute magnitudes

We use the methods prescribed by Hogg (1999) to calculate IR (W1) absolute magnitudes for our AGN sample. We calculate the absolute magnitude, M, using;

$$m = M + DM + K \tag{4.1}$$

where m is apparent magnitude and K is k-correction (Hogg, 1999). The distance modulus, DM, is given by;

$$DM \equiv 5\log_{10}\left[\frac{\mathrm{D_L}}{10\mathrm{pc}}\right] \tag{4.2}$$

and it is the difference in magnitude of an objects bolometric flux and the flux one would measure if the object was observed at 10pc. The luminosity distance D_L can be determined using;

$$D_L \equiv \sqrt{\frac{L}{4\pi S}} \tag{4.3}$$

where S is the bolometric flux integrated over all frequencies and L is the bolometric luminosity. As we are using the spectral flux density, f_ν;

$$f_\nu = 3631 \text{ Jy} \times 10^{-0.4\mathrm{m}} \tag{4.4}$$

and luminosity L_ν;

$$L_\nu = 4\pi d^2 f_\nu \tag{4.5}$$

rather than the bolometric fluxes and distance, d, we must apply a k-correction. Since k-correction depends on the spectrum of the object, for our AGNs we use the SED templates presented in Brown et al. (2019).

The k-correction allows us to transform our photometry from observed to rest-frame. We use the steps prescribed in Hogg et al. (2002) to measure the k-corrections for our sample. The k-correction, K_{QR} can be determined using;

$$K_{QR} = -2.5\log_{10}\left[[1+z]\frac{\int \frac{d\nu_o}{\nu_o} f_\nu(\nu_o)R(\nu_o)\int \frac{d\nu_e}{\nu_e} g_\nu^Q(\nu_e)Q(\nu_e)}{\int \frac{d\nu_o}{\nu_o} g_\nu^Q(\nu_o)R(\nu_o)\int \frac{d\nu_e}{\nu_e} f_\nu(\frac{\nu_e}{1+z})Q(\nu_e)}\right] \tag{4.6}$$

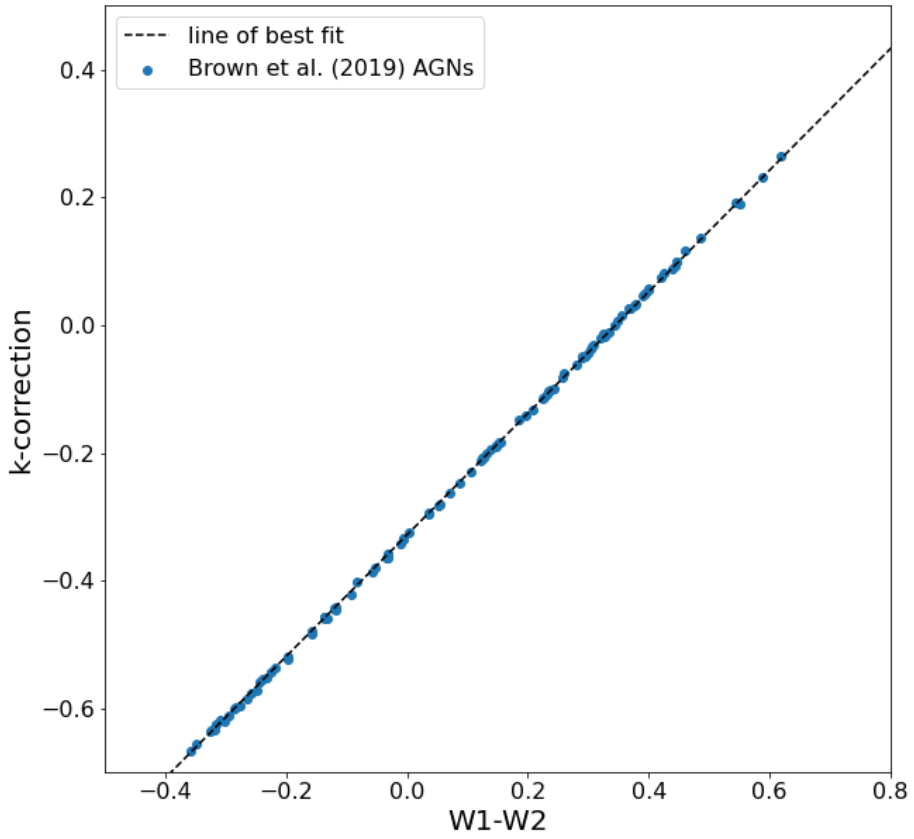

FIGURE 4.12: This is an example of a k-correction used to measure absolute magnitudes. This specific W1-W2 vs k-correction plot is at z = 0.35. We use the Brown et al. (2019) SEDs to measure k-corrections for GAMA AGNs and galaxies.

where $R(\nu)$ describes the bandpass and $f_\nu(\nu_0)$ is the observed-frame flux.

As we do not have SEDs of the AGNs in our sample, we use the Brown et al. (2019) Atlas of AGN SEDs. This Atlas of AGNs includes 113 AGN SEDs, 41 of which are individual AGN SEDs derived from multiwavelegth photometry and archival spectroscopy, and 72 Seyfert SEDs produced by mixing SEDs of the central regions of Seyferts with galaxy SEDs. These SEDs span at least 0.09 to 30 µm, where some SEDs have wavelength coverage beyond this into the X-ray. We first measure the k-corrections and photometry for the Brown et al. (2019) AGNs for *WISE* W1 and W2 for z of 0.01 - 0.40 with a $\Delta z = 0.01$. We are then able to determine a straight line fit between k-correction and W1-W2 colour at

each redshift. An example of this is Figure 4.12 which is determined at z = 0.35. The median scatter for all the k-correction across the redshift range mentioned, measured using median absolute deviation, is 0.15 mag. We then interpolate using GAMA W1 - W2 colour for individual AGNs in our sample. We use an AGN's redshift to determine which W1 - W2 vs k-correction function to use, then interpolate using the W1 - W2 colour to determine the k-correction we need to apply. This method allows us to measure the *WISE* W1 absolute magnitudes for our AGN sample.

4.4 GAMA IR AGN luminosity functions

To measure AGN luminosity functions with high completeness we first look at where the number of galaxies in the GAMA catalogue at z $<$ 0.35 peaks at in W1 magnitude. This is done by utilising a histogram which is shown in Figure 4.13. This figure shows that the peak of the galaxies population occurs at a magnitude of W1 = 18 mag. Thus we use a magnitude limit of W1 = 18 mag to measure our subsequent luminosity functions to maintain high completeness. A W1 uncertainty limit of $<$ 0.2 mag has been used throughout this chapter for all galaxies and AGNs, to prevent large photometric errors. W1 uncertainty as a function of W1 magnitude is displayed in Figure 4.14, showing the W1 magnitude limit that is used for our AGN sample. Note, these uncertainty measurements were provided by GAMA in their LAMBDAR photometry catalogues (Wright et al., 2016).

In order to investigate completeness further, we created a plot of W1 absolute magnitude as a function of W1 - W2 colour displayed in Figure 4.15. This figure shows that almost everything brighter than M_{W1} = -23.5 mag has WISE colour consistent with harbouring an AGN. This result implies that the bright end of the luminosity function does not depend on the details of our criteria.

We plot z $<$ 0.35 IR luminosity functions for multiple samples using the GAMA catalogues, this includes a luminosity function for all galaxies in GAMA, a luminosity function for AGNs selected with BPT and the Jarrett et al. (2011) WISE colour criteria, as well as a luminosity function for AGNs selected with BPT and more conservative Stern et al. (2012) and Assef et al. (2013) WISE colour criteria. A bin size of 0.5 mag is used. These luminosity functions are presented in Figure 4.16 and are all made with a W1 magnitude limit of 18 mag. The luminosity function of all GAMA galaxies (presented in the left panel of Figure 4.16) shows both the galaxy component and the AGN component at M_{W1} brighter than -24 clearly.

In the middle panel of Figure 4.16 we show the luminosity function measured using AGNs that have been selected with the BPT criterion and the less conservative Jarrett et al. (2011) WISE colour criteria. The right side panel of

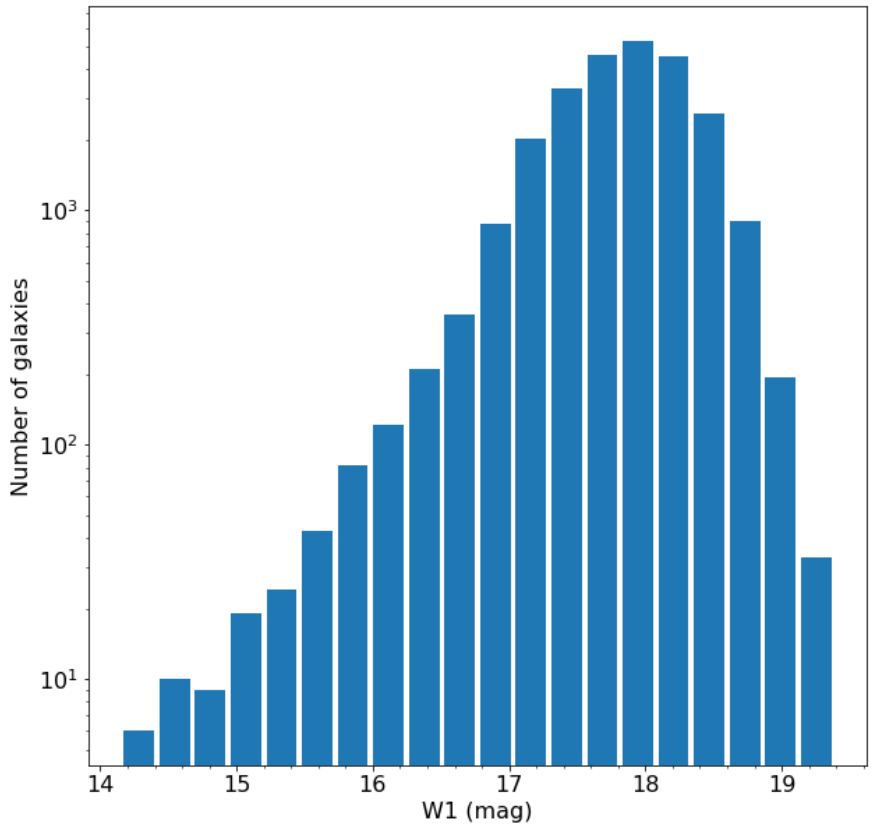

FIGURE 4.13: Histogram of GAMA galaxies in W1 at z < 0.35. The number of galaxies peaks at 18 mag and we use this magnitude limit to measure subsequent luminosity function to maintain good completeness.

Figure 4.16 displays the luminosity function measured with AGNs selected using the BPT criterion and the more conservative Stern et al. (2012) and Assef et al. (2013) WISE colour criteria. The turnover in the two AGN luminosity functions occurs at $M_{W1} \approx$ -23 mag and the shape of the bright end is similar qualitatively to that of the AGN component of the galaxy luminosity function. That being said however, as we've discussed in Section 4.2.3, the Jarrett et al. (2011) colour criteria can contain a large number of contaminants and this is also observed by Yao et al. (2020). Therefore we use the luminosity function created using the conservative Stern et al. (2012) and Assef et al. (2013) WISE colour criteria in order to select a pure sample of AGNs.

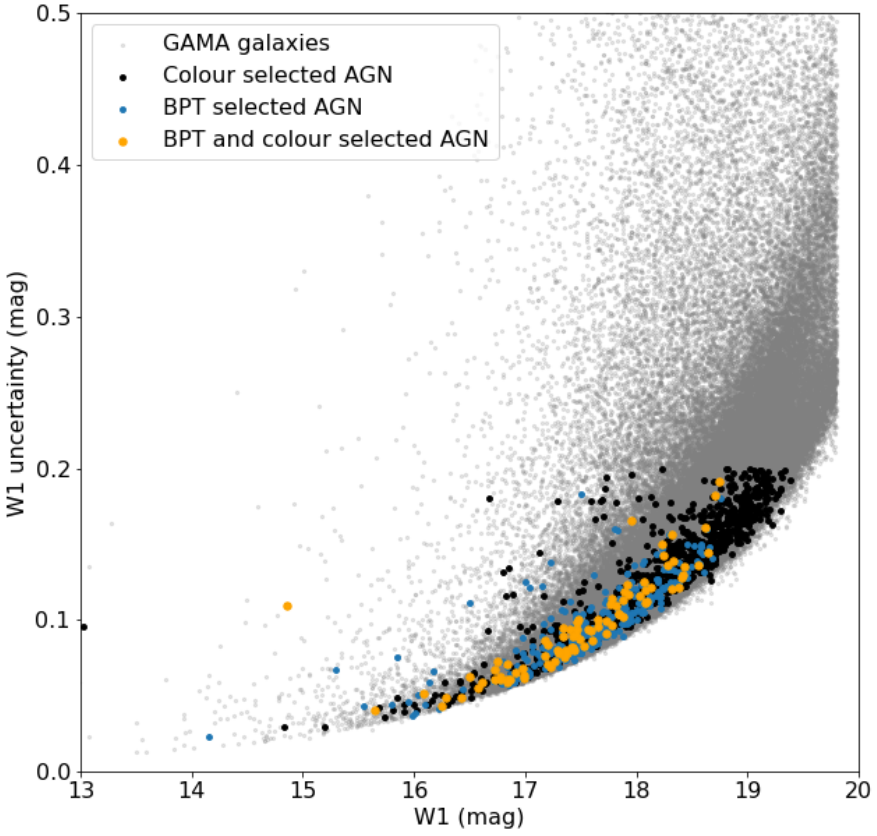

FIGURE 4.14: W1 magnitude as a function of W1 uncertainty. We use an uncertainty limit of $W1_{\text{uncertainty}} < 0.2$ for all galaxies and AGNs in our sample and this corresponds to a signal to noise of 5.4.

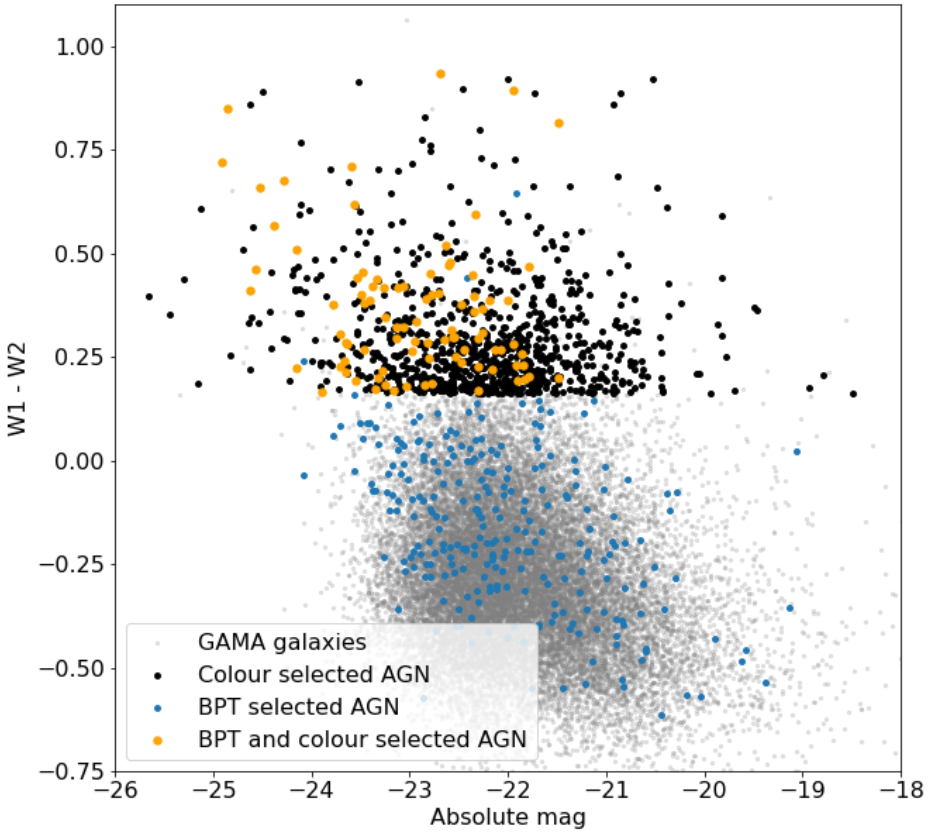

FIGURE 4.15: W1 absolute magnitude vs W1 - W2 colour. This figure shows that the majority of the objects brighter than M_{W1} = -23 are AGNs. And this implies that the bright end of the luminosity function does not depend on the details of our criteria.

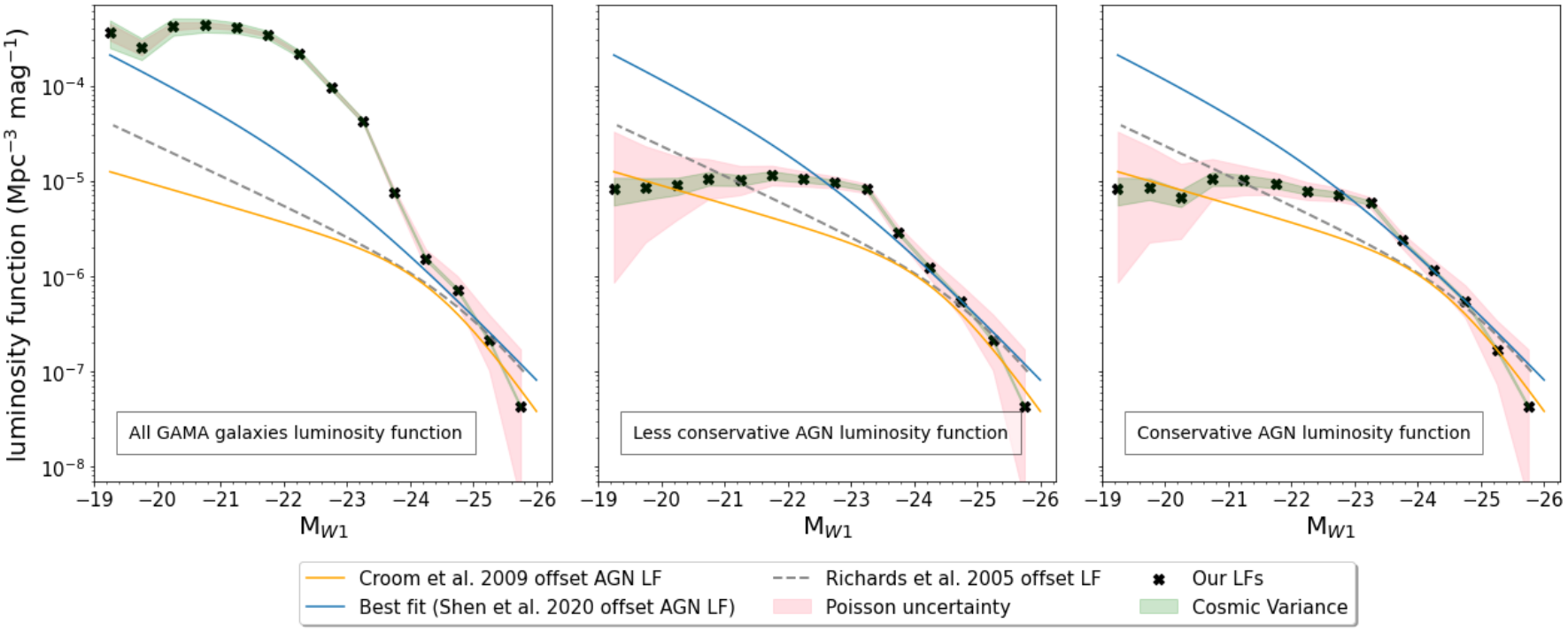

FIGURE 4.16: Luminosity functions of GAMA galaxies and AGNs all made with a W1 magnitude limit of 18 mag and magnitude bins of Δ 0.5 mag. Left: Luminosity function of all the galaxies in GAMA, with the bright AGN luminosity function being clearly visible at M_{W1} < -24 mag. Middle: AGN luminosity function made using the Jarrett et al. (2011) WISE colour criteria. Right: AGN luminosity function made with AGNs that meet the more conservative Stern et al. (2012) and Assef et al. (2013) WISE colour criteria. The luminosity function made with the more conservative criteria shows good agreement (within Poisson uncertainties) with the offset Shen et al. (2020) luminosity function at M_{W1} < -23 mag. We also compare our luminosity functions to that of Richards et al. (2005), Croom et al. (2009) and Shen et al. (2020) which have all been offset in M_{W1} to allow for comparison between our luminosity function and there's.

We also investigated the effects of different magnitude limits on our luminosity functions. Specifically for the galaxy luminosity function, using a magnitude limit of W1 = 19 mag showed a clear turnover at the lower brightness end at M_{W1} ≈ -21 mag which may be an indication of incompleteness. This turnover is not visible in the galaxy luminosity function made with a magnitude limit of 18 mag (presented in Figure 4.16), which is an indication that there is high completeness at W1 = 18 mag. We also investigate the effects of using different magnitude limits for the more conservative AGN luminosity function, including testing at W1 = 19 mag, 18.5 mag, 18 mag and 17.5 mag limits. This investigation showed the brighter end of the luminosity function (brighter than M_{W1} = -23 mag) is seemingly impervious to the magnitude limit used. This result was also implied by Figure 4.15, which shows that objects brighter than $M_{W1} = 23$ mag are AGNs.

Looking at the r - W1 SED colours of the Brown et al. (2019) AGNs, most of the AGN colours are bluer than 2.3 at z = 0.35, as the r band magnitude limit for GAMA is 19.8 mag, this colour corresponds to a W1 limit of 17.5 mag. Due to the unusual nature of some AGNs in the Brown et al. (2019) sample, a W1 limit of 17.5 is a more conservative limit and may be fainter than 17.5 mag. At a magnitude limit of W1 = 17.5 mag the data points at the brighter end shift, however the bins are within 1σ of that of the W1 = 18 mag limit luminosity function. That being the case, we use a magnitude limit of W1 = 18 mag to maintain relatively high completeness and large sample size. We illustrate our magnitude bins and the corresponding redshift limits in Figure 4.17 for our luminosity function using a line of constant magnitude of 18 mag. The specific limits of the magnitude bins, the number of AGNs in each bin and the volume of each bin are provided in Table 4.2.

In Figure 4.16, we present multiple luminosity functions from literature including Richards et al. (2005), Croom et al. (2009) and Shen et al. (2020) which have all been offset in M_{W1}. We use the offset luminosity function from Shen et al. (2020) to describe the brighter end of our luminosity function and this is displayed in Figure 4.16. The Shen et al. (2020) bolometric luminosity function is paramaterised by a double power law of the form;

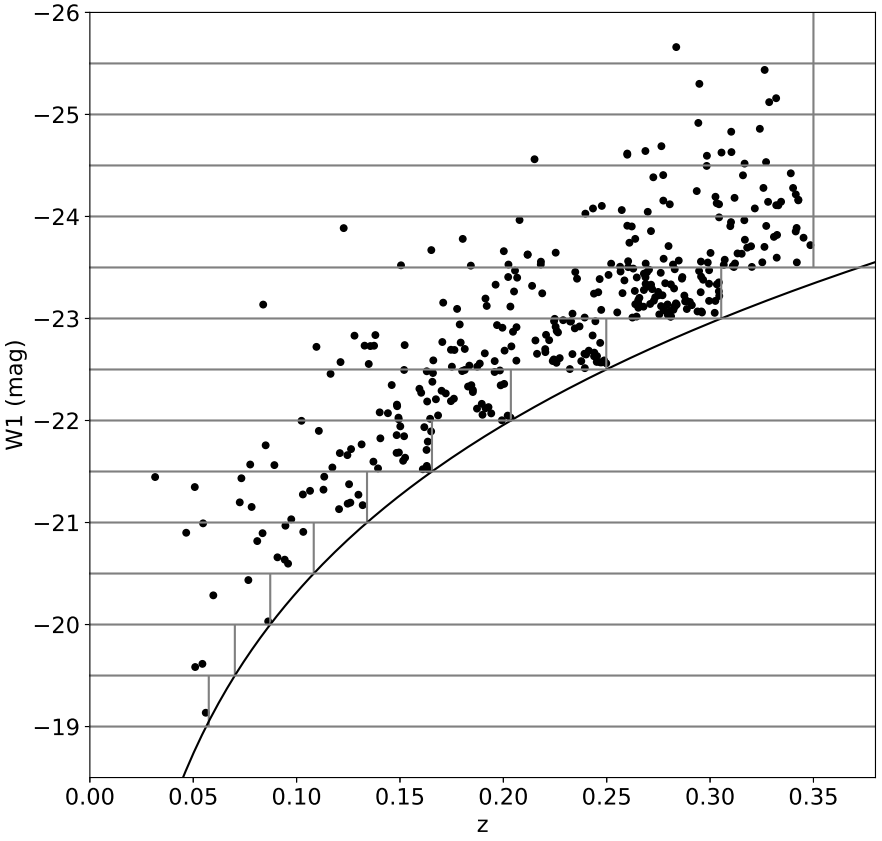

FIGURE 4.17: Absolute W1 magnitude vs redshift plot for our $z < 0.35$ AGN sample displaying our magnitude bins of 0.5 mag width as well as redshift limits for specific bins. The curve is a line of constant apparent magnitude of W1 = 18 mag, used to determine the redshift limits of each bin. Note that we use AGNs with $z < 0.35$ for our luminosity function so Hα remains in the optical wavelength range.

$$\phi_{bol}(L) = \frac{\phi_*}{(L/L_*)^{\gamma_1} + (L/L_*)^{\gamma_2}} \tag{4.7}$$

which expressed in magnitudes becomes;

$$\phi(M) = \frac{\phi_*''}{10^{0.4(\alpha+1)(M-M_*)} + 10^{0.4(\beta+1)(M-M_*)}} \tag{4.8}$$

where M_* is the break magnitude and α and β are the faint-end and bright-end slopes, respectively (Peterson, 1997; Croom et al., 2004). To go from the luminosity form of the double power law to the magnitude form we use; $\phi_*'' =$

$0.4\phi_*$, α = - (γ_1 +1) and β = - (γ_2 +1). The Shen et al. (2020) luminosity function is well constrained and it makes sense for us to move their function to fit our data, rather than to determine the different parameters required to fit a double power law luminosity function.

Using the Shen et al. (2020) luminosity function parameters as our initial parameters, we determine the M_* value that will fit the Shen et al. (2020) function to our luminosity functioned data at M_{W1} brighter than -23 mag. We do this by setting M_* as a free parameter in Curve_fit to determine the best M_* (colour offset) to describes our luminosity function. We find that an M_* = -22.77 $\pm$ 0.11 mag best describes our AGN luminosity function with a χ^2 = 11.76, and it is also within Poisson uncertainties as is evident by Figure 4.16 where we use M_* = -22.77 with the Shen et al. (2020) function. The bright end index of the luminosity function is -2.753; note we provide parameters for luminosity function from the literature in Table 1.1. It should be noted that we calculate Poisson uncertainties for our luminosity functions using the methods prescribed by Gehrels (1986). Cosmic variance uncertainties (sample variance) uncertainties are measured using Driver & Robotham (2010).

If we leave all parameters in the luminosity function free for data at M_{W1} < -23 mag we will have 7 data points to fit 4 different parameters. Attempting this fit produces a χ^2 = 1.35. Thus the parameters are not plausibly constrained, i.e. the location of the break could be anywhere and still produce a good fit to the data.

We thus express our IR $z < 0.35$ AGN luminosity function as;

$$\Phi(M_{W1}, z) = \frac{1.57 \times 10^{-5}}{10^{0.4(-1.812+1)(M_{W1}-M^*_{W1})} + 10^{0.4(-2.753+1)(M_{W1}-M^*_{W1})}} \tag{4.9}$$

where $M_* = M^*_{W1}$ = -22.77 $\pm$ 0.11 mag.

We also compare our luminosity functions to the optical luminosity functions from Richards et al. (2005) and Croom et al. (2009) presented in Figure 4.16. We offset the Richards et al. (2005) and Croom et al. (2009) functions in W1 absolute magnitude (M_{W1}) to aid in our comparison. Optical, X-ray and IR luminosity functions are measuring different things, by definition. It is thus not

TABLE 4.2: Our $z < 0.35$ quasar luminosity function with Poisson uncertainties, where the three GAMA regions cover 180 square degrees with a magnitude limit of W1 = 18 mag.

W1 range (mag)	Number of AGNs	Volume (Mpc^3)	Space density (Mpc^{-3} mag^{-1})	z range
-26.0 < M_{W1} < -25.5	1	4.76×10^7	$4.21 \pm 3.77 \times 10^{-8}$	z < 0.35
-25.5 < M_{W1} < -25.0	4	4.76×10^7	$1.68 \pm 1.34 \times 10^{-7}$	z < 0.35
-25.0 < M_{W1} < -24.5	13	4.76×10^7	$5.47 \pm 1.83 \times 10^{-7}$	z < 0.35
-24.5 < M_{W1} < -24.0	27	4.76×10^7	$1.14 \pm 0.33 \times 10^{-6}$	z < 0.35
-24.0 < M_{W1} < -23.5	56	4.76×10^7	$2.35 \pm 0.43 \times 10^{-6}$	z < 0.35
-23.5 < M_{W1} < -23.0	96	3.27×10^7	$5.87 \pm 0.65 \times 10^{-6}$	z < 0.31
-23.0 < M_{W1} < -22.5	67	1.87×10^7	$7.17 \pm 1.09 \times 10^{-6}$	z < 0.25
-22.5 < M_{W1} < -22.0	41	1.05×10^7	$7.82 \pm 1.50 \times 10^{-6}$	z < 0.20
-22.0 < M_{W1} < -21.5	27	5.79×10^6	$9.33 \pm 2.21 \times 10^{-6}$	z < 0.17
-21.5 < M_{W1} < -21.0	16	3.15×10^6	$1.02 \pm 0.37 \times 10^{-5}$	z < 0.13
-21.0 < M_{W1} < -20.5	9	1.63×10^6	$1.06 \pm 8.13 \times 10^{-5}$	z < 0.11
-20.5 < M_{W1} < -20.0	3	8.97×10^5	$6.69 \pm 6.31 \times 10^{-6}$	z < 0.09
-20.0 < M_{W1} < -19.5	2	4.71×10^5	$8.48 \pm 6.23 \times 10^{-6}$	z < 0.07
-19.5 < M_{W1} < -19.0	1	2.46×10^5	$8.14 \pm 15.97 \times 10^{-6}$	z < 0.06

surprising that the shapes of these luminosity functions differ from each other, i.e, the location of the break in the luminosity function varies between these different functions. It is also not surprising that how they are connected to the bolometric luminosity function differs. How faint you can push an AGN luminosity function in different bands depends on how bright the host galaxies are in that band relative to the AGN. We can see in our luminosity function figure that host galaxy contamination starts to make our luminosity function incomplete at magnitudes fainter than M_{W1} = -23 mag. In the optical, host galaxies are relatively bright, whereas in the X-ray host galaxies are relatively faint with IR falling somewhere in between and this is illustrated by our luminosity function we present in this work (Figure 4.16).

4.5 Accretion rate density

Our IR luminosity function, and our IR bolometric corrections measured in Chapter 3 can be used to measure the black hole accretion rate density for z < 0.35 (low redshift) AGNs using the methods described by Barger et al. (2001) and Shen et al. (2020). We use the 3 μm bolometric correction as it the closest in wavelength to the *WISE* W1 band, specifically we use the bolometric correction determined for our sample of AGNs which contained no host galaxy light and no PAHs. It should be noted that a motivation for using W1 to measure the

GAMA AGN luminosity function is that the 3 μm bolometric correction measured in Chapter 3 contained the least amount of 1σ vertical scatter of all IR bolometric corrections measured.

The bolometric luminosity function has the form;

$$\frac{\mathrm{d}n}{\mathrm{d}L_{bol}} = \frac{\mathrm{d}n}{\mathrm{d}M} \times \frac{\mathrm{d}M}{\mathrm{d}L} \times \frac{\mathrm{d}L}{\mathrm{d}L_{bol}} \tag{4.10}$$

where $\mathrm{d}n/\mathrm{d}M$ is our IR luminosity function (Equation 4.9) and $\mathrm{d}M/\mathrm{d}L$ is the derivative of magnitude to luminosity equation. The luminosity is related to the magnitude by;

$$L = \nu L_\nu = \nu \times 3631\mathrm{Jy} \times 4\pi \times (10\mathrm{pc})^2 \times 10^{-0.4M} = const \times 10^{-0.4M} \tag{4.11}$$

which is true if the absolute magnitude, M, is measured in AB magnitudes, and ν is the frequency of the *WISE* W1 band for which we have measured our luminosity function. Note when we refer to the luminosity, L, in this section, we are referring to νL_ν which is in units of erg s^{-1}, for convenience we denote it as just L. The derivative of the luminosity equation is then;

$$\frac{\mathrm{d}L}{\mathrm{d}M} = const \times \ln(10) \times -0.4 \times 10^{-\ln(10)\times 0.4\mathrm{M}} \tag{4.12}$$

and we use the inverse of this in Equation 4.10.

The 3 μm bolometric correction we measure in Chapter 3 is;

$$log(L_{bol}) = 0.05 + 1.02 log(\lambda L_\lambda) \tag{4.13}$$

and the derivative of this is;

$$\frac{\mathrm{d}L_{bol}}{\mathrm{d}L} = 10^{0.05} \times 1.02 \times L^{0.02} \tag{4.14}$$

and we use the inverse of this in Equation 4.10.

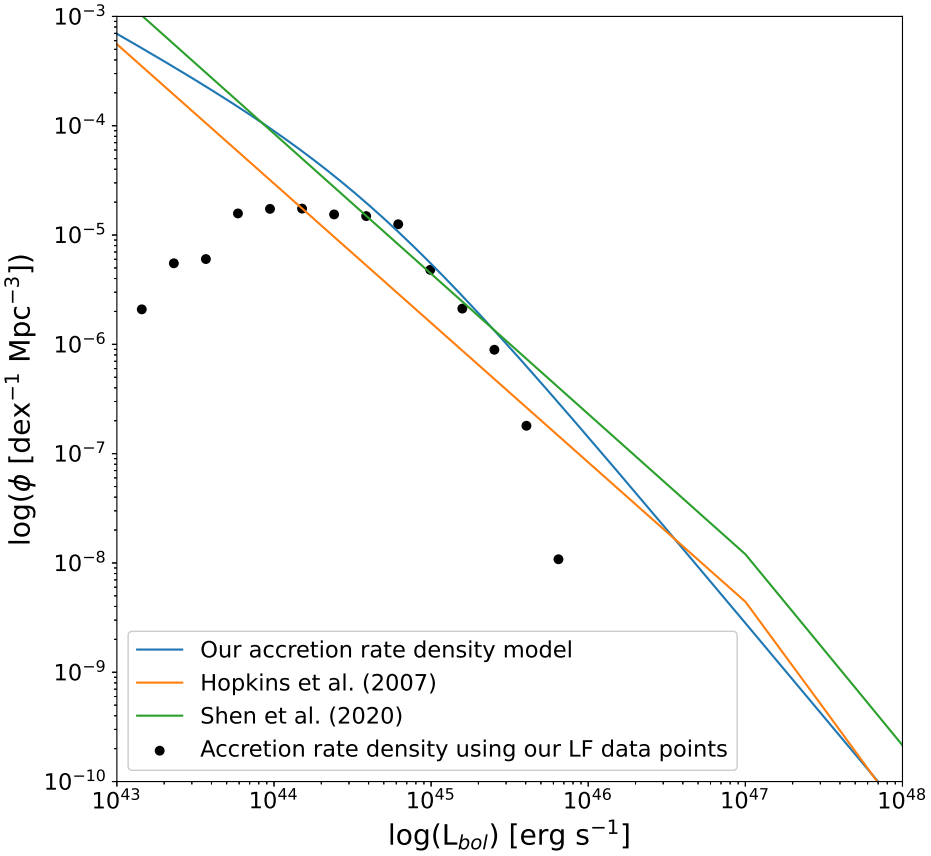

FIGURE 4.18: Our bolometric luminosity function determined using the $z < 0.35$ IR AGN luminosity function determined in this chapter and the 3 µm bolometric correction determined in Chapter 3. We also present the bolometric luminosity functions of Hopkins et al. (2007) and Shen et al. (2020).

We present our bolometric luminosity function in the form dL/dlog(L$_{bol}$), which can be measured using;

$$\frac{\mathrm{d}n}{\mathrm{dlog}(L_{bol})} = \frac{\mathrm{d}n}{\mathrm{d}L_{bol}} \times \frac{\mathrm{d}L_{bol}}{\mathrm{dlog}(L_{bol})} \tag{4.15}$$

and we display our bolometric luminosity function in Figure 4.18, along with the bolometric luminosity functions from Hopkins et al. (2007) and Shen et al. (2020). We convert our bolometric luminosity function into this form to allow for comparison with the quasar bolometric luminosity function from Shen et al. (2020), which is parameterised in this form.

The accretion rate history can thus be determined by integrating over our quasar bolometric luminosity function using;

$$\dot{\rho} = \int \frac{\mathrm{d}n}{\mathrm{d}L_{bol}} L_{bol}\ \mathrm{d}L_{bol} \tag{4.16}$$

where $\dot{\rho}$ is the bolometric luminosity density. We then use Equation 1.2 from Barger et al. (2001) to measure the accretion rate density, where our measured $\dot{\rho}$ is L_{bol} in units of erg s^{-1} Mpc^{-3}. The resulting accretion rate density is in units of $M_\odot$ Gyr^{-1} Mpc^{-3}.

We first measure the accretion rate density for an absolute magnitude range of -35 < M_{W1} (mag) < -20, which is comparable to the magnitude range our IR luminosity function is applicable for. The resulting low redshift ($z < 0.35$, mean z of the sample = 0.24) accretion rate density we measure is 2.85 $\times$ 10^{-6} $M_\odot$ yr^{-1} Mpc^{-3}. Cosmic variance uncertainties in GAMA for z < 0.35 are 3.8%. The uncertainty in our fit of M^*_{W1} is 0.11 mag and we believe that this is our dominant source of random error. Therefore our accretion rate density with uncertainties is 2.85 $\pm$ 0.36 $\times$ 10^{-6} $M_\odot$ yr^{-1} Mpc^{-3}.

This accretion rate density is comparable, however lower than, the accretion rate densities measured by Barger et al. (2001) which are displayed in Figure 1.14. The accretion rate density for $z = 0.25$ measured by Barger et al. (2001) is $\approx$ 5 $\times$ 10^{-6} $M_\odot$ yr^{-1} Mpc^{-3}, and increases with redshift following a $(1 + z)^3$ trend. For a redshift of $z = 0.35$, they measure an accretion rate density of $\approx$ 7 $\times$ 10^{-6} $M_\odot$ yr^{-1} Mpc^{-3}. These measurements of accretion rate density are comparable to that of Marconi et al. (2004) who measure an accretion rate density of $\approx$ 9 $\times$ 10^{-6} $M_\odot$ yr^{-1} Mpc^{-3} at $z \approx 0.35$. Merloni (2004) determine the accretion rate density using a number of luminosity functions, including Elvis et al. (1994), Boyle et al. (2000) and Marconi et al. (2004), calculating a range of 6 - 10 $\times$ 10^{-6} $M_\odot$ yr^{-1} Mpc^{-3}.

While our random errors are small, our systematic uncertainties are far larger. If we integrate down to M_{W1} = -10 mag, we measure an accretion rate density of 5.61 $\times$ 10^{-6} $M_\odot$ yr^{-1} Mpc^{-3}, but if we integrate down to M_{W1} = -20 mag the accretion rate density is 2.85 $\times$ 10^{-6} $M_\odot$ yr^{-1} Mpc^{-3}. This highlights that

the extrapolation at the faint end of the luminosity function is critical for the inferred accretion rate density. As the brighter end of the bolometric luminosity function declines steeply, shown in Figure 4.18, extrapolating to brighter luminosities does not have a significant impact on the accretion rate density. If we use a different bolometric correction, such as the 3 μm Runnoe et al. (2012a) bolometric correction (remeasured using Hyperfit), we measure an accretion rate density of 2.26 $\times$ 10^{-6} $M_{\odot}$ yr^{-1} Mpc^{-3} for -35 $<$ M_{W1} (mag) $<$ -20, which is 21 % lower than our original accretion rate density estimated using the same magnitude range. We therefore note that when utilising our work, to be aware that systematic errors are the main source of error in our accretion rate density.

4.6 Conclusions

In this chapter we measured the IR luminosity function of AGNs in the GAMA survey at $z < 0.35$ AGNs using IR colour and optical emission line ratios. These selection methods allow us to select AGNs that are both obscured and unobscured and is different from previous AGN luminosity functions that select AGNs using the optical, UV or soft X-ray which preferentially select unobscured AGNs. We used this sample to determine if there is a population of obscured AGNs which are optically faint and Compton thick. We find a population of WISE AGNs that have the emission lines of star forming galaxies but also have a broadened Hα component implying the presence of an AGN. These AGNs are LIRGs and historically they have been attributed largely to star forming but the WISE colours and the (sub-dominant) broad emission lines imply that they are powered by AGNs (i.e. Yao et al., 2020). An example of this is G09_Y1_GS1_242 which appears to have narrow lines where Hα is stronger than [NII], however there appears to be a broadened component. This AGN has an FWHM of 45.72 $\pm$ 2.42 Å($\approx$ 2000 km/s), as the star forming lines in this AGN dominate, it may be miss-classified by other surveys. These AGNs are LIRGs and historically they have been attributed largely to star forming but the WISE colours imply that they are powered by AGNs as is found also by Yao et al. (2020).

Of the 1199 quasars in our sample, the two most luminous type 2 quasars (M_{W1} < -24 mag) are GAMA J143124.72+012724.3 and GAMA J084359.39-004423.0 (shown in Figure 4.11). We find that luminous type 2 AGNs makes up ≈ 4 % of our sample of M_{W1} < -24 mag AGNs upon visual inspection of AGN spectra with the remainder being unobscured AGNs.

We modeled our luminosity function (at M_{W1} < -23 mag) by offsetting the Shen et al. (2020) bolometric luminosity function in W1 absolute magnitude to determine the break magnitude (M_*) which best fits our data. When we try to do fitting for more than one parameter (such as ϕ_*'' and M_*), the luminosity function is poorly constrained. This is because we do not have enough data to constrain the break and faint end index of the luminosity function. As the Shen et al. (2020) function is well constrained, offsetting it provides a good fit to our data.

When we compare our luminosity function to that of Richards et al. (2005) and Croom et al. (2009) optical luminosity functions, we find that the break in our IR luminosity function occurs at lower luminosities (M_{W1} = -23 mag). This is to be expected as our luminosity functions, by definition, are looking at different things, thus the break in the luminosity function occurs at different locations. The brightness of host galaxy light varies between the optical, X-ray and IR. We can see from Figure 4.16, that host galaxy contamination starts to effect our luminosity function at magnitudes fainter than M_{W1} = -23 mag. The host galaxy is relatively bright in the optical, relatively faint in the X-ray and IR sits in between this.

Using our luminosity function and the 3 μm bolometric correction from Chapter 3, we measured the low redshift accretion rate density. For a magnitude range of -35 < M_{W1} (mag) < -20 we measure an accretion rate density of 2.85 ± 0.36 × 10^{-6} $M_\odot$ yr^{-1} Mpc^{-3}. We find that the main source of uncertainty is systematic rather than random. When extrapolating to lower luminosities we see an increase in the accretion rate density and this is due to the shape of the bolometric luminosity function. Extrapolating to brighter luminosities does not impact the accretion rate density as the slope of the bolometric luminosity function decreases

at brighter luminosities. Investigation of using different bolometric corrections also showed that variation in measurements were larger than random errors.

Chapter 5

Summary and Conclusions

In this thesis we used a combination of infrared (IR) photometry, optical photometry and optical emission line measurements to select obscured, unobscured and variable AGNs from galaxy surveys **to determine whether there are populations of AGNs that have been missed by previous AGN surveys and to improve measurements of the cosmic accretion history**. The space density of AGNs has previously been measured using optical, X-ray and radio wavelengths. The issue with these wavelengths is, however, that they suffer from significant and well-known selection effects. Optical and UV light is obscured by dust, radio emission is poorly correlated with bolometric luminosity and the soft X-ray is sensitive to electron attenuation. Therefore, using these wavelengths may lead to an underestimate of the true space density of AGNs.

The bolometric luminosities of individual AGNs and the AGN bolometric luminosity function provide a measure of the accretion history of SMBHs, but require a means to estimate bolometric luminosities from the available data. We have measured bolometric corrections for X-ray, UV/optical and IR wavelengths using the Brown et al. (2019) AGN SEDs. Using the GAMA survey we determined the IR luminosity function of $z < 0.35$ AGNs which were selected using IR colour and emission line ratios in order to select both obscured and unobscured AGNs. We then used our IR bolometric correction and IR luminosity function to measure the accretion rate density at $z < 0.35$.

In this chapter we look back at the aims presented in Chapter 1 and summarise our key conclusions below:

- We conducted a systematic search for $z < 0.04$ CLAGNs that may have changed spectral type in the past decade using SkyMapper, Pan-STARRs and *WISE* to search the entire sky. We identified AGNs in these surveys using the Véron-Cetty & Véron (2010) catalogue of AGNs. To select CLAGN candidates we used optical colours as a proxy for Hα equivalent widths and selected red Seyfert type 1s and blue Seyfert type 2s. We also used variability of optical and MIR fluxes to select CLAGN candidates, where a change may indicate a change in spectral type. We then inspected the archival spectra of the our CLAGN candidates for any indication of changes in the spectra. To confirm the change in spectral type, we used the WiFeS instrument on the 2.3m telescope at Siding Spring to obtain new spectra of our candidates.

  We identified two new CLAGNs; NGC 1346 and MASX J20075129-1108346, and also recovered Mrk 915 and Mrk 609. We also estimate a lower limit of ≈ 18 CLAGNs at $z < 0.04$, including the two new CLAGNs identified in this work, 10 previously known CLAGNs and as many as 6 CLAGNs that may have been missed by our selection methods. We note that this number of CLAGNs is too small to significantly effect the current quasar luminosity function.

- We have measured UV/optical, X-ray and IR bolometric corrections using the Brown et al. (2019) AGN SEDs, which are the best available AGN SEDs at this time. Our AGN SED sample contained a variety of different AGNs including obscured and unobscured. To measure the bolometric luminosity, we integrated over a wider integration range than much of recent literature; from 24 μm to 8 keV (Nemmen & Brotherton, 2010; Runnoe et al., 2012a,b; Krawczyk et al., 2013). Our integration range included IR to X-ray wavelengths; this is because different AGNs have different emission mechanisms at different wavelengths, therefore it is necessary to use a wide integration range to measure an accurate bolometric luminosity.

Our main sample of AGN SEDs consisted of 27 AGNs, which all had X-ray spectra data. From this main sample we measured bolometric corrections for a number of different subsets and these were: a sample of AGNs that did not have PAHs (22 AGNs), a sample of AGNs that contained no host galaxy contributions or PAHs (16 AGNs) as well as for the full Brown et al. (2019) AGN SED sample (27 AGNs).

Host galaxy contamination was determined for the 8 AGNs in our sample that had archival H-band host galaxy fractions from McLeod & Rieke (1994a) and McLeod & Rieke (1994b). We used the same methods as Shang et al. (2011) to do this. In the IR 1.5 µm, 2 µm and 3 µm had decreases in monochromatic luminosity with the largest decrease seen at 1.5 µm of 0.01 - 0.22 dex. In the optical/UV we see a decrease in monochromatic magnitude at 5100 Å of 0.00 - 0.17 dex. The reason we see significant changes in luminosity at these wavelengths is due to the H-band peaking at 1.65 µm. When host galaxy fractions and HST galaxy imaging is unavailable, another option is to explore SED AGN and host galaxy decomposition. Pacifici et al. (in prep,. private communication) use different SED-fitting codes to illustrate that it is difficult to measure host galaxy light, especially when the host fraction exceeds 20 %. As SED-fitting codes are highly dependent on the priors used and the library of AGN models used, measurements of galaxy decomposition can vary greatly across different codes.

In order to compare our bolometric corrections to that of Runnoe et al. (2012a) and Runnoe et al. (2012b), we remeasured their bolometric corrections (which were measured using minimising-χ^2) using Hyper-fit, a maximum-likelihood fitting technique which fits data points in D-dimensions (Robotham & Obreschkow, 2015). We found that the gradients measured using minimised-χ^2 were between 0.69 - 0.98 compared to gradients measured using Hyperfit, which were between 0.89 - 1.07.

Our bolometric luminosities spanned a wider wavelength range than the literature ($\log(L_{bol}) \approx 42.5$ - 47.5 erg s^{-1}). We found that our bolometric

luminosities and IR monochromatic luminosities were almost directly proportional, which is different to what is seen in the literature. The Runnoe et al. (2012b) bolometric corrections have a wider range of gradients from 0.89 to 1.07. The discrepancy from the literature may be caused in part by our sample covering a wider luminosity range than literature, and in part by the differences in fitting methods used to determine the relationship between bolometric luminosity and monochromatic luminosity.

The 1σ scatter of our IR bolometric corrections increased with increasing wavelength. We recorded the highest scatter for our 24 µm bolometric correction of 0.49 dex and a 1σ scatter of 0.23 dex for our 1.5 µm, 2 µm and 3 µm bolometric corrections. These measurements suggest that our bolometric corrections at shorter wavelengths are more reliable that those at longer wavelengths.

- We measured the $z < 0.35$ IR luminosity function for the GAMA survey (Hopkins, 2008; Cluver et al., 2014), using a combination of IR colour and optical emission line selection criteria to search for AGNs that may not be identified by UV-optical and X-ray surveys. The advantage of using the GAMA survey was that GAMA provides spectra for most of their objects, which allowed us to verify our AGNs by visually inspecting spectra. GAMA also furnishes us with spectroscopic redshifts for all the likely quasar host galaxies of $z < 0.35$ AGNs, where this redshift limit corresponds to the redshift limit at which optical emission lines appear in the GAMA optical spectra.

  We selected our AGN sample using emission line ratios, *WISE* colour and the Véron-Cetty & Véron (2010) AGN catalogue. Using these criteria we were able to select 1199 $z < 0.35$ obscured and unobscured AGNs. We found that the colour selected AGNs were the most luminous AGNs in our sample, including broad line AGNs. The IR colour selection picked many galaxies with narrow lines that are consistent with star formation, but that often have broadening of Hα and Hβ indicating the presence of an underlying AGN. The BPT selected AGNs were lower luminosity narrow-line AGNs.

We find a population of WISE AGNs that have emission lines of star forming galaxies but also have a broadened Hα component, which implies the presence of an AGN. An example of this is G09_Y1_GS1_242, which had an FWHM of 45.72 $\pm$ 2.42 Å($\approx$ 2000 km/s). This AGN had narrow lines where Hα was stronger than [NII]. As the star forming region in these AGNs dominate, they may be miss-classified by other surveys. Historically these AGNs have been attributed to star forming, however these are LIRGs and the WISE colours imply that they are powered by AGNs.

We use a magnitude limit of W1 = 18 mag to determine our luminosity function (displayed in Figure 4.16). This limit was used as this magnitude is where the peak of the GAMA galaxy population is (this is displayed in Figure 4.13). Investigations of using different magnitude limits, including W1 = 19 mag, 18.5 mag, 18 mag and 17.5 mag showed that the bright end of our luminosity function (M_{W1} < -23 mag) remained seemingly impervious to the magnitude limit used. Investigations were also made into using different magnitude limits to determine a galaxy luminosity function for GAMA. This investigation showed that the galaxy luminosity function turns over when a limit of 19 mag or 18.5 mag is used, which is an indication of incompleteness. This was not seen in the galaxy luminosity function determined using a 18 magnitude limit, where the lower luminosity end looks flat. It should also be noted that this galaxy luminosity function displayed an AGN component at brighter magnitudes (M_{W1} < -24 mag).

We modelled our luminosity function by offsetting the Shen et al. (2020) bolometric luminosity function in W1 absolute magnitude. When all parameters were left free for our data points at M_{W1} < -23 mag, we are fitting seven data points to a model with four free parameters, and we get a χ^2 = 1.35. Thus, the parameters are not plausible constrained, i.e. the location of the break could be anywhere and still produce a good fit to the data. We used the parameters of Shen et al. (2020) and kept M_* as a free parameter. We found that an M^*_{W1} = -22.77 $\pm$ 0.11 mag provided the best fit to our data.

Optical, X-ray and IR luminosity functions are, by definition, measuring different things. It is therefore not surprising that we see that the shapes of the optical luminosity functions from Richards et al. (2005) and Croom et al. (2009) differ from our IR luminosity function, i.e. the position of the break in luminosity function varies. The faint luminosity limits of an AGN luminosity function in different bands depends on the brightness of the host galaxy in that band, relative to the AGN. In our luminosity function, we can see that host contamination starts to make our luminosity function incomplete at magnitudes fainter than M_{W1} = -23 mag.

We then used our IR luminosity function measured in W1 (3.4 μm) and the 3 μm bolometric correction measured in Chapter 3 to measure the low redshift ($z < 0.35$) accretion rate density. For a magnitude range of -35 < M_{W1} (mag) < -20 we measured an accretion rate density of 2.85 ± 0.36 × 10^{-6} $M_{\odot}$ yr^{-1} Mpc^{-3}. Cosmic variance uncertainties in GAMA for z < 0.35 are 3.83 %. The uncertainty in M^{*}_{W1} = 0.11 mag and we believe that this is our dominant source of random uncertainty.

Our systematic errors for the accretion rate density are far larger than our random errors. Investigation of extrapolating to lower luminosities highlighted that extrapolation at the faint of the luminosity function does play a critical role on the accretion rate density measured. This is because the lower luminosity end of the bolometric luminosity function tends upwards. If a different bolometric correction is used (such as the 3 μm Runnoe et al. (2012a) bolometric correction) we measure an accretion rate density which is 21 % lower than our original accretion rate density. We therefore note that when utilizing our work, to be aware that systematic errors are the main source of error in our accretion rate density.

Future work

Our survey for CLAGNs had limited follow up of candidates, particularly in the northern hemisphere, so an obvious next step is more comprehensive spectroscopic follow-up and observations. Long term monitoring of our CLAGN

candidates is also a logical next step using such tools as the Gravitational-wave Optical Transient Observer (GOTO, Dyer et al., 2020). GOTO and similar telescopes will allow for constant monitoring of CLAGN candidates and the ability to observe changes in light curves of candidates, which may indicate changes in spectral type.

Chapter 2 represents an exploration of trying to select as many CLAGNs as possible in the nearby Universe in a systematic fashion. The selection criteria we adopted worked to varying degrees, which we explained in detail in Section 2.3. Our work showed that previously available spectra were a critical point for this study and better utilization of the quantification of this spectra (e.g., measurements of emission line widths) could lead to more efficient selection of CLAGNs and the quantification of these changes. **A clear next step would be to create a pipeline that can do two component emission line fits on heterogeneous spectra.** Using this pipeline we can make accurate and consistent measurements from archival spectra that comes from various sources obtained from different telescopes. This pipeline will be particularly valuable as we are often comparing spectra that are observed sometimes decades apart where the quality spectra that are $\gtrapprox$ 20 years old may not be ideal.

Intermediate AGN types are often classified qualitatively (e.g. Osterbrock, 1977), which has the potential for the classifications of spectra to vary across literature. We have classified the spectra qualitatively using the descriptions that have been provided by Osterbrock (1977) and Osterbrock (1981). The classification were performed by several researchers (4 researchers including Micheal Brown, Michelle Cluver, Christian Wolf and myself). We did this by individually classifying spectra using the Osterbrock (1977) and Osterbrock (1981) descriptions and then comparing our classifications to see if there was agreement or disagreement between all researchers. When there was a disagreement with classifications we discussed as a group why a certain classification was appropriate and then reclassified the spectra in question until we all agreed. We classified both the newly obtained WiFeS spectra as well as the spectra from literature to maintain consistency.

A key component of this next step, and thus pipeline, should be providing a quantitative classification scheme for intermediate spectral types based on the widths of the emission lines that it measures. The classification on the basis of width will need careful consideration, and a potential avenue to consider is using archival spectra and the classifications given to them by previous studies to decide a quantitative means of classifying AGN types. This avenue will first require that the pipeline measure widths of the archival spectra and matching that to the classification given by the literature. Combining this together this pipeline can become extremely important for the field.

We wish to expand the luminosity range, wavelength range and sample size of obscured and unobscured AGNs used for bolometric corrections. In Chapter 3 of this thesis, we measured bolometric corrections for X-ray, optical/UV and IR wavelengths using AGN SEDs from Brown et al. (2019) which contained both obscured and unobscured AGNs. We found that luminosity range was wider than much of the literature, where we had AGNs with bolometric luminosities that extended out to lower luminosities (Elvis et al., 1994; Nemmen & Brotherton, 2010; Runnoe et al., 2012a,b). Thus, we found that while our bolometric corrections overlapped those from the literature at higher luminosities, the slope of our bolometric correction was steeper than the literature as a result of our lower luminosity AGNs. Thus the bolometric corrections can be improved by using a larger, more diverse AGN sample that cover a wide luminosity range and include both obscured and unobscured AGNs.

We would also like to investigate the effects of using a wider wavelength range for integration to measure bolometric corrections, particularly when using a variety of different AGN types. The two major outliers in our bolometric corrections were Mrk 421 and Mrk 231, which are obscured optically red objects. These AGNs produce the majority of their energy at wavelengths beyond 24 μm. We investigated the effects on the bolometric luminosity if we integrated from 500 μm - 8 keV for these two AGNs, finding that doing so measured a bolometric luminosity that was closer to the line of best fit for our bolometric correction with an increase in $\log(L_{bol})$ of 0.46 dex. This result

showed that the choice of integration range can effect the measured bolometric correction, which is particularly true for AGNs types with different emission mechanisms.

Another avenue for future work pertaining to our bolometric corrections is to measure host galaxy contributions for all AGNs in our sample and then remove this fraction before measuring bolometric corrections. In Chapter 3, we explained that we only have archival H-band host galaxy fractions for 8 AGNs in our sample obtained from McLeod & Rieke (1994a) and McLeod & Rieke (1994b) and we removed AGNs from our sample that contained a H-band galaxy fraction of > 0.20. Runnoe et al. (2012a) and Runnoe et al. (2012b) also measured H-band host galaxy fractions, where they used archival fractions when available, and measuring H-band host galaxy fractions from HST observations for their remaining AGNs. These fractions were then used to remove host galaxy contributions from their SEDs by using the elliptical galaxy template for NGC 0584 from Dale et al. (2007), where NGC 0584 is scaled using the H-band host galaxy contribution fraction and the resulting spectrum is removed from the SED. A possibility is taking the same approach to remove host galaxy contribution for the SEDs used in Chapter 3.

Are there overlooked quasars in the SDSS and 6dFGS? Using *WISE* colours, we selected both obscured and unobscured AGNs from the GAMA catalogue with both clear and low level broad lines. IR selection picked many galaxies with narrow lines consistent with star formation, but with broadened Hα and Hβ, confirming that they were AGNs. We also saw that galaxies in the star forming region of the *WISE* colour diagram showed no evidence of broadening in Hα emission.

By using *WISE*, we can select obscured and unobscured AGNs in the SDSS and 6dFGS catalogues with the aim of looking for AGNs with low level broadening, which may have been overlooked by previous AGN surveys. The presence of these AGNs could also have implications for star formation in AGNs. There may be potentially significant populations of Seyferts in SDSS and 6dFGS where the flux is dominated by the star forming host, which may have been missed by surveys that only perform single component line fits.

We now have a large number of relatively luminous AGNs where the optical is dominated by the host while the IR is dominated by the AGN. We thus may expect to see IR variability for these objects, as not all IR emission from AGNs is from the torus (Kishimoto et al., 2013; Kool et al., 2020). Apart from confirming the AGN origin of the IR, this may also identify changing look AGNs for optical follow-up.

Bibliography

Abazajian K., Adelman-McCarthy J. K., Agüeros M. A., Allam S. S., et al. 2004, Astronomical Journal, 128, 502

Afanasiev V. L., Popović L. Č., Shapovalova A. I., Borisov N. V., Ilić D., 2014, Monthly Notices of the RAS, 440, 519

Agís-González B., Bagnulo S., Hutsemékers D., Montesinos B., Miniutti G., Sanfrutos M., 2017, in Arribas S., Alonso-Herrero A., Figueras F., Hernández-Monteagudo C., Sánchez-Lavega A., Pérez-Hoyos S., eds, Highlights on Spanish Astrophysics IX. pp 275–275

Alam S., et al., 2015, The Astrophysical Journal Supplement Series, 219, 12

Alexandroff R., et al., 2013, Monthly Notices of the Royal Astronomical Society, 435, 3306

Amanullah R., et al., 2010, The Astrophysical Journal, 716, 712

Antonucci R., 1993, Annual Review of Astronomy and Astrophysics, 31, 473

Antonucci R. R. J., Cohen R. D., 1983, Astrophysical Journal, 271, 564

Assef R. J., et al., 2013, The Astrophysical Journal, 772, 26

Baldry I. K., Glazebrook K., Brinkmann J., Ivezić Ž., Lupton R. H., Nichol R. C., Szalay A. S., 2004, The Astrophysical Journal, 600, 681

Baldry I. K., et al., 2014, Monthly Notices of the RAS, 441, 2440

Baldwin J. A., Phillips M. M., Terlevich R., 1981, Publications of the Astronomical Society of the Pacific, 93, 5

Banerji M., Alaghband-Zadeh S., Hewett P. C., McMahon R. G., 2015, Monthly Notices of the Royal Astronomical Society, 447, 3368

Barger A. J., Cowie L. L., Bautz M. W., Brandt W. N., Garmire G. P., Hornschemeier A. E., Ivison R. J., Owen F. N., 2001, Astronomical Journal, 122, 2177

Barger A. J., Cowie L. L., Mushotzky R. F., Yang Y., Wang W. H., Steffen A. T., Capak P., 2005, Astronomical Journal, 129, 578

Barth A. J., et al., 2015, Astrophysical Journal Supplement, 217, 26

Barvainis R., 1987, The Astrophysical Journal, 320, 537

Beckmann V., Shrader C., 2012, in Proceedings of "An INTEGRAL view of the high-energy sky (the first 10 years)" - 9th INTEGRAL Workshop and celebration of the 10th anniversary of the launch (INTEGRAL 2012). p. 69 (arXiv:1302.1397)

Begelman M. C., 1989, in Osterbrock D. E., Miller J. S., eds, 134th Symposium of the International Astronomical Union Vol. 134, Active Galactic Nuclei. p. 141

Bell E. F., McIntosh D. H., Katz N., Weinberg M. D., 2003, Astrophysical Journal Supplement, 149, 289

Bell E. F., et al., 2004, The Astrophysical Journal, 608, 752

Bennett C. L., et al., 2003, The Astrophysical Journal Supplement Series, 148, 1

Bergvall N., Johansson L., Olofsson K., 1986, Astronomy & Astrophysics, 166, 92

Bianchi S., La Franca F., Matt G., Guainazzi M., Jimenez Bailón E., Longinotti A. L., Nicastro F., Pentericci L., 2008, Monthly Notices of the Royal Astronomical Society, 389, L52

Bianchi S., Guainazzi M., Matt G., Fonseca Bonilla N., Ponti G., 2009, Astronomy & Astrophysics, 495, 421

Birnboim Y., Dekel A., Neistein E., 2007, Monthly Notices of the RAS, 380, 339

Blumenthal G. R., Faber S. M., Primack J. R., Rees M. J., 1984, Nature, 311, 517

Bouchet P., Garcia-Marin M., Lagage P.-O., et al. 2015, Astronomical Society of the Pacific, 127, 1

Boyle B. J., Shanks T., Peterson B. A., 1988, Monthly Notices of the RAS, 235, 935

Boyle B. J., Shanks T., Croom S. M., Smith R. J., Miller L., Loaring N., Heymans C., 2000, Monthly Notices of the RAS, 317, 1014

Braito V., Reeves J. N., Bianchi S., Nardini E., Piconcelli E., 2017, Astronomy & Astrophysics, 600, A135

Brammer G. B., et al., 2009, The Astrophysical Journal, 706, L173

Brightman M., et al., 2017, The Astrophysical Journal, 844, 10

Brodie J. P., et al., 2014, The Astrophysical Journal, 796, 52

Bromm V., Yoshida N., 2011, Annual Review of Astronomy and Astrophysics, 49, 373

Brough S., et al., 2017, The Astrophysical Journal, 844, 59

Brown M. J. I., et al., 2006, The Astrophysical Journal, 638, 88

Brown M. J. I., et al., 2014, Astrophysical Journal Supplement, 212, 18

Brown M. J. I., Duncan K. J., Landt H., Kirk M., Ricci C., Kamraj N., Salvato M., Ananna T., 2019, Monthly Notices of the RAS, 489, 3351

Burtscher L., et al., 2013, Astronomy & Astrophysics, 558, A149

Burtscher L., et al., 2015, Astronomy & Astrophysics, 578, A47

Buttiglione S., Capetti A., Celotti A., Axon D. J., Chiaberge M., Macchetto F. D., Sparks W. B., 2009, Astronomy & Astrophysics, 495, 1033

Calzetti D., 2001, The Publications of the Astronomical Society of the Pacific, 113, 1449

Canelo C. M., Friaça A. C. S., Sales D. A., Pastoriza M. G., Ruschel-Dutra D., 2018, Monthly Notices of the Royal Astronomical Society, 475, 3746

Cappellari M., Copin Y., 2003, Monthly Notice of the Royal Astronomical Society, 342, 345

Cappellari M., et al., 2007, Monthly Notices of the Royal Astronomical Society, 379, 418

Cardelli J. A., Clayton G. C., Mathis J. S., 1989, The Astrophysical Journal, 345, 245

Cen R., 2011, The Astrophysical Journal, 741, 99

Chambers K. C., et al., 2019, arXiv e-prints, p. arXiv:1612.05560

Chartas G., Brandt W. N., Gallagher S. C., 2003, The Astrophysical Journal, 595, 85

Childress M. J., Vogt F. P. A., Nielsen J., Sharp R. G., 2014, Astrophysics and Space Science, 349, 617

Cluver M. E., et al., 2014, The Astrophysical Journal, 782, 90

Cluver M. E., et al., 2020, The Astrophysical Journal, 898, 20

Cole S., Lacey C. G., Baugh C. M., Frenk C. S., 2000, Monthly Notices of the RAS, 319, 168

Colless M., et al., 2001, Monthly Notices of the RAS, 328, 1039

Comastri A., 2004, in Barger A. J., ed., Astrophysics and Space Science Library Vol. 308, Supermassive Black Holes in the Distant Universe. p. 245 (arXiv:astro-ph/0403693), doi:10.1007/978-1-4020-2471-9_8

Condon J. J., 1992, Annual review of astronomy and astrophysics, 30, 575

Cowie L. L., Songaila A., Barger A. J., 1999, The Astronomical Journal, 118, 603

Coziol R., Demers S., Barneoud R., Pena M., 1997, Astronomical Journal, 113, 1548

Croom S. M., Smith R. J., Boyle B. J., Shanks T., Loaring N. S., Miller L., Lewis I. J., 2001, Monthly Notices of the Royal Astronomical Society, 322, L29

Croom S. M., Smith R. J., Boyle B. J., Shanks T., Miller L., Outram P. J., Loaring N. S., 2004, Monthly Notices of the Royal Astronomical Society, 349, 1397

Croom S. M., et al., 2009, Monthly Notices of the Royal Astronomical Society, 399, 1755

Croton D. J., et al., 2006, Monthly Notices of the RAS, 365, 11

Cruz-Gonzalez I., Carrasco L., Serrano A., Guichard J., Dultzin-Hacyan D., Bisiacchi G. F., 1994, Astrophysical Journal Supplement, 94, 47

Dahari O., De Robertis M. M., 1988, Astrophysical Journal Supplement, 67, 249

Dale D. A., et al., 2007, The Astrophysical Journal, 655, 863

Davies L. J. M., Robotham A. S. G., Driver S. P., et al. 2015, Monthly Notices of the Royal Astronomical Society, 452, 616

Davis S. W., El-Abd S., 2019, The Astrophysical Journal, 874, 23

De Lucia G., Blaizot J., 2007, Monthly Notices of the RAS, 375, 2

Denney K. D., et al., 2014, The Astrophysical Journal, 796, 134

Dexter J., Agol E., 2011, The Astrophysical Journal, 727, L24

Dopita M. A., Sutherland R. S., 2003, Astrophysics of the diffuse universe. Springer

Dopita M., et al., 2010, Astrophysics and Space Science, 327, 245

Dopita M. A., et al., 2014, Astronomy & Astrophysics, 566, A41

Dopita M. A., et al., 2015, Astrophysical Journal Supplement, 217, 12

Dressler A., Oemler A., Gladders M. G., Bai L., Rigby J. R., Poggianti B. M., 2009, Astrophysical Journal Letters, 699, L130

Driver S. P., Robotham A. S. G., 2010, Monthly Notices of the Royal Astronomical Society, 407, 2131

Driver S. P., et al., 2011, Monthly Notices of the RAS, 413, 971

Dunlop J. S., Peacock J. A., 1990, Monthly Notices of the RAS, 247, 19

Duras F., et al., 2020, Astronomy & Astrophysics, 636, A73

Durret F., 1994, Astronomy and Astrophysics, Supplementary Series, 105, 57

Dyer M. J., et al., 2020, in Society of Photo-Optical Instrumentation Engineers (SPIE) Conference Series. p. 114457G (arXiv:2012.02685), doi:10.1117/12.2561008

Eckart M. E., McGreer I. D., Stern D., Harrison F. A., Helfand D. J., 2010, The Astrophysical Journal, 708, 584

Eisenstein D. J., et al., 2011, Astronomical Journal, 142, 72

Elvis M., et al., 1994, The Astrophysical Journal, Supplement, 95, 1

Emsellem E., et al., 2007, Monthly Notices of the Royal Astronomical Society, 379, 401

Eracleous M., Halpern J. P., 2001, Astrophysical Journal, 554, 240

Fabian A. C., 1999a, Proceedings of the National Academy of Science, 96, 4749

Fabian A. C., 1999b, Monthly Notices of the RAS, 308, L39

Fabian A. C., 2012, Annual Review of Astronomy and Astrophysics, 50, 455

Falcón-Barroso J., et al., 2006, Monthly Notices of the Royal Astronomical Society, 369, 529

Fan X., et al., 2001, Astronomical Journal, 121, 54

Flewelling H. A., et al., 2020, The Astrophysical Journal Supplement Series, 251, 7

Florez J., et al., 2021, Monthly Notices of the RAS, 508, 762

Fogarty L. M. R., et al., 2014, Monthly Notices of the Royal Astronomical Society, 443, 485

Fontanot F., Cristiani S., Monaco P., Nonino M., Vanzella E., Brandt W. N., Grazian A., Mao J., 2007, Astronomy & Astrophysics, 461, 39

Fosbury R. A. E., et al., 1982, Monthly Notices of the RAS, 201, 991

Fraquelli H. A., Storchi-Bergmann T., Binette L., 2000, The Astrophysical Journal, 532, 867

Gaia Collaboration et al., 2016, Astronomy & Astrophysics, 595, A1

Gavazzi G., Consolandi G., Dotti M., Fossati M., Savorgnan G., Gualandi R., Bruni I., 2013, Astronomy & Astrophysics, 558, A68

Gehrels N., 1986, The Astrophysical Journal, 303, 336

Georgantopoulos I., Papadakis I., Zezas A., Ward M. J., 2004, The Astrophysical Journal, 614, 634

George I. M., Fabian A. C., 1991, Monthly Notices of the Royal Astronomical Society, 249, 352

Gezari S., et al., 2017, The Astrophysical Journal, 835, 144

Giacconi R., et al., 2002, The Astrophysical Journal Supplement Series, 139, 369

Giannuzzo E. M., Stirpe G. M., 1996, Astronomy & Astrophysics, 314, 419

Gilli R., Maiolino R., Marconi A., Risaliti G., Dadina M., Weaver K. A., Colbert E. J. M., 2000, Astronomy & Astrophysics, 355, 485

Gitti M., Brighenti F., McNamara B. R., 2012, Advances in Astronomy, 2012, 950641

Gonçalves A. C., Véron-Cetty M. P., Véron P., 1999, Astronomy and Astrophysics, Supplementary Series, 135, 437

Goodrich R. W., 1989, The Astrophysical Journal, 340, 190

Goodrich R. W., 1995, The Astrophysical Journal, 440, 141

Goodrich R. W., Osterbrock D. E., 1983, The Astrophysical Journal, 269, 416

Gordon Y. A., et al., 2017, Monthly Notices of the RAS, 465, 2671

Greenawalt B., Walterbos R. A. M., Braun R., 1997, The Astrophysical Journal, 483, 666

Greene J. E., Ho L. C., 2007, The Astrophysical Journal, 667, 131

Gregory S. A., Tifft W. G., Cocke W. J., 1991, Astronomical Journal, 102, 1977

Grogin N. A., Geller M. J., 2000, Astronomical Journal, 119, 32

Grogin N. A., et al., 2011, The Astrophysical Journal Supplement, 197, 35

Guo H., et al., 2016, Astrophysical Journal, 826, 186

Han Y., Dai B., Wang B., Zhang F., Han Z., 2012, Monthly Notices of the RAS, 423, 464

Hasinger G., et al., 2001, Astronomy and Astrophysics, 365, L45

Hasinger G., Miyaji T., Schmidt M., 2005, Astronomy & Astrophysics, 441, 417

Hewett P. C., Foltz C. B., Chaffee F. H., 1993, Astrophysical Journal Letters, 406, L43

Ho L., 1999, in Chakrabarti S. K., ed., Astrophysics and Space Science Library Vol. 234, Observational Evidence for the Black Holes in the Universe. p. 157, doi:10.1007/978-94-011-4750-7_11

Ho L. C., Kim M., 2009, Astrophysical Journal Supplement, 184, 398

Ho L. C., Filippenko A. V., Sargent W. L., 1995, Astrophysical Journal Supplement, 98, 477

Hogg D. W., 1999, arXiv e-prints, pp astro–ph/9905116

Hogg D. W., Baldry I. K., Blanton M. R., Eisenstein D. J., 2002, Cornell University Library

Hogg D. W., et al., 2004, Astrophysical Journal Letters, 601, L29

Hon W. J., Webster R., Wolf C., 2020, Monthly Notices of the Royal Astronomical Society, 497, 192

Hönig S. F., et al., 2013, The Astrophysical Journal, 771, 87

Hopkins P. F., 2008, in Kodama T., Yamada T., Aoki K., eds, Astronomical Society of the Pacific Conference Series Vol. 399, Panoramic Views of Galaxy Formation and Evolution. p. 405

Hopkins P. F., Hernquist L., Cox T. J., Di Matteo T., Robertson B., Springel V., 2006, Astrophysical Journal Supplement, 163, 1

Hopkins P. F., Bundy K., Hernquist L., Ellis R. S., 2007, The Astrophysical Journal, 659, 976

Hopkins A. M., et al., 2013, Monthly Notices of the Royal Astronomical Society, 430, 2047

Houck J. R., et al., 2005, The Astrophysical Journal Letters, 622, L105

Hubble E. P., 1926, The Astrophysical Journal, 64, 321

Hubble E. P., 1936, Realm of the Nebulae. Yale University Press

Hubble E., Humason M. L., 1931, The Astrophysical Journal, 74, 43

Hunt M. P., Steidel C. C., Adelberger K. L., Shapley A. E., 2004, The Astrophysical Journal, 605, 625

Ishibashi W., Fabian A. C., Canning R. E. A., 2013, Monthly Notices of the Royal Astronomical Society, 431, 2350

Jaffe W., et al., 2004, Nature, 429, 47

Jansen R. A., Fabricant D., Franx M., Caldwell N., 2000, Astrophysical Journal Supplement, 126, 331

Jarrett T. H., et al., 2011, The Astrophysical Journal, 735, 112

Jeong H., et al., 2019, The Astrophysical Journal, 875, 60

Jones D. H., et al., 2009, Monthly Notices of the Royal Astronomical Society, 399, 683

Kauffmann G., Heckman T. M., White S. D. M., et al. 2003, Monthly Notices of the Royal Astronomical Society, 341, 33

Kelly B. C., Sobolewska M., Siemiginowska A., 2011, in American Astronomical Society Meeting Abstracts #217. p. 142.33

Kennicutt Robert C. J., 1992, Astrophysical Journal Supplement, 79, 255

Kennicutt R. C. J., Keel W. C., 1984, Astrophysical Journal Letters, 279, L5

Kereš D., Katz N., Weinberg D. H., Davé R., 2005, Monthly Notices of the RAS, 363, 2

Kewley L. J., Heisler C. A., Dopita M. A., Lumsden S., 2001a, Astrophysical Journal Supplement, 132, 37

Kewley L. J., Dopita M. A., Sutherland R. S., et al. 2001b, The Astrophysical Journal, 556, 121

Khachikian E. Y., Weedman D. W., 1971, Astrophysical Journal Letters, 164, L109

Khachikian E. Y., Asatrian N. S., Burenkov A. N., 2011, Astrophysics, 54, 26

Kim D. C., Sanders D. B., Veilleux S., Mazzarella J. M., Soifer B. T., 1995, Astrophysical Journal Supplement, 98, 129

Kishimoto M., et al., 2013, The Astrophysical Journal Letters, 775, L36

Koekemoer A. M., et al., 2011, The Astrophysical Journal Supplement, 197, 36

Kokubo M., 2015, Monthly Notices of the Royal Astronomical Society, 449, 94

Kollatschny W., Fricke K. J., 1987, Astronomy & Astrophysics, 183, 9

Komatsu E., et al., 2011, Astrophysical Journal Supplement, 192, 18

Koo D. C., Kron R. G., 1988, The Astrophysical Journal, 325, 92

Kool E. C., et al., 2020, Monthly Notices of the Royal Astronomical Society, 498, 2167

Korista K., Baldwin J., Ferland G., Verner D., 1997, Astrophysical Journal Supplement, 108, 401

Koss M., et al., 2017, The Astrophysical Journal, 850, 74

Krajnović D., et al., 2011, Monthly Notices of the Royal Astronomical Society, 414, 2923

Krawczyk C. M., Richards G. T., Mehta S. S., Vogeley M. S., Gallagher S. C., Leighly K. M., Ross N. P., Schneider D. P., 2013, The Astrophysical Journal Supplement Series, 206, 4

Kubota A., Done C., 2018, Monthly Notices of the Royal Astronomical Society, 480, 1247

Kulkarni G., Worseck G., Hennawi J. F., 2019, Monthly Notices of the Royal Astronomical Society, 488, 1035

LaMassa S. M., et al., 2015, Astrophysical Journal, 800, 144

Landt H., Bentz M. C., Ward M. J., Elvis M., Peterson B. M., Korista K. T., Karovska M., 2008, Astrophysical Journal Supplement, 174, 282

Landt H., Ward M. J., Peterson B. M., Bentz M. C., Elvis M., Korista K. T., Karovska M., 2013, Monthly Notices of the RAS, 432, 113

Leger A., Puget J. L., 1984, Astronomy and Astrophysics, 500, 279

Lilly S. J., Le Fevre O., Hammer F., Crampton D., 1996, Astrophysical Journal Letters, 460, L1

Lira P., Johnson R. A., Lawrence A., Cid Fernand es R., 2007, Monthly Notices of the RAS, 382, 1552

MacLeod C. L., et al., 2010, The Astrophysical Journal, 721, 1014

MacLeod C. L., Ross N. P., Lawrence A., Goad M., Horne K., Burgett W., Chambers K. C., 2016, Monthly Notices of the Royal Astronomical Society, 457, 389

MacLeod C. L., et al., 2019, The Astrophysical Journal, 874, 8

Magorrian J., et al., 1998, Astronomical Journal, 115, 2285

Maia M. A. G., da Costa L. N., Willmer C., Pellegrini P. S., Rite C., 1987, Astronomical Journal, 93, 546

Maia M. A. G., Suzuki J. A., da Costa L. N., Willmer C. N. A., Rite C., 1996, Astronomy and Astrophysics, Supplementary Series, 117, 487

Mainzer A., et al., 2014, The Astrophysical Journal, 792, 30

Marchese E., Braito V., Della Ceca R., Caccianiga A., Severgnini P., 2012, Monthly Notices of the Royal Astronomical Society, 421, 1803

Marconi A., Risaliti G., Gilli R., Hunt L. K., Maiolino R., Salvati M., 2004, Monthly Notices of the Royal Astronomical Society, 351, 169

Marin F., Porquet D., Goosmann R. W., Dovčiak M., Muleri F., Grosso N., Karas V., 2013, Monthly Notices of the RAS, 436, 1615

Markwardt C. B., 2009, in Bohlender D. A., Durand D., Dowler P., eds, Astronomical Society of the Pacific Conference Series Vol. 411, Astronomical Data Analysis Software and Systems XVIII. p. 251 (arXiv:0902.2850)

Márquez I., et al., 2004, Astronomy & Astrophysics, 416, 475

Masetti N., et al., 2006a, Astronomy & Astrophysics, 449, 1139

Masetti N., et al., 2006b, Astronomy & Astrophysics, 459, 21

Mason R. E., 2015, Planetary Space Science, 116, 97

Massaro E., Giommi P., Leto C., Marchegiani P., Maselli A., Perri M., Piranomonte S., Sclavi S., 2009, Astronomy & Astrophysics, 495, 691

Mathews W. G., Ferland G. J., 1987, The Astrophysical Journal, 323, 456

Mathez G., 1978, Astronomy and Astrophysics, 68, 17

McElroy R. E., et al., 2016, Astronomy & Astrophysics, 593, L8

McGreer I. D., et al., 2013, The Astrophysical Journal, 768, 105

McLeod K. K., Rieke G. H., 1994a, The Astrophysical Journal, 420, 58

McLeod K. K., Rieke G. H., 1994b, The Astrophysical Journal, 431, 137

Meiksin A., 2005, Monthly Notices of the RAS, 356, 596

Meisenheimer K., et al., 2007, Astronomy & Astrophysics, 471, 453

Menci N., 2006, Mem. S.A.It., 77, 670

Merloni A., 2004, Monthly Notices of the Royal Astronomical Society, 353, 1035

Merloni A., et al., 2015, Monthly Notices of the RAS, 452, 69

Miley G., 1980, Annual review of astronomy and astrophysics, 18, 165

Mocz P., Fabian A. C., Blundell K. M., 2013, Monthly Notices of the RAS, 432, 3381

Moran E. C., Halpern J. P., Helfand D. J., 1994, Astrophysical Journal Letters, 433, L65

Moran E. C., Halpern J. P., Helfand D. J., 1996, Astrophysical Journal, Supplement, 106, 341

Morris S. L., Ward M. J., 1988, Monthly Notices of the RAS, 230, 639

Moustakas J., Kennicutt Jr. R. C., 2006, Astrophysical Journal Supplement, 164, 81

Mutch S. J., Croton D. J., Poole G. B., 2013, Monthly Notices of the Royal Astronomical Society, 435, 2445

Nagayama T., 2012, African Skies, 16, 98

Nemmen R. S., Brotherton M. S., 2010, Monthly Notices of the Royal Astronomical Society, 408, 1598

Netzer H., 2015, Annual Review of Astron and Astrophys, 53, 365

Niida M., et al., 2020, The Astrophysical Journal, 904, 89

Noda H., Done C., 2018, Monthly Notices of the Royal Astronomical Society,

Oknyansky V. L., et al., 2017, Monthly Notices of the Royal Astronomical Society, 467, 1496

Oknyansky V. L., Lipunov V. M., Gorbovskoy E. S., Winkler H., van Wyk F., Tsygankov S., Buckley D. A. H., 2018, The Astronomer's Telegram, 11915

Onken C. A., Wolf C., Bian F., Fan X., Hon W. J., Raithel D., Tisserand P., 2021, arXiv e-prints, p. arXiv:2105.12215

Osterbrock D. E., 1977, The Astrophysical Journal, 215, 733

Osterbrock D. E., 1978, Physica Scripta, 17, 137

Osterbrock D. E., 1981, The Astrophysics Journal, 249, 462

Osterbrock D. E., 1985, The Publications of the Astronomical Society of the Pacific, 97, 25

Osterbrock D. E., 1989, Astrophysics of gaseous nebulae and active galactic nuclei. University Science Books

Osterbrock D. E., Koski A. T., 1976, Monthly Notices of the Royal Astronomical Society, 176, 61P

Owen F. N., Ledlow M. J., Keel W. C., 1996, Astronomical Journal, 111, 53

Padovani P., 2016, The Astronomy and Astrophysics Review, 24, 13

Padovani P., et al., 2017, Astronomy and Astrophysics Reviews, 25, 2

Paliya V. S., Marcotulli L., Ajello M., Joshi M., Sahayanathan S., Rao A. R., Hartmann D., 2017, The Astrophysical Journal, 851, 33

Parkash V., Brown M. J. I., Jarrett T. H., Fraser-McKelvie A., Cluver M. E., 2019, Monthly Notices of the RAS, 485, 3169

Pennell A., Runnoe J. C., Brotherton M. S., 2017, Monthly Notices of the Royal Astronomical Society, 468, 1433

Penston M. V., Perez E., 1984, Monthly Notices of the Royal Astronomical Society, 211, 33P

Peterson B. M., 1997, An Introduction to Active Galactic Nuclei. Cambridge University Press

Phillips M. M., Charles P. A., Baldwin J. A., 1983, The Astrophysical Journal, 266, 485

Piconcelli E., Jimenez-Bailón E., Guainazzi M., Schartel N., Rodríguez-Pascual P. M., Santos-Lleó M., 2005, Astronomy & Astrophysics, 432, 15

Pietsch W., Bischoff K., Boller T., Doebereiner S., Kollatschny W., Zimmermann H. U., 1998, Astronomy & Astrophysics, 333, 48

Pimbblet K. A., Drinkwater M. J., Hawkrigg M. C., 2004, Monthly Notices of the Royal Astronomical Society, 354, L61

Pimbblet K. A., Shabala S. S., Haines C. P., Fraser-McKelvie A., Floyd D. J. E., 2013, Monthly Notices of the RAS, 429, 1827

Pracy M. B., Owers M. S., Zwaan M., Couch W., Kuntschner H., Croom S. M., Sadler E. M., 2014, Monthly Notices of the Royal Astronomical Society, 443, 388

Ramos Almeida C., Martínez González M. J., Asensio Ramos A., Acosta-Pulido J. A., Hönig S. F., Alonso-Herrero A., Tadhunter C. N., González-Martín O., 2016, Monthly Notices of the RAS, 461, 1387

Raouf M., et al., 2021, The Astrophysical Journal, 908, 123

Rees M. J., 1984, Annual Review of Astronomy and Astrophysics, 22, 471

Reichardt C., Jimenez R., Heavens A. F., 2001, Monthly Notices of the RAS, 327, 849

Reimers D., Koehler T., Wisotzki L., 1996, Astronomy and Astrophysics, Supplementary Series, 115, 235

Retana-Montenegro E., Röttgering H. J. A., 2020, Astronomy & Astrophysics, 636, A12

Reunanen J., Kotilainen J. K., Prieto M. A., 2003, Monthly Notices of the RAS, 343, 192

Richards G. T., et al., 2005, Monthly Notices of the RAS, 360, 839

Richards G. T., et al., 2006a, Astronomical Journal, 131, 2766

Richards G. T., et al., 2006b, The Astrophysical Journal, Supplement, 166, 470

Riffel R., Rodríguez-Ardila A., Pastoriza M. G., 2006, Astronomy & Astrophysics, 457, 61

Robotham A. S. G., Obreschkow D., 2015, Publications of the Astronomical Society of Australia, 32, e033

Ross N. P., et al., 2013, The Astrophysical Journal, 773, 14

Ross N. P., et al., 2018, Monthly Notices of the Royal Astronomical Society

Rossa J., van der Marel R. P., Böker T., Gerssen J., Ho L. C., Rix H.-W., Shields J. C., Walcher C.-J., 2006, Astronomical Journal, 132, 1074

Roussel H., Sauvage M., Vigroux L., Bosma A., 2001, Astronomy & Astrophysics, 372, 427

Ruan J. J., et al., 2016, The Astrophysical Journal, 826, 188

Rudy R. J., Cohen R. D., Ake T. B., 1988, The Astrophysical Journal, 332, 172

Runnoe J. C., Brotherton M. S., Shang Z., 2012a, Monthly Notices of the Royal Astronomical Society, 422, 478

Runnoe J. C., Brotherton M. S., Shang Z., 2012b, Monthly Notices of the RAS, 426, 2677

Runnoe J. C., et al., 2016, Monthly Notices of the Royal Astronomical Society, 455, 1691

Sabbadin F., Cappellaro E., Salvadori L., Turatto M., 1989, Astrophysical Journal Letters, 347, L5

Sadler E. M., Jenkins C. R., Kotanyi C. G., 1989, Monthly Notices of the RAS, 240, 591

Sanders D. B., et al., 2007, The Astrophysical Journal Supplement Series, 172, 86

Scarpa R., Falomo R., Pesce J. E., 1996, Astronomy and Astrophysics, Supplementary Series, 116, 295

Scarsi L., 1997, in Data Analysis in Astronomy. pp 65–78

Schawinski K., et al., 2014, Monthly Notices of the RAS, 440, 889

Schmidt M., 1963, Nature, 197, 1040

Schmidt M., 1968, The Astrophysical Journal, 151, 393

Schmidt M., Green R. F., 1983, The Astrophysical Journal, 269, 352

Schmidt M., Schneider D. P., Gunn J. E., 1995, Astronomical Journal, 110, 68

Schmidt E. O., Ferreiro D., Vega Neme L., Oio G. A., 2016, Astronomy & Astrophysics, 596, A95

Schneider D. P., Hall P. B., Richards G. T., Strauss M. A., Vanden Berk D. E., others 2007, Astronomical Journal, 134, 102

Senarath M. R., Brown M. J. I., Cluver M. E., Jarrett T. H., Ross N. P., 2019, Research Notes of the AAS, 3, 62

Senarath M. R., et al., 2021, Monthly Notices of the Royal Astronomical Society, 503, 2583

Seyfert C. K., 1943, Astrophysical Journal, 97, 28

Shang Z., et al., 2005, The Astrophysical Journal, 619, 41

Shang Z., et al., 2011, Astrophysical Journal Supplement, 196, 2

Shapovalova A. I., Popović L. Č., Burenkov A. N., Chavushyan V. H., Ilić D., Kovačević A., Bochkarev N. G., León-Tavares J., 2010, Astronomy and Astrophysics, 509, A106

Shapovalova A. I., et al., 2019, Monthly Notices of the RAS, 485, 4790

Shappee B. J., et al., 2014, The Astrophysical Journal, 788, 48

Shen X., Hopkins P. F., Faucher-Giguère C.-A., Alexander D. M., Richards G. T., Ross N. P., Hickox R. C., 2020, Monthly Notices of the RAS, 495, 3252

Shinozaki K., Miyaji T., Ishisaki Y., Ueda Y., Ogasaka Y., 2006, Astronomical Journal, 131, 2843

Siemiginowska A., Czerny B., Kostyunin V., 1996, The Astrophysical Journal, 458, 491

Silk J., Rees M. J., 1998, Astronomy & Astrophysics, 331, L1

Singal J., George J., Gerber A., 2016, The Astrophysical Journal, 831, 60

Springel V., et al., 2005, Nature, 435, 629

Springel V., Frenk C. S., White S. D. M., 2006, Nature, 440, 1137

Stepanian J. A., Chavushyan V. H., Carrasco L., Valdés J. R., Mújica R. M., Tovmassian H. M., Ayvazyan V. T., 2002, Astronomical Journal, 124, 1283

Stern D., et al., 2012, The Astrophysical Journal, 753, 30

Stern D., et al., 2018, The Astrophysical Journal, 864, 27

Stoklasová I., Ferruit P., Emsellem E., Jungwiert B., Pécontal E., Sánchez S. F., 2009, Astronomy & Astrophysics, 500, 1287

Storchi Bergmann T., 2015, in Ziegler B. L., Combes F., Dannerbauer H., Verdugo M., eds, Proceedings of the International Astronomical Union Vol. 309, Galaxies in 3D across the Universe. pp 190–195 (arXiv:1410.6241), doi:10.1017/S1743921314009648

Storchi Bergmann T., Bica E., Pastoriza M. G., 1990, Monthly Notices of the RAS, 245, 749

Storchi-Bergmann T., Baldwin J. A., Wilson A. S., 1993, Astrophysical Journal Letters, 410, L11

Strateva I., et al., 2001, Astronomical Journal, 122, 1861

Tabor G., Binney J., 1993, Monthly Notices of the RAS, 263, 323

Tanimoto A., Ueda Y., Kawamuro T., Ricci C., Awaki H., Terashima Y., 2018, The Astrophysical Journal, 853, 146

Taylor E. N., et al., 2014, Monthly Notices of the Royal Astronomical Society, 446, 2144

Thomas A. D., et al., 2017, Astrophysical Journal Supplement, 232, 11

Tinsley B. M., 1968, The Astrophysical Journal, 151, 547

Tohline J. E., Osterbrock D. E., 1976, Astrophysical Journal, Letters, 210, L117

Toomre A., Toomre J., 1972, The Astrophysical Journal, 178, 623

Trakhtenbrot B., et al., 2019, The Astrophysical Journal, 883, 94

Tran H. D., Osterbrock D. E., Martel A., 1992a, Astronomical Journal, 104, 2072

Tran H. D., Miller J. S., Kay L. E., 1992b, The Astrophysical Journal, 397, 452

Trippe M. L., Crenshaw D. M., Deo R., Dietrich M., 2008, The Astronomical Journal, 135, 2048

Trippe M. L., Crenshaw D. M., Deo R. P., Dietrich M., Kraemer S. B., Rafter S. E., Turner T. J., 2010, The Astrophysical Journal, 725, 1749

Tsalmantza P., et al., 2009, Astronomy & Astrophysics, 504, 1071

Tuccillo D., González-Serrano J. I., Benn C. R., 2015, Monthly Notices of the Royal Astronomical Society, 449, 2818

Tully R. B., Mould J. R., Aaronson M., 1982, The Astrophysical Journal, 257, 527

Ueda Y., Akiyama M., Ohta K., Miyaji T., 2003, The Astrophysical Journal, 598, 886

Veron-Cetty M. P., Veron P., 1986a, Astronomy and Astrophysics, Supplementary Series, 65, 241

Veron-Cetty M. P., Veron P., 1986b, Astronomy and Astrophysics, Supplementary Series, 66, 335

Véron-Cetty M.-P., Véron P., 2003, Astronomy & Astrophysics, 412, 399

Véron-Cetty M.-P., Véron P., 2010, Astronomy & Astrophysics, 518, A10

Von Benda-Beckmann A. M., Müller V., 2008, Monthly Notices of the Royal Astronomical Society, 384, 1189

Wang L., et al., 2013, Monthly Notices of the RAS, 431, 648

Wang S., Liu J., Qiu Y., Bai Y., Yang H., Guo J., Zhang P., 2016, Astrophysical Journal Supplement, 224, 40

Warren S. J., Hewett P. C., Osmer P. S., 1994, The Astrophysical Journal, 421, 412

Weedman D. W., 1976, Quarterly Journal of the Royal Astronomical Society, 17, 227

Wei J. Y., Xu D. W., Dong X. Y., Hu J. Y., 1999, Astronomy and Astrophysics, Supplementary Series, 139, 575

Weijmans A.-M., et al., 2014, Monthly Notices of the Royal Astronomical Society, 444, 3340

Wen X.-Q., Wu H., Zhu Y.-N., et al. 2014, Monthly Notices of the Royal Astronomical Society, 438, 97

Werner M. W., et al., 2004, Astrophysical Journal Supplement, 154, 1

White S. D. M., Frenk C. S., 1991, The Astrophysical Journal, 379, 52

White S. D. M., Rees M. J., 1978, Monthly Notices of the RAS, 183, 341

White R. L., et al., 2000, Astrophysical Journal Supplement, 126, 133

Wilson G., Cowie L. L., Barger A. J., Burke D. J., 2002, The Astronomical Journal, 124, 1258

Winkler H., 1992, Monthly Notices of the RAS, 257, 677

Wolf C., Wisotzki L., Borch A., Dye S., Kleinheinrich M., Meisenheimer K., 2003, Astronomy & Astrophysics, 408, 499

Wolf C., et al., 2018, Publications of the Astronomical Society of Australia, 35, e010

Wright E. L., et al., 2010, Astronomical Journal, 140, 1868

Wright A. H., et al., 2016, Monthly Notices of the RAS, 460, 765

Wyder T. K., et al., 2007, Astrophysical Journal Supplement, 173, 293

Wyithe J. S. B., Loeb A., 2003, The Astrophysical Journal, 595, 614

Yang X., Mo H. J., van den Bosch F. C., Zhang Y., Han J., 2012, The Astrophysical Journal, 752, 41

Yang Q., et al., 2018, The Astrophysical Journal, 862, 109

Yao H. F. M., et al., 2020, The Astrophysical Journal, 903, 91

York D. G., et al., 2000, Astronomical Journal, 120, 1579

Yu Q., Tremaine S., 2002, Monthly Notices of the RAS, 335, 965

Yuan S., Strauss M. A., Zakamska N. L., 2016, Monthly Notices of the Royal Astronomical Society, 462, 1603

Yung L. Y. A., Somerville R. S., Finkelstein S. L., Hirschmann M., Davé R., Popping G., Gardner J. P., Venkatesan A., 2021, Monthly Notices of the RAS,

Zetzl M., et al., 2018, Astronomy & Astrophysics, 618, A83

Zhang Y., et al., 2021, arXiv e-prints, p. arXiv:2105.11497

Zheng Z., Coil A. L., Zehavi I., 2007, The Astrophysical Journal, 667, 760

de Grijp M. H. K., Keel W. C., Miley G. K., Goudfrooij P., Lub J., 1992, Astronomy and Astrophysics, Supplementary Series, 96, 389

de Ruiter H. R., Lub J., 1986, in Swarup G., Kapahi V. K., eds, IAU Symposium Vol. 119, Quasars. p. 89

de Vaucouleurs G., 1959, Handbuch der Physik, 53, 275

de Zeeuw T., Franx M., 1991, Annual Review of Astronomy and Astrophysics, 29, 239

van Dokkum P. G., et al., 2010, The Astrophysical Journal, 709, 1018

van de Sande J., et al., 2021, Monthly Notices of the Royal Astronomical Society, 508, 2307